A dissertation submitted for the degree of
Doctor of Science

The theoretical prediction of neutrino emissions from the core-collapse supernovae and their progenitors

超新星爆発及びその親星における
ニュートリノ放出の理論予想

February 2019

Chinami KATO

加藤 ちなみ

The theoretical prediction of neutrino emissions from the core-collapse supernovae and their progenitors

超新星爆発及びその親星における
ニュートリノ放出の理論予想

February 2019

Waseda University
Graduate School of Advanced Science and Engineering
Department of Pure and Applied Physics,
Research on Theoretical Astrophysics

Chinami KATO

加藤 ちなみ

Abstract

Stars in the universe trace different evolutionary paths depending on their initial mass and end up in different ways. Especially the stars with $M_{\rm ZAMS} \gtrsim 8M_{\odot}$ cause a huge explosion, called supernova (SN), and then compact objects, such as neutron star (NS) and black hole (BH), are formed after the explosion. Many unclear points still remain, such as the internal structure of progenitors before the explosion, the mechanism of explosion and the formation scenario of compact objects. Since progenitors before the explosion and compact objects have extremely high temperature and density at the center, there may be a system that follows different physical laws from those on the earth. If we can solve these mysteries, there is a possibility to find new physics. In this thesis, I hence focus on the internal structure of massive progenitors and the explosion mechanism in terms of "neutrinos", which have a crucial role in the evolution of massive stars and SN explosions.

We usually calculate the evolution of massive stars dividing into three stages. The first stage is the quasi-stationary evolution phase of progenitors, the second is the SN explosion phase, and the third is the cooling phase of proto-neutron stars (PNS) remaining after the explosion. These evolutions are just theoretical predictions based on physics, so direct observations of the internal structures are necessary to confirm these predictions. We focus on observations of neutrinos, which can escape freely from the core because of their small cross sections with matters, and there is a possibility to get information about the central core with high temperature and density, directly. In fact, when the SN explosion occurred in the Large Magellanic Cloud in 1987, Koshiba et al. observed SN neutrinos released from PNS and contributed greatly to the understanding of the explosion mechanism. Thirty years have passed since then, neutrino detectors have been developed further and more detailed observations are possible. At the Super Kamiokande, which observes electron anti-neutrinos ($\bar{\nu}_e$'s), low background techniques have been developed, and DUNE, which will be able to detect electron neutrinos (ν_e's), is under construction. More realistic theoretical predictions on neutrinos are, therefore, strongly required to derive more detailed information with observations of next galactic SN explosions.

First of all, I focus on "pre-SN neutrinos" released from the center of progenitors at the first evolutionary stage. It is well known that energy losses by neutrinos become dominant over those by electromagnetic waves, and these effects are already taken into numerical simulations of stellar evolutions. While SN neutrinos are released with several tens of MeV, pre-SN neutrinos are mainly emitted with several MeV. Therefore, it is difficult to distinguish them from background of detectors, and it has never been focused in the observational point of view so far. However, with recent developments of neutrino detectors, there is a possibility of detecting

pre-SN neutrinos from neighborhood ($\sim$ kpc). In this study, I calculate luminosities and spectra of pre-SN neutrinos emitted from the progenitors with different initial masses for all flavors and examine their detectability. In particular, I focus on the difference between the progenitors of ONe core collapse supernova ("ONeCCSN") and Iron core collapse supernova ("FeCCSN"). Since it is well known that evolutions of the central density and temperature in both progenitors are greatly different at the late phase, I discuss whether they can be discriminated from observations of pre-SN neutrinos. I employ the results of the latest stellar evolution model as a background and obtain the evolutions of the neutrino luminosities and spectra. As a result, the neutrino luminosities and average energies of the FeCCSN progenitors gradually increase from several days before the explosion, whereas those from the ONeCCSN progenitors sharply rise from tens of milliseconds before the explosion. Finally, estimating the number of pre-SN neutrinos detected at the terrestrial detectors, the $\bar{\nu}_e$'s from the ONeCCSN progenitor can not be detected by almost all detectors, whereas for the FeCCSN progenitor all detectors can detect pre-SN neutrinos. On the other hand, the number of ν_e's events are largely depending on the mass hierarchy of neutrinos and it is expected to contribute to the determination of neutrino mass hierarchy.

Secondly, we pay attention to "SN neutrinos" accompanying a explosion. Although a SN explosion occurs when the shock wave formed at the center reaches the stellar surface, it stagnates inside the core because of the matter accretion and some additional heating sources are necessary for the shock to revive. The most promising source is the neutrinos emitted from PNS and they interact with matters behind the shock wave. This is called "neutrino heating mechanism". In this scenario, the energy given to the shock wave is determined by the total number and the average energy of the neutrinos emitted inside PNS. Therefore, it is necessary to deal with emission processes of neutrinos inside PNS and scattering processes with matters during propagation from the PNS surface to the shock wave in detail. In the recent numerical studies, the number of energy and angle bins are not enough to resolve the small energy exchanged by scatterings with heavy nucleons. However, since there are many nucleons inside stars, the number of scatterings is large and it is necessary to investigate how much the neutrino spectrum is changed by nucleon recoils. In this study, I carry out steady-state calculations of the neutrino transport from the PNS surface to the region, where neutrino reactions can be negligible, using Monte Carlo method based on the dynamical SN simulation. Then I calculate the change of neutrino spectra due to nucleon recoils and investigate whether it is necessary to incorporate them in dynamical SN simulations. The effects of nucleon recoils appear in the different way depending on neutrino flavors. For ν_e's and $\bar{\nu}_e$'s, charged current reactions with nucleons dominate other reactions and nucleon recoils do not change the spectra. On the other hand, for heavy-lepton neutrinos (ν_x's), which do not cause charge current reactions, the average energy and the number of neutrinos existing in the calculation domain are reduced by $\sim$ 15% and $\sim$ 7%, respectively, due to nucleon recoils. The reduction of neutrino opacities enhances the PNS contraction and the increase of temperature, which increase the luminosities of ν_e's and $\bar{\nu}_e$'s and the heating rates behind the shock wave.

Contents

Chapter 1

Introduction

1.1 Stellar evolution of massive stars

There are two types of progenitors that are supposed to produce CCSNe: in the majority case they produce a core mainly composed of irons (Fe-core); in the other case, which occupies ∼5% of all CCSNe according to a recent study (Doherty et al., 2017), a core is composed of oxygens and neons (ONe-core). The initial stellar mass on the main sequence is the main factor to determine which is obtained in the end: stars on the lightest end of massive stars (∼8-10 $M_\odot$) will lead to the latter and more massive stars will produce the former (Umeda et al., 2012; Jones et al., 2013). In this section, I explain their evolutions until the core begins to collapse.

1.1.1 Overview of stellar evolution

Stars evolve in the quasi-static state, in which self-gravity balances with the gradient of pressure. This condition is described in spherical symmetry as follows:

$$\frac{\partial P}{\partial r} = -\frac{Gm}{r^2}\rho \tag{1.1}$$

with the pressure P, the radius r, the gravitational constant G, the enclosed mass m and the matter density ρ. The thermal pressure produced by nuclear burning contributes largely to support the stellar mass. Stars are composed of hydrogen and helium at first and the heavier elements are created by nuclear burning with the stellar evolutions. The thresholds of temperature for nuclear burning depend on nuclei and the higher temperature is necessary to create the heavier elements in general. After the depletion of fuels for nuclear burning, stars contract and release their gravitational energy in order to raise the temperature and the thermal pressure until the next nuclear burning starts. Stars evolve repeating the series of nuclear burning, fuel depletion and core contraction.

The degeneracy of electrons terminates this cycle. Electrons are degenerate at the core and produce the new pressure, or the degeneracy pressure. Since there is the degeneracy pressures even at zero temperature, the hydrostatic equilibrium is satisfied and the contraction of the core stops before the temperature reaches the threshold for the next nuclear burning. These situations appear inside the stars with

the lighter initial mass $M_{\rm ZAMS} \lesssim 8M_\odot$, whose mass of the core at the end of He-burning is less than the upper limit which can be supported only by the degenerate pressure, or the "Chandrasekhar mass":

$$M_{\rm ch} = 1.46 M_\odot \left(\frac{Y_e}{0.5}\right)^2, \tag{1.2}$$

with the electron fraction Y_e. The stars supported only by the degenerate pressure are called "white dwarfs (WDs)" and we name the WDs composed of carbon mainly as "carbon white dwarfs (C-WDs)". They cool down by thermal radiation gradually and finish their lives.

On the other hand, oxygen and neon can be produced by C-burning inside the core of the massive stars with $M_{\rm ZAMS} \gtrsim 8M_\odot$. Thereafter three paths, i.e. ONe-WDs, ECSNe or FeCCSNe, are considered depending on the initial mass. In the first path, the nuclear burning can not proceed further because of the degeneracy of electrons and ONe-WDs are formed in the same way as C-WDs. The stars passing through the latter two paths cause violent explosions, called "supernovae (SNe)", at the different evolutionary phase (See Section 1.1.3, 1.1.4 in detail). The maximum luminosities of SN explosions reach 10^{10} times larger than the solar luminosity and their kinetic energy is $\sim 10^{51}$ erg, typically. Since the heavy elements synthesized inside stars are blown off by SN explosions, they also affect the chemical evolutions of galaxies. Moreover, compact objects, i.e. neutron stars (NSs) and black holes (BHs), remain at the center after the explosions. The former objects, NSs, are the stars in which many neutrons with the total mass $M \sim 1.4M_\odot$ are jammed within ~ 10 km and their central density reaches $\rho \gtrsim 10^{14}$ g/cm^3. They support their own mass by the degeneracy pressures of neutrons and the repulsive forces between neutrons. The latter objects, BHs, are formed when they can not keep the balance between self-gravity and these forces. There is no trend that the stars with the larger initial mass form BHs, because some massive stars emit the large amount of their envelope before the explosions (Ugliano et al., 2016). It is still unknow how to form these compact objects. In some cases, the SN explosions in the binary systems form the binaries of NS-NS, NS-BH or BH-BH, which are the important sources of gravitational waves. Detecting the gravitational wave from the BH-BH binary in 2016 (Abbott et al., 2016), many researchers investigate the formations of these compact objects recently.

As it is shown so far, the evolutions of stars depend on the initial mass $M_{\rm ZAMS}$. The overview of the stellar evolutions with the various initial masses is summarized in Figure 1.1. The boundaries of the initial mass among the evolutionary paths are still unknown (Doherty et al., 2017), because the stellar evolutions themselves highly depend on the input physics treated in the numerical simulations. We need observational evidence in order to confirm the theories of the stellar evolutions in the future.

In the following sections, I focus on the massive stars with $M_{\rm ZAMS} \gtrsim 8M_\odot$ and explain their evolutions in detail.

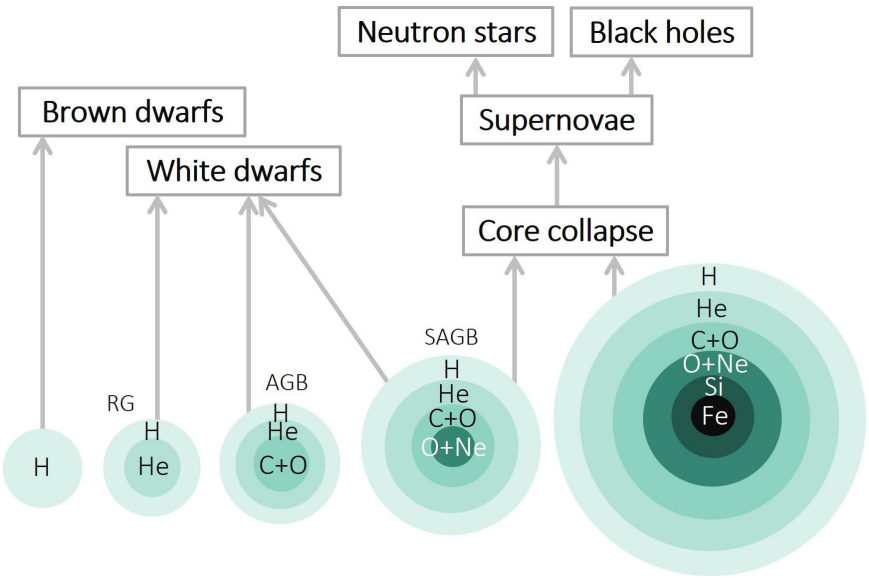

Figure 1.1: The overview of the stellar evolutions.

1.1.2 Evolutions from main-sequence to ONe-core formation

Protostars, which are formed by the gravitational collapse of hydrogen clouds, contract by self-gravity and the temperature increases gradually. When the temperature becomes larger than $\sim 10^7$ K, H-burning occurs and helium is produced by CNO cycles. This stage is called "Main Sequence (MS)" stage. The energy generation of the CNO cycles is large enough to develop the convections inside the H-core and the fraction of hydrogen decreases uniformly. Figure 1.2 shows the time evolution of the stellar structure, called the "Kippenhahn diagram". The shaded regions correspond to the convective regions by the nucelar burning.

After hydrogen is depleted at the center, the stars go into the "Red Giant Branch (RGB)" phase, in which the He-core is formed and H-burning continues at the shell around the core. They can be supported by the energy generated via the shell H-burning and the core contracts with the increase of thermal pressures. That makes the pressure gradient around the shell H-burning region steep and the stars expand drastically. The surface temperature decreases $T_{\rm s} \sim 3000$ K because of the expansion and the stars in this phase look "red" by observations.

Because there is no energy source to balance self-gravity, the core begins to contract and release the gravitational energy. Helium burning occurs at the region where the temperature exceeds the energy threshold $T_{\rm He} \sim 2 \times 10^8$ K and carbon and oxygen are produced mainly at the core. When the CO-core is formed after the depletion of helium, electrons are degenerate in the core of the stars with $M =$ 8-10 $M_\odot$. The core has the negative gradient of the temperature and carbon burning ignites at the outer part of the core shown in the bottom panel of Figure 1.2. From this figure, we can find the heat of C-burning propagates to the center and C-burning occurs in the whole core, and a ONe-core is formed. The C-burning inside the stars

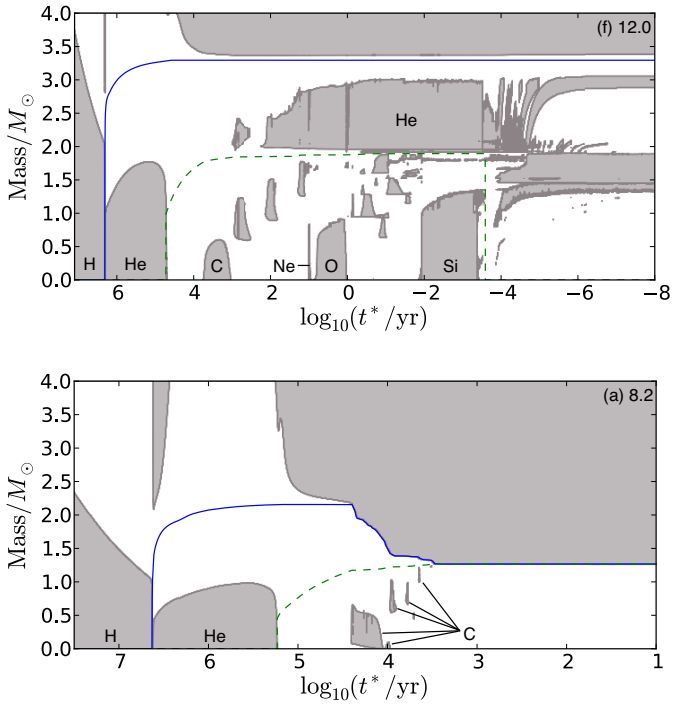

Figure 1.2: The kippenhahn diagram of the progenitors with $12M_\odot$ (top) and $8.2M_\odot$ (bottom). Convections occur at the shaded regions. (Jones et al., 2013)

with $M \gtrsim 10M_\odot$, on the other hand, begins at the center shown in the top panel of Figure 1.2.

The properties of nuclear burning phases in the massive stars are summarized in Table 1.1.2. The thresholds of the temperatures for the heavier elements are higher, because the heavier nuclei have the larger charges and the larger energy is necessary to cause the nucelar burning. As energy generation rates by the nuclear burning of heavier elements are more sensitive to the temperature, they are burned out in a shorter timescale.

Table 1.1: The properties of the nuclear burning inside massive stars.

Stage	$T_{\rm th}$ [K]	Duration time	Main reactions
H burning	1.5×10^7	10^7 yrs	H $\rightarrow$ ^{4}He
He burning	2×10^8	10^6 yrs	^{4}He $\rightarrow$ ^{12}C, ^{16}O
C burning	6×10^8	10^3 yrs	^{12}C $\rightarrow$ ^{16}O, ^{20}Ne, ^{24}Mg
Ne burning	1.3×10^9	1 yrs	^{20}Ne $\rightarrow$ ^{16}O, ^{24}Mg
O burning	3×10^9	1 yrs	^{16}O $\rightarrow$ ^{28}Si, ^{32}S
Si burning	4×10^9	10 days	^{28}Si $\rightarrow$ Fe elements

1.1.3 Electron capture supernovae (ECSNe)

Thermal neutrino emission phase

The ONe-core contracts by neutrino cooling via plasmon decays at first. In Figure 1.3, several important timescales are shown. We find that a contraction timescale $\tau_{\rm con}$ is close to a Kelvin-Helmholtz one $\tau_{\rm KH}$. As the entropy decreases as well as the temperature, thermal neutrino emission become less effective and their timescale becomes longer.

Core mass growth phase

Because of the suppression of neutrino emission, the ONe-core contracts by the growth of the core mass through the shell C-burning. The timescale of the mass growth $\tau_{\rm growth}$ becomes shorter than that of neutrino cooling (See Figure 1.3). Since the growth of the core mass occurs at a constant rate and the neutrino cooling is suppressed, the central density and temperature increase monotonically.

Electron capture phase

The mass of the ONe-core increases through the shell C-burning and if it exceeds the critical value $M_{\rm core} = 1.376\ M_\odot$, at which the central density reaches the threshold for EC on ^{24}Mg ($\rho_c = 10^{9.88}$ g/cm^3):

$$^{24}{\rm Mg} + e^- \longrightarrow {}^{24}{\rm Na} + \nu_{\rm e}, \tag{1.3}$$

$$^{24}{\rm Na} + e^- \longrightarrow {}^{24}{\rm Ne} + \nu_{\rm e}, \tag{1.4}$$

then the core begins to contract, losing the pressure support from electrons (Takahashi et al., 2013). The reduction in the mass fraction of ^{24}Mg is shown in Figure 1.4. This leads in turn to EC on ^{20}Ne ($\rho_c = 10^{10.3}$ g/cm^3):

$$^{20}{\rm Ne} + e^- \longrightarrow {}^{20}{\rm F} + \nu_{\rm e}, \tag{1.5}$$

accelerating the contraction and eventually igniting O and Ne at the point where the temperature exceeds the critical value $T_C = 10^{9.2}$ K.

ONe deflagration phase

The regions, where O- and Ne-burnings occur, expand and the surrounding matters are compressed, which makes the temperature high enough to cause the O- and Ne-burnings. The propagation of the front of O- and Ne-burnings looks like a wave, called "deflagration", shown in Figure 1.5 and behind it the nuclear statistical equilibrium (NSE) is established. Neutrinos are then emitted copiously via EC reactions on iron-group elements and free protons, which eventually trigger the collapse of the ONe-core that proceeds on a dynamical time scale. We call this mode of the evolution to collapse and the following CCSN either "electron capture supernovae (ECSNe)" or "ONe-core collapse supernovae (ONeCCSNe)". The resultant SN explosions are supposed to be weaker with an explosion energy of $\sim 10^{50}$ erg than FeCCSNe with $\sim 10^{51}$ erg (Kitaura et al., 2006). In fact, SN1054, which produced the Crab pulsar, may be one of such ECSNe (Nomoto et al., 1982; Tominaga et al., 2013).

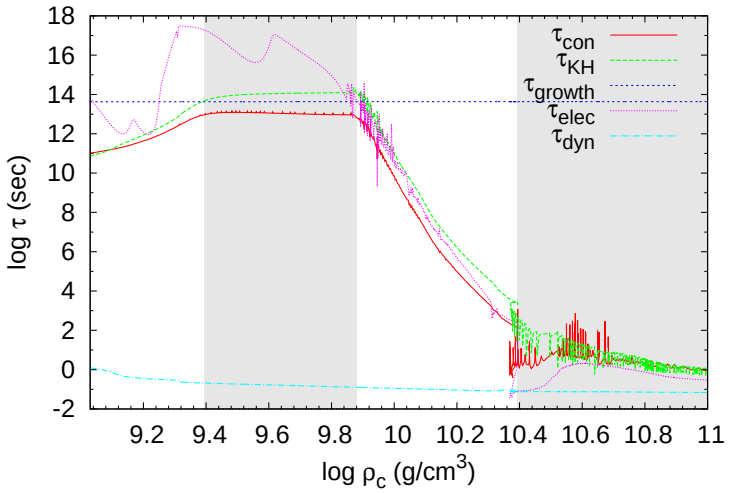

Figure 1.3: The evolutions of the timescales with the central density. Color lines denote the different timescales: core contraction $\tau_{\rm con}$ (red, solid line), KelvinHelmholtz $\tau_{\rm KH}$ (green, long dashed line), core mass growth $\tau_{\rm growth}$ (blue, short dashed line), EC $\tau_{\rm elec}$ (magenta, dotted line), and dynamical timescale $\tau_{\rm dyn}$ (cyan, dash-dotted line). Background colors show four evolutionary phases: thermal neutrino emission phase, core mass growth phase, electron capture phase, and deflagration phase. (Takahashi et al., 2013)

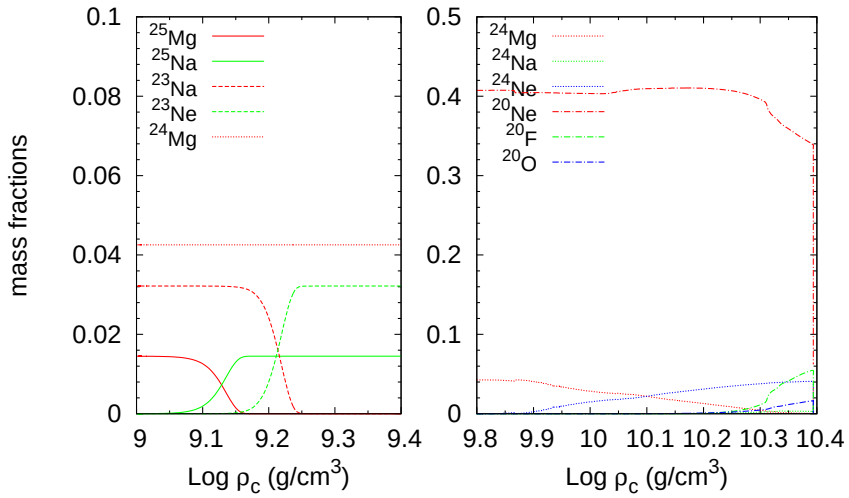

Figure 1.4: The evolutions of the mass fractions of electron capture nuclei with the central density. (Takahashi et al., 2013)

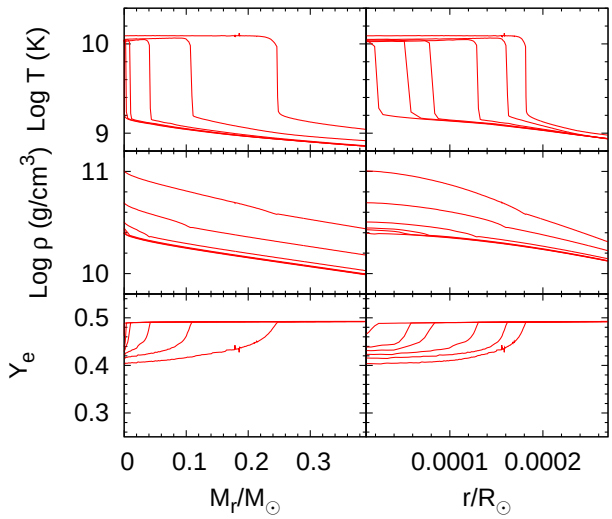

Figure 1.5: The profiles of temperature, density, and electron fraction during the O+Ne deflagration phase. They are taken at $1.13 \times 10^{-2}, 5.40 \times 10^{-2}, 9.92 \times 10^{-2}, 1.49 \times 10^{-1}, 2.00 \times 10^{-1}$, and 2.34×10^{-1} s after the ignition at the center of the core. (Takahashi et al., 2013)

1.1.4 Iron-Core Collapse Supernovae (FeCCSNe)

If stars are massive enough ($M_{\rm ZAMS} \gtrsim 10\ M_\odot$), then the temperature reaches the ignition point of Ne or O at the center, synthesizing iron-group elements through Si-burnings ($T_c = 10^{10.6}$ K). As iron is the most stable nuclei to both of nuclear fusion and decay, further nuclear burning does not proceed. Neutrinos are, on the other hand, emitted efficiently via EC's on free protons and iron-group elements and get away energy from the core. Furthermore, when the temperature exceeds $T = 10^{10}$ K, the free energy becomes lower if iron decomposes into small particles such as helium and nucleons with photons, called photo-dissociations:

$$^{56}\mathrm{Fe} \longrightarrow 13\ ^4\mathrm{He} + 4\ n, \tag{1.6}$$

$$^4\mathrm{He} \longrightarrow 2\ p + 2\ n. \tag{1.7}$$

They are endothermic reactions and the Fe-core begins to contract. As the density increases, the Fermi energy of electrons also increases and the EC's occur more efficiently. Moreover, the increase of the temperature due to the core contraction also enhances the decompositions of heavy elements. The cycle of these two processes triggers the gravitational collapse of the Fe-core. This mode of the evolution to collapse and the ensuing explosion are referred to as "iron core collapse supernovae (FeCCSNe)".

1.2 Supernova explosion

The evolutions of the two types of progenitors after the core collapse are very similar, although the timescales of their core collapses are different. In this section, I explain the mechanism of the core collapse and SN explosion for FeCCSNe.

1.2.1 Core collapse and neutrino trapping

The core begins to collapse at the central density $\rho_c = 10^{10}$ g/cm^3, and the density and Fermi energy of electrons increase during the collapsing phase. These conditions enhance the EC's and the number of neutrons increases gradually, called "neutronization". This situation is, however, changed after neutrinos are trapped inside the Fe-core.

The typical cross section of weak interactions is estimated as

$$\sigma_{\rm weak} \sim {G_F}^2 {\epsilon_\nu}^2 \sim 10^{-42}\ {\rm cm}^2 \left(\frac{\epsilon_\nu}{10{\rm MeV}}\right)^2, \tag{1.8}$$

using the Fermi coupling constant $G_F = 1.166364 \times 10^{-11}$ MeV^{-2} and the neutrino energy ϵ_ν. The mean free path of neutrinos interacting with neutrons:

$$l_{\rm mfp} \sim \frac{1}{n_n \sigma} \sim 10^9\ {\rm cm} \left(\frac{\rho}{10^{10}{\rm g/cm^3}}\right)^{-1} \left(\frac{\sigma}{10^{-42}{\rm cm^2}}\right)^{-1}, \tag{1.9}$$

is longer than the typical size of the Fe-core $\sim 10^7$ cm at the beginning of the core collapse. That means neutrinos can escape freely from the core. As the density increases, this cross section becomes larger and the mean free path becomes shorter. Moreover, the cross section of coherent scatterings by the nucleons bounded inside nuclei becomes proportional to the square of the mass number of nuclei, because the De Broglie wave length of neutrinos is longer than the radius of nuclei. It is known that large nuclei can be formed because of the Coulomb screening by electrons as the density increases (Furusawa et al., 2011) and the cross section of coherent scatterings increases. Taking the coherent scatterings into account, the mean free path of neutrinos at the density $\rho \sim 10^{11}$ g/cm^3:

$$l_{\rm mfp} \sim 10^7\ {\rm cm} \left(\frac{\epsilon_\nu}{10{\rm MeV}}\right)^{-2} \left(\frac{\rm A}{56}\right)^{-1} \left(\frac{\rho}{10^{11}{\rm g/cm^3}}\right)^{-1}, \tag{1.10}$$

is shorter than the radius of the core and then neutrinos propagate through matters as a random walk. The degree of diffusion is described using the optical depth, defined as

$$\tau\left(\epsilon_\nu\right) = \int_r^\infty \frac{1}{l_{\rm mfp}\left(\epsilon_\nu\right)} ds. \tag{1.11}$$

We usually define the critical value of the optical depth for neutrino reactions as 2/3 and we call the point where this condition is satisfied as "neutrino sphere". The timescale of this random walk is described as

$$t_{\rm diff} \sim 10\ {\rm ms} \left(\frac{\rm R_{core}}{10^7{\rm cm}}\right)^2 \left(\frac{\epsilon_\nu}{10{\rm MeV}}\right)^2 \left(\frac{\rho}{10^{12}{\rm g/cm^3}}\right). \tag{1.12}$$

The dynamical timescale is, on the other hand, proportional to the square root of the density:

$$t_{\rm dyn} \sim \frac{1}{\sqrt{G\rho}} \sim 10\ {\rm ms} \left(\frac{\rho}{10^{12}{\rm g/cm^3}}\right)^{-1/2}. \tag{1.13}$$

Comparing the two timescales, if the density exceeds $\rho = 10^{12}$ g/cm^3, neutrinos are trapped inside the core ("neutrino trapping").

Due to the neutrino trapping, the beta equilibrium condition:

$$\mu_e + \mu_p = \mu_n + \mu_{\nu_e}, \tag{1.14}$$

is achieved inside the core, because the inverse reactions of EC ($n+\nu_e \rightarrow p+e^-$) can occur and neutrinos also become degenerate. The neutronization does not proceed under the beta equilibrium and the electron fraction is fixed at $Y_e \sim 0.3$, typically.

1.2.2 After the core bounce to the stagnation of the shock

The core continues to collapse until the center density reaches the nuclear saturation density $\rho_c \sim 10^{14}$ g/cm^3. The adiabatic index is $\Gamma \sim 4/3$ during the core collapse, whereas it becomes $\Gamma \sim 2$ where the density exceeds the saturation density. The sudden change of the adiabatic index makes the core stable and the core collapse stops and begins to expand, which is called a "core bounce". Since the matters in the inner part of the core (inner core) contract with a subsonic speed, their core bounces coincide. The matters in the outer part of the core (outer core), on the other hand, contract with a supersonic speed and the information about the core bounce is not transmitted there in the top panel of Figure 1.6. Then, a shock wave is formed at the boundary between the inner and outer cores. The initial energy of the shock wave is estimated using the gravitational energy of the inner core:

$$E_{\rm shock} \sim \frac{GM_{\rm inner}^2}{R_{\rm inner}} \sim 10^{51}\ {\rm erg}, \tag{1.15}$$

with the mass and the radius of the inner core $M_{\rm inner} \sim 0.6$-$0.9\ M_\odot$, $R_{\rm inner} \sim 10$ km, respectively.

The shock wave propagates outwards by the pressure of the matters in the downstream. The middle panel of Figure 1.6 shows the propagation of the shock wave, which is described as the discontinuity of the density. The matters in the upstream are compressed and their kinetic energies are dissipated when they pass through the shock wave and the temperature behind the shock wave becomes higher. In this region, photo-dissociations of nuclei occur and the pressure of matters for driving up the shock waves is reduced. The typical energy loss by the photo-dissociations is estimated as

$$E_{\rm loss} \sim 1.6 \times 10^{51}\ {\rm erg} \left(\frac{\rm M_{outer}}{0.1 \rm M_\odot} \right), \tag{1.16}$$

which is as large as the initial energy of the shock wave. Furthermore, after the shock wave passes through the neutrino sphere, neutrinos trapped inside the Fe-core, especially ν_e, can escape easily from the post shock regions, which is called a "neutronization burst" (See Section 1.3.3). Then, neutrinos, which are emitted efficiently in the region with the high temperature, reduce the energy of the shock wave. Finally, the shock wave stagnates at the radius $r \sim$100-200 km inside the outer core in Figure 1.7. The matters accrete to a PNS, which is formed at the central part of the core, and the mass of the PNS increases in the accretion phase. In some cases, the PNS collapses to the BH when the mass of the PNS exceeds the

Chandrasekhar limit $M \sim 1.4M_\odot$ because of the matter accretion. If we reproduce SN explosions, which means that the shock wave reaches the stellar surface and blows off the envelope of the star, some energy should be given to the stalled shock wave.

1.2.3 Neutrino heating mechanism and shock revival

The most favorable mechanism to give energy to the stalled shock is a "neutrino heating mechanism", in which neutrinos emitted from the PNS interact with the nucleons behind the shock wave. The idea of this mechanism comes from the fact that most of the gravitational energy released during the core collapse converts to the internal energy of the PNS. The gravitational energy, which is released during the core collapse, ΔW is estimated as

$$\Delta W = \left(-G\frac{M_{\rm core}^2}{R_i}\right) - \left(-G\frac{M_{\rm core}^2}{R_f}\right) \sim 10^{53}\ {\rm erg} \tag{1.17}$$

using the core mass $M_{\rm core} = 1.4M_\odot$ and the initial and final radii of the core at the core collapse $R_i \sim 10^8$ cm and $R_f \sim 10^6$ cm, respectively. As I mentioned in the previous section, the initial energy of the shock wave is just $\sim 10^{51}$ erg, which is $\sim$1% of the released energy ΔW and the remaining $\sim$99% are stored inside the core as the internal energy. This energy is taken away by the neutrinos trapped inside the PNS gradually. The timescale of diffusion of neutrinos inside the PNS is

$$t_{\rm diff} \sim 100\ {\rm ms}\left(\frac{\rm R_{core}}{3\times10^6{\rm cm}}\right)^2\left(\frac{\epsilon_\nu}{10{\rm MeV}}\right)^2\left(\frac{\rho}{10^{14}{\rm g/cm^3}}\right). \tag{1.18}$$

This is the typical time scale of the shock heating by neutrinos.

Assuming that neutrino luminosities do not depend on neutrino flavors, the total neutrino luminosity for all flavors from the PNS is estimated by the radius of the PNS $R_{\rm PNS}$ and the temperature at the neutrino sphere T_ν:

$$L_\nu \sim 4\pi R_{\rm PNS}^2\sigma_{\rm SB}T_\nu^4 \times 6 \sim 2\times10^{52}\ {\rm erg/s}\left(\frac{\rm R_{PNS}}{10{\rm km}}\right)^2\left(\frac{\rm k_B T_\nu}{4{\rm MeV}}\right)^4, \tag{1.19}$$

with the Stefan-Boltzmann constant $\sigma_{\rm SB}$. Although the shock wave stagnates outside of the neutrino sphere $R_\nu \sim 50$ km and the optical depth for neutrinos is less than 1 there, neutrinos can still interact with the nucleons behind the shock wave:

$$\nu_e + n \longrightarrow p + e^-, \tag{1.20}$$

$$\bar{\nu}_e + p \longrightarrow n + e^+, \tag{1.21}$$

because there are large amount of nucleons produced by the photo-dissociations between the neutrino sphere and the shock radius. Matters get energy from neutrinos via these reactions, whose heating rate per nucleon is derived from the neutrino luminosity L_ν and the cross section σ as follows:

$$\left(\frac{dE}{dt}\right)_{\rm abs} \sim \frac{L_\nu\sigma}{4\pi r^2} = 8\ {\rm Mev/s}\left(\frac{\rm L_\nu}{10^{52}{\rm erg/s}}\right)\left(\frac{\epsilon_\nu}{10{\rm MeV}}\right)^2\left(\frac{\rm r}{200{\rm km}}\right)^{-2}. \tag{1.22}$$

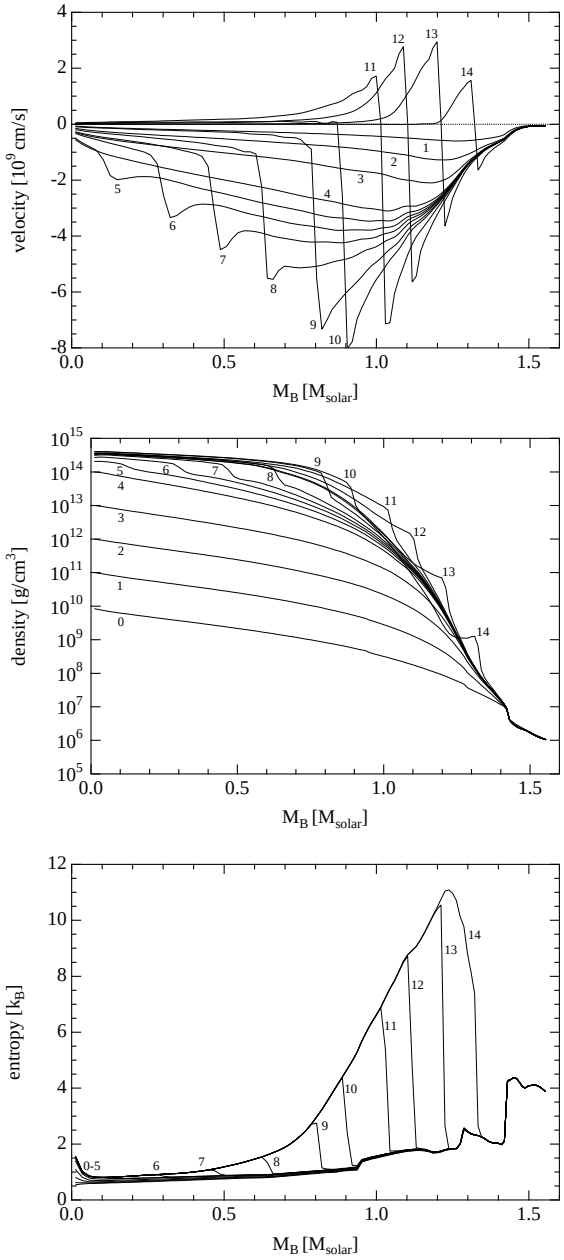

Figure 1.6: The propagation of the shock wave from the core bounce $t_{\rm pb} = 0$ to $t_{\rm pb} = 12$ ms. The profiles of velocity (top), density (middle) and entropy (bottom) are shown as the function of the mass coordinate. The profiles at the numbers 1-4 correspond the time at which the density becomes 10^{11}, 10^{12}, 10^{13} and 10^{14} g/cm^3, respectively. (Sumiyoshi et al., 2004)

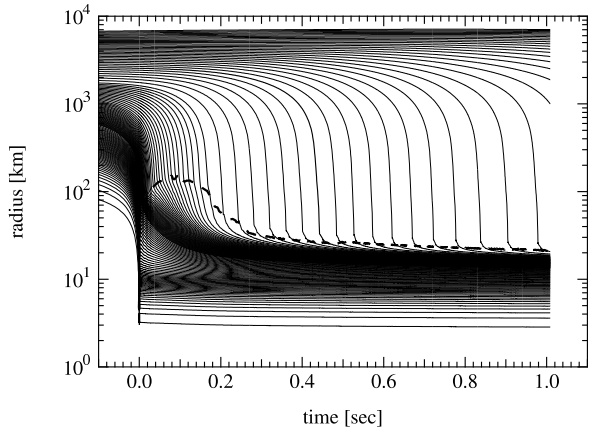

Figure 1.7: The radial trajectories of mass elements in the core of $15M_\odot$ progenitors as a function of the time after the core bounce. The thick dashed line denotes the location of the shock wave. (Sumiyoshi et al., 2005)

Neutrinos, on the other hand, are emitted due to the inverse reactions of the heating:

$$p + e^- \longrightarrow \nu_e + n, \tag{1.23}$$
$$n + e^+ \longrightarrow \bar{\nu}_e + p. \tag{1.24}$$

They play a role as the cooling of the shock wave and their rate per nucleon is described as

$$\left(\frac{dE}{dt}\right)_{\rm emis} \sim -\sigma v_{e^\pm} n_{e^\pm} \langle \epsilon_\nu \rangle, \tag{1.25}$$

using the velocity and number density of electrons or positrons $v_{e^\pm} \sim c$ and $n_{e^\pm}$, the cross section σ and the average energy $\langle \epsilon_\nu \rangle$. The net heating, which is defined as the difference between the heating and cooling rates, is written as

$$\left(\frac{dE}{dt}\right)_{\rm net} \sim \left(\frac{dE}{dt}\right)_{\rm abs} \left[1 - \left(\frac{2r}{r_\nu}\right)^2 \left(\frac{T_m}{T_\nu}\right)^6\right]. \tag{1.26}$$

The first term decreases with r^{-2} (see eq. (1.22)), whereas the matter temperature T_m in the second term decreases with r^{-1}. The second term hence dominates at a large radius, which means that neutrinos give energy to the shock wave. Where the equilibrium of heating and cooling is achieved is called a "gain radius" r_g and the region where $r \geq r_g$ is named as a "gain region". The typical gain radius is ~ 100 km and whether the shock radius is larger than the gain radius or not is critical for the shock revival. Moreover, it is also important how long neutrinos can stay in the gain region and give energy to matters. The sufficient timescale for the shock revival depends on the neutrino luminosities and mass accretion rates; the higher neutrino luminosity and the lower mass accretion rates are necessary (Yamasaki and Yamada, 2006).

It is known that the heating by neutrinos is not enough to revive the shock wave and the supernova explosion does not occur in the spherical symmetric simulations

(Sumiyoshi et al., 2005). Many researchers try to do multi-dimensional supernova simulations recently. In the multi-dimensional simulations, the non-spherical motions of matters, such as a convection or a standing accretion shock instability ("SASI"), push up the shock wave (Iwakami et al., 2007) and extend the staying time of neutrinos in the gain region. Some successful simulations have come to be reported recently (Takiwaki et al., 2016; Nagakura et al., 2018; Summa et al., 2016; O'Connor and Couch, 2018; Skinner et al., 2015).

There is the alternative mechanism to revive the shock wave, for example the acoustic mechanism (Burrows et al., 2006) and the magneto-rotational mechanism (Obergaulinger et al., 2009). The kinetic energies of SN explosions derived from dynamical simulations depend on explosion mechanisms and they may explain the diversity of SN observations.

1.2.4 PNS cooling

After the Shock wave is revived by the neutrino heating and propagate through the outer core, the matter accretion stops and the PNS is separated from the surroundings and cooled by neutrinos gradually. This phase is called "PNS cooling phase".

The mean free path of the neutrinos inside the PNS is

$$l_{\rm mfp} \sim 10 \text{ cm} \left(\frac{\rho}{10^{14}\text{g/cm}^3}\right)^{-1} \left(\frac{\text{E}_\nu}{100\text{MeV}}\right)^{-2}, \tag{1.27}$$

which is much shorter than the radius of the PNS $r_{\rm PNS} \sim 10$ km. Neutrinos hence propagate diffusively and the neutrino transport is usually treated under a diffusion approximation. The energy of neutrinos is ~ 100 MeV in the inner part of the PNS and they lose their own energy to ~ 10 Mev at the PNS surface via interactions with matters. The emission of neutrinos in this phase last ~ 10 s estimated by the internal energy U and the neutrino luminosity L_ν:

$$t_{\rm PNS} \sim \frac{U}{L_\nu} \sim 10 \text{ s} \left(\frac{\text{U}}{10^{53}\text{erg}}\right) \left(\frac{\text{L}_\nu}{10^{52}\text{erg/s}}\right)^{-1}. \tag{1.28}$$

They are the most favorable for observations like that at SN1987A. (See Section 1.5)

It is known that the negative gradient of lepton numbers per nucleon inside the PNS causes a "PNS convection" (Dessart et al., 2006). Since neutrinos propagate through matters inside the PNS diffusively, the lepton numbers near the PNS surface are taken away by neutrinos more efficiently, which causes the negative gradient $dY_l(z)/dz < 0$. The larger energy is transported by the PNS convection and the neutrino luminosities increase ∼10-20% (Müller and Janka, 2014). The heating behind the shock wave is hence enhanced by the PNS convection.

The PNS is cooled down with the decreases of the neutrino luminosities and the lepton numbers for ~ 1 minute. As the temperature becomes low enough that neutrinos escape the PNS without interactions with matters, the evolutionary phase moves to a NS cooling.

1.3 Neutrino properties of massive star evolutions and supernova explosions

As I explained so far, neutrinos have an important role in the evolutions of massive stars and SN explosions. In this section, I summarize important neutrino reactions and their current understandings.

1.3.1 In the quasi-static evolutionary phase

Neutrinos are emitted from the stellar core with the higher temperature and density and take energy away from stars. The energy losses by neutrinos dominate those by photons after the C-burning phase (Arnett, 1996) and neutrinos affect the thermal evolution of the core. We call neutrinos emitted from the core of the massive stars "pre-SN neutrinos". The important reactions for neutrino emission in the quasi-static evolutionary phase are classified into thermal pair emission and nuclear weak interactions mainly. EC's on free protons are also important just before the core collapse, which trigger the core collapse of the FeCCSNe-progenitors.

Thermal emission of neutrino pairs

There are four processes responsible for the neutrino emission: 1. annihilations of electronpositron pairs, 2. plasmon decays, 3. photo-pair processes, 4. bremsstrahlungs by electrons and positrons accelerated by nuclei. They produce all flavors of neutrinos. The reaction rates of these processes depend mainly on three hydrodynamical variables: density, temperature and electron fraction (or electron chemical potential).

1. Electron-positron pair annihilation
   When the temperature in the core becomes $\gtrsim 10^9$ K, the number of photons with high enough energy to produce electron-positron pairs becomes large. As the temperature increases, these pairs become highly abundant, being in chemical equilibrium with photons. Although they annihilate each other to generate photons most of the time, they produce from time to time pairs of neutrino and anti-neutrino via weak interaction.

   $$\gamma \longleftrightarrow e^+ + e^- \longrightarrow \nu_e + \bar{\nu}_e \tag{1.29}$$

   The Feynman diagram corresponding to this process is displayed in Figure 1.8. This production process is called "pair-annihilation process".

2. Plasmon decay
   Plasmons are quantized collective motions of plasma. They are much like photons as shown in the Feynman diagram given in the right panel of Figure 1.8, obeying the Bose-Einstein statistics. Unlike ordinary photons in vacuum, however, they are massive quasi-particles, having a longitudinal mode in addition to the two transverse modes[1]. Thanks to this property, a plasmon decay to

[1] In some textbooks, only the longitudinal mode is called plasmon. In this paper, I refer also to the transverse modes as plasmon.

two massless particles is not kinetically forbidden, the fact which is in sharp contrast to photons in vacuum. The plasmon decay to a pair of neutrinos,

$$\gamma^* \longrightarrow \nu + \bar{\nu}, \tag{1.30}$$

is one of the main cooling processes in the massive stars after C-burning.

3. Photo neutrino
   Photons, which get energy from electrons in the same way as Compton scatterings, can produce neutrino pairs:

$$e^- + \gamma \longrightarrow e^- + \nu + \bar{\nu}. \tag{1.31}$$

   This reaction is important for the lower density $\rho \lesssim 10^5$ g/cm^3 and the lower temperature $T \lesssim 4 \times 10^8$ K, because photons can produce the electron-positron pairs at high temperature.

4. Electron-nucleus bremsstrahlung
   When electrons feel the potential of surrounding ions, they are accelerated and emit neutrino pairs:

$$e^- + (Z, A) \longrightarrow e^- + (Z, A) + \nu + \bar{\nu}, \tag{1.32}$$

   in the same way as the photon emission by bremsstrahlungs. The reaction rate of bremsstrhlungs becomes large when electrons are relativistic and non-degenerate with the larger temperature $T \gtrsim 10^8$ K and the lower density $\rho \lesssim 2 \times 10^6$ g/cm^3.

Having in mind applications to the stellar evolution calculations, Itoh et al. (1996) obtained useful fitting formulae to the energy loss rates for these processes. They also drew a phase diagram in the $\rho - T$ plane to indicate which reaction is dominant for a given combination of density and temperature. According to their results, Kato et al. (2015) plotted the typical evolutionary paths of massive stars in Figure 1.9, the electron pair annihilation and the plasmon decay will be the most important neutrino-emission processes for the evolutions of the massive stars.

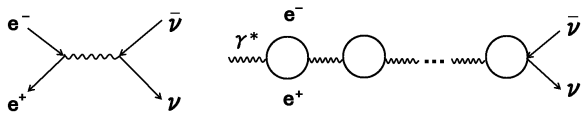

Figure 1.8: Feynman diagrams of the electron-positron pair-annihilation (left panel) and the plasmon decay (right panel).

Nuclear weak interaction

In the late evolutionary phase of progenitors, nuclear weak interactions can no longer be neglected. In particular, once opened, EC's by heavy nuclei are dominant reactions. They play an important role in the hydrodynamics of core-collapse

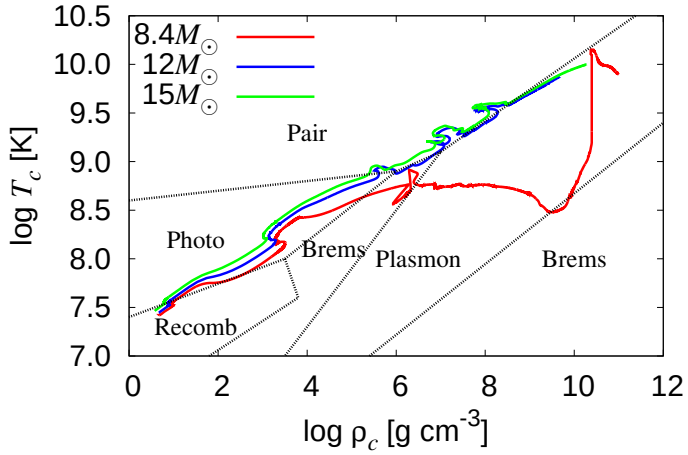

Figure 1.9: The dominant thermal emission processes of neutrinos indicated by Itoh et al. (1996) comparing with the typical trajectories of the central density ρ_c and temperature T_c for the massive stars. The red, blue and green curves correspond to 8.4, 12 and 15 $M_\odot$ models, respectively (Takahashi et al., 2013; Takahashi et al., 2016).

as explained earlier. Although β^+ decays of heavy nuclei also emit ν_e's, they are certainly sub-dominant. Electron anti-neutrinos are emitted either by positron captures (PC's) or β^- decays. Although they never affect the core dynamics up to core bounce, they are important from the observational point of view, since water Cherenkov detectors mainly observe them (See Sec 1.5). Moreover, Patton et al. (2017) pointed out that there may be a period, in which the β^- decay dominates the pair annihilation in the production of $\bar{\nu}_e$'s.

1. electron capture (EC)

$$(Z, A) + e^- \longrightarrow (Z - 1, A) + \nu_e \tag{1.33}$$

2. β^+ decay

$$(Z, A) \longrightarrow (Z - 1, A) + e^+ + \nu_e \tag{1.34}$$

3. positron capture (PC)

$$(Z, A) + e^+ \longrightarrow (Z + 1, A) + \bar{\nu}_e \tag{1.35}$$

4. β^- decay

$$(Z, A) \longrightarrow (Z + 1, A) + e^- + \bar{\nu}_e. \tag{1.36}$$

In the above expressions, Z and A are the atomic and mass numbers of nuclei, respectively.

Electron capture on free nucleon

Although they are not abundant, EC's on free protons:

$$p + e^- \longrightarrow n + \nu_e, \tag{1.37}$$

cannot be ignored, since the cross section is larger than those of EC's on heavy nuclei.

Recent studies of pre-SN neutrinos

Odrzywolek et al. (2004) calculated the luminosities and spectra of the neutrinos emitted by the pair annihilations during the C-, Ne-, O-, Si-burnings for a $20M_\odot$ progenitor model with the Monte Carlo method and estimated the number of detection events for 6 terrestrial neutrino detectors. They found that the mean energies of neutrinos are 0.71, 0.97, 1.1 and 1.8 MeV for the C-, Ne-, O- and Si-burnings, respectively. Assuming that the distance to the progenitors is 1 kpc, they evaluated the number of events would be 41 for Super-Kamiokande and 4 for KamLAND. Later they also investigated the energy spectrum of plasmon decays (Odrzywołek, 2007). What is important here is that the neutrinos emitted by these processes prior to collapse may be observable if the SN explosion occurs in our vicinity, e.g., within 1 kpc.

Odrzywolek (2009) and Patton et al. (2017) pointed out that neutrino emission via nuclear weak processes, such as β^- decay, may become dominant just prior to the collapse. Misch and Fuller (2016) discussed the importance of excited states in both parent and daughter nuclei in these processes.

Kato et al. (2015) took into account realistic stellar evolutions that lead to both the FeCCSN and ONeCCSN. They showed that these two types of SN progenitors can be distinguished by the detection (or no detection) of their pre-SN neutrinos. Yoshida et al. (2016) investigated more in detail the pre-SN neutrino luminosities and cumulative numbers of detection events as a function of time for FeCCSN-progenitors. They demonstrated that the pre-SN neutrinos can be used as a useful probe into the Si-burning, which occurs deep inside massive stars, if they are observed on the next-generation detectors such as JUNO and Hyper-Kamiokande. Moreover, they found that the number of events decreases during the shell burning phases due to the core expansion. Wright et al. (2016, 2017a,b) studied the neutrino emission from the progenitors of the other types of SN explosions, i.e. type Ia SNe and pair instability SNe.

1.3.2 Collapsing phase

Continuing from the quasi-static evolutionary phase, neutrino emission via EC's has an important role for the dynamics of the core collapse. The luminosity of ν_e's increases towards the core bounce, but it turns down quickly because of the neutrino trapping inside the core. In this phase, heavy nuclei contribute more largely than free protons because the core has very low entropy with $\sim 1\ k_B$ per nucleon and the fraction of free protons is very small $X_P \lesssim 10^{-3}$ (Langanke et al., 2003). The core is composed of the neutron rich nuclei with $A \gtrsim 60$ and the main contributors for

EC's are the nuclei with the closed nucleon shell $A \sim 80$ and $Z \sim 50$ (Sullivan et al., 2016). The rates of EC's on these neutron rich nuclei are still uncertain because we never confirm them by experiments on the Earth. Depending on the rates of EC's, the neutrino luminosity may change in $\sim 40\%$ (Sullivan et al., 2016).

As I explained, the mean free path of neutrinos becomes shorter than the radius of the Fe-core due to coherent scatterings by nuclei. Their cross section is described as

$$\frac{d\sigma}{d\Omega} = \frac{\sigma_0}{64\pi}\left(\frac{\epsilon_\nu}{m_e}\right)^2 A^2 \left[1 - \frac{2Z}{A}\left(1 - 2\sin^2\theta_W\right)\right]^2 C_{\rm FF}^2 \left(1 + \cos\theta\right) \tag{1.38}$$

using the typical factor of reaction rates of weak interactions $\sigma_0 = 4G_F^2 m_e^2/\pi \sim 1.7 \times 10^{-44}$ cm^2, the Weinberg-Salam angle $\sin^2\theta_W \sim 0.23$ and the form factor of nuclei $C_{\rm FF}$. In this formulation, we assume that scatters are delocalized within the wave length of scattered waves. The condition that the radius of the nuclei $r_A \sim 5\,(A/56)^{1/3}$ fm is smaller than the wave length of neutrinos $\lambda_\nu \sim 20\,(\epsilon_\nu/10{\rm MeV})^{-1}$ fm should be satisfied in this case. Only under this condition, we find the cross section is proportional to the square of the mass number.

After neutrinos are trapped inside the core, we have to solve Boltzmann equations for the transport of neutrinos inside the core.

1.3.3 After core bounce

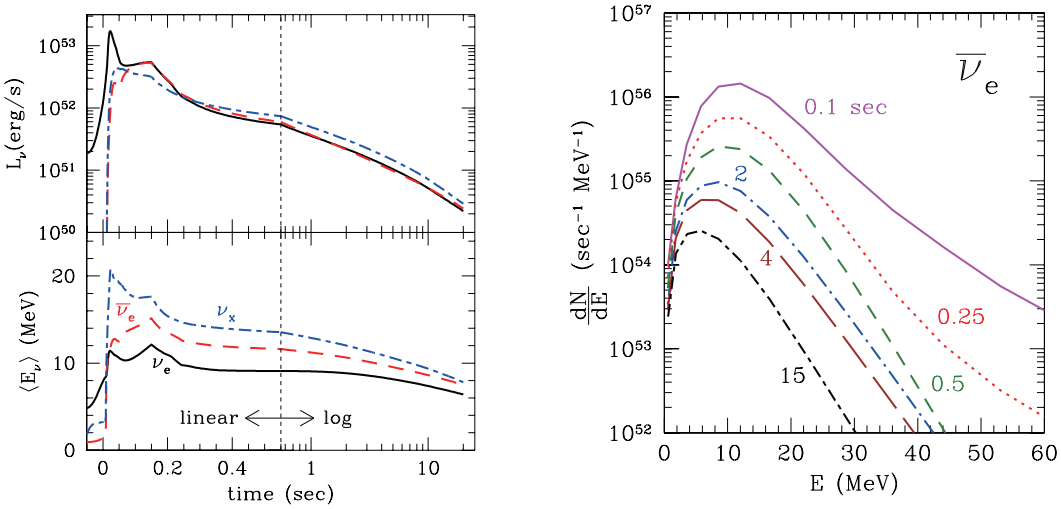

Figure 1.10: The properties of SN neutrinos from the core bounce to the PNS cooling. The left panel shows the time evolution of neutrino luminosities and average energies for ν_e's (black, solid), $\bar{\nu}_e$'s (red, dashed) and ν_x's (blue, dash-dotted). The right panel shows the time evolutions of spectra for $\bar{\nu}_e$'s. Color lines denote the spectra at the different time steps. (Nakazato et al., 2013)

Neutronization burst

Figure 1.10 shows the time evolutions of the neutrino luminosities after the core bounce. We find the sudden increase of the ν_e's luminosity several milliseconds

after the core bounce. This burst-like feature of ν_e's is called a "neutronization burst" and it is a standard candle of CCSNe. There are two important effects to form the neutronization burst: a shock breakout of neutrinos and a decomposition of the nuclei behind the shock wave. In the former, since the optical depth for neutrinos becomes less than 1 outside of the neutrino sphere, neutrinos emitted via EC's on the nucleons behind the shock wave can escape easily when the shock wave passes through the neutrino sphere. This phenomena occurs in the same way as the shock breakout of the photons around the stellar surface. In the latter, nuclei are decomposed into nucleons by the shock heating and the rate of coherent scatterings by nuclei can be neglected. This reduction makes the optical depth lower. The properties of the neutronization burst, i.e. the duration timescale ∼a few ms and the peak luminosity $\sim 4 \times 10^{53}$ erg/s, are universal not depending on progenitor models and input physics of EOS (Wallace et al., 2016).

After the shock breakout of neutrinos, the other flavors of neutrinos are also emitted via the thermal pair emission: electron-positron pair annihilation and nucleon bremsstrhlung:

$$e^- + e^+ \longrightarrow \nu + \bar{\nu} \tag{1.39}$$

$$N + N \longrightarrow N + N + \nu + \bar{\nu}. \tag{1.40}$$

For $\bar{\nu}_e$'s, PC's on neutrons dominate the thermal emission because many positrons exist behind the shock wave because the degeneracy of electrons is resolved by the high temperature. Since their luminosities are much smaller than that of ν_e's, if we take neutrino oscillations into account, the observed flux of ν_e's is reduced drastically. Therefore, we may find the mass hierarchy of neutrinos from the observation of the neutronization burst (Scholberg, 2018).

Accretion phase

After the shock wave stagnates inside the Fe-core, matters accrete to the PNS. The temperature around the PNS surface increases due to the heating by the matter accretion and neutrinos are emitted via charged current reactions efficiently. Neutrinos also diffuse out from the PNS. Initially the luminosity of ν_e's dominates that of ν_x's, but after the shock wave restarts to propagate outwards and the matter accretion stops, the luminosity hierarchy is inverted gradually. The average energies of neutrinos in all flavors increase with time and their order is $\langle E_{\nu_e} \rangle < \langle E_{\bar{\nu}_e} \rangle < \langle E_{\nu_x} \rangle$ depending on the position of neutrino sphere, typically (See Figure 1.10). ν_x's interact with matters only via neutral current reactions and the neutrino sphere is deeper than those for the other flavors. Some studies, however, show that the hierarchy of the average energy change to the order $\langle E_{\nu_e} \rangle < \langle E_{\nu_x} \rangle < \langle E_{\bar{\nu}_e} \rangle$, because the temperature profile inside the PNS is changed by the matter accretion (Marek et al.).

In this phase, the hydrodynamical instabilities, i.e. SASI or convection, appear in multi-dimensional simulations and help SN explosions. The multi-dimensional simulations become a mainstream for the studies of SN explosions. The features of SASI sloshing or spiral motions appear in the neutrino luminosities as the modulation of large amplitude with the frequency $\lesssim 100$ Hz and can be detected at the

terrestrial detectors, Ice Cube especially, if the SN explosion occurs at the Galactic center (Tamborra et al., 2013). The accretion rates also increase due to these instabilities, which enhance the neutrino emission in the accretion phase.

Recently, some studies show that not only the hydrodynamic instabilities but also the corrections for neutrino reaction rates help the explosion.

1. Nucleon recoil
   ν_x's are emitted by the thermal pair emission, i.e., electron-positron pair annihilation and nucleon bremsstrhlung. However, the neutrino sphere for ν_x's is decided by neutrino-nucleon scatterings (Raffelt, 2001):

   $$\nu + N \longrightarrow \nu + N. \tag{1.41}$$

   Although the energy exchange per nucleon is very small because nucleons have larger mass $\mu_n = 939.56$ MeV than the typical neutrino energy $\sim 30-40$ MeV, the number of nucleons is large enough that neutrino-nucleon scatterings dominate the other reactions in the thermalization for ν_x's. If we take the nucleon recoils of neutrino-nucleon scatterings into account, the difference of the average energy between ν_e, $\bar{\nu}_e$ and ν_x's becomes smaller (Raffelt, 2001). The energy exchanges between neutrinos and matters are important for the other reactions for ν_e's and $\bar{\nu}_e$'s. If we take the nucleon recoils into account for the reaction rates of charged current reactions, for example EC's on free protons, the opacities for neutrinos become smaller, which increase the neutrino luminosities and help the SN explosion (Müller et al., 2013).

2. Weak magnetism
   Weak magnetism is a higher order correction for the axial vector current of neutrino-nucleon interactions in the Weinberg-Salam theory. This correction reduces the opacity for neutrinos and increases for anti-neutrinos (Horowitz, 2002). The increase of ν_e's luminosity due to the opacity reduction enhances the heating behind the shock wave, which overcomes smaller absorption rates of $\bar{\nu}_e$'s. Weak magnetism also reduces the cooling via PC's on neutrons further, increasing the net heating behind the shock wave. These features not only enhance the explodability of SN but also change the condition of electron fraction Y_e and nucleosynthesis (Horowitz and Li, 1999).

3. Strange-quark effects
   In the Weinberg-Salam theory, the existence of quarks confined inside hadrons is also included in interactions with neutrinos effectively. We usually neglect the components of strange-quarks calculating cross sections. Strange-quarks are expected to increase the cross section for neutrino-proton scatterings and decrease that for neutrino-neutron scatterings. These changes reduce opacities by 10-20% depending on the condition of electron fraction (Melson et al., 2015) and help the SN explosion. Note that this correction does not contribute to charged current reactions.

Although there are numerous realistic dynamical SN simulations in the context of explodabilities, some missing points still remain. One is neutrino oscillations,

which may swap and split the neutrino spectrum between electron and heavy-lepton neutrinos (See Section 1.4) and change the heating rates behind the shock wave. It is difficult for neutrino oscillations to be taken into the dynamical simulations, because the oscillations have too short length scale to be resolved in the simulations. The second is the distinction between ν_μ, ν_τ, $\bar{\nu}_\mu$ and $\bar{\nu}_\tau$, which are usually put together as ν_x. As I explained, weak magnetism correction gives the opposite effects to neutrinos and anti-neutrinos. Moreover, Bollig et al. (2017) pointed out muons were created inside the PNS at the density 4×10^{14} g/cm^3 $\lesssim \rho \lesssim 2 \times 10^{13}$ g/cm^3 because the temperature $T \sim 30$ MeV is high enough to create muons via electron-positron or photon annihilations. Due to the creation of muons, ν_μ's and $\bar{\nu}_\mu$'s can interact with matters via the charged current reactions:

$$\nu_\mu + n \leftrightarrows p + \mu^- \tag{1.42}$$

$$\bar{\nu}_\mu + p \leftrightarrows n + \mu^+, \tag{1.43}$$

which enhance the PNS cooling and the shock heating. Neutrino oscillations also become one of the important reasons for the distinction of heavy-lepton flavors.

PNS cooling

After the matter accretion stops by the shock revival, the PNS is cooled down by neutrinos gradually. In this phase, neutrinos are emitted via the thermal pair emission inside the PNS for ∼10 s as I mentioned in Section 1.2.4. We divide neutrino luminosities into two components: the gravitational energy released by the matter accretion and the PNS cooling (Thompson et al., 2003). Although the accretion component dominates in the early phase ($t_{pb} \sim 100$ ms), the cooling component dominates after the shock wave begins to propagate and the matter accretion stops (Nakazato et al., 2013). The luminosity of ν_x's measured at infinity is well fitted using the Stefan-Boltzmann relation:

$$L_{\nu_x} = 4\pi\phi\sigma_\nu T_\nu^4 R_\nu^2, \tag{1.44}$$

with $\sigma_\nu = 4.75 \times 10^{35}$ erg/MeV^4/cm^2/s and the effective temperature and radius at the neutrino sphere T_ν and R_ν. We usually take the numerical factor $\phi \sim 0.4$-0.8 (Müller and Janka, 2014). The luminosities of ν_e's and $\bar{\nu}_e$'s, on the other hand, are described as

$$L_{\nu_e} + L_{\bar{\nu}_e} = 2\beta_1 L_{\nu_x} + \beta_2 \frac{GM_{\rm PNS}\dot{M}}{R_{\rm PNS}}. \tag{1.45}$$

The first term corresponds to the cooling component and the second term corresponds to the accretion component. If we take the numerical factors $\beta_1 \sim 1$ and $\beta_2 \sim 0.5 - 1$, the luminosities in the accretion phase derived from numerical simulations can be constructed (Müller and Janka, 2014).

The thermal pair emission, i.e. electron-positron pair annihilation and nucleon bremsstrhlung, contributes to the neutrino emission of ν_x's as well as in the accretion phase. The situations of the emission of ν_e's and $\bar{\nu}_e$'s are, however, change with the cooling of the PNS gradually. Because of the degeneracy of neutrons inside the PNS,

charged current reactions are suppressed and neutral current reactions have a large contribution to electron-type neutrinos (Fischer et al., 2012). This feature appears in the luminosity of $\bar{\nu}_e$'s at earlier time $t_{pb} \sim 20$ s.

The hierarchy of average energy is $\langle E_{\nu_e} \rangle < \langle E_{\bar{\nu}_e} \rangle < \langle E_{\nu_x} \rangle$ as well as in the accretion phase. They decrease with the coolig of the PNS in Figure 1.10. The opacities for $\bar{\nu}_e$'s and ν_x's come from neutrino-nucleon scatterings mainly at $t_{pb} \sim 1$ s. The absorption by neutrons is, on the other hand, the dominant opacity for ν_e's at this time. In the later time, neutrino-nucleon scatterings have same contribution to the opacities as neutron absorptions due to the Pauli-blocking of neutrons in the high density region.

1.4 Neutrino oscillation

From the recent experiments using solar neutrinos (Smy et al., 2004), atmospheric neutrinos (Ashie et al., 2005) and reactor neutrinos (Abe et al., 2014b), it is certain that neutrinos have finite masses. Although they are small enough not to affect the calculations of reaction rates, neutrinos can convert their flavor during propagation when mass eigenstates and flavor eigenstates do not match. The phenomenon of the conversion between neutrino flavors is called "neutrino oscillation". The neutrino spectra and luminosities observed at the earth are different from those emitted inside stars and we have to take this phenomenon into account for discussing observations of pre-SN and SN neutrinos. The absolute values of masses in the mass eigenstates have not been measured yet and there are two possibilities for the order of masses: normal hierarchy and inverted hierarchy shown in Figure 1.11.

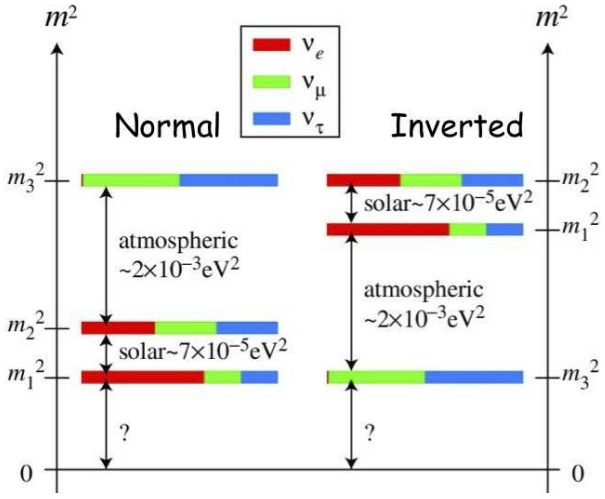

Figure 1.11: The possible orderings for neutrino masses. (Yang, 2015)

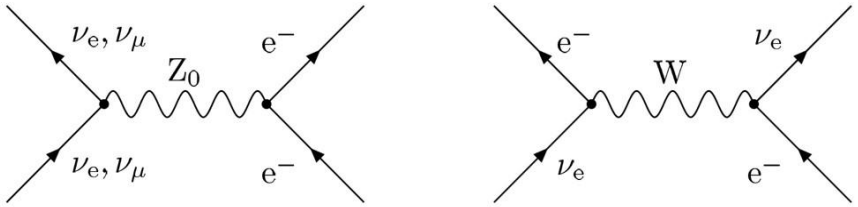

Figure 1.12: The type of neutrino interactions with electrons, i.e. charged current reactions (left panel) and neutral current reactions (right panel).

1.4.1 Basic equations

The flavor eigenstates $|\nu_\alpha\rangle$ are described by the linear summation of the mass eigenstates $|\nu_i\rangle$ using the mixing matrix U:

$$|\nu_\alpha\rangle = \Sigma_i U^*_{\alpha i} |\nu_i\rangle. \tag{1.46}$$

The evolution of flavor conversions follows the Schrödinger equation in the mass eigenstates:

$$i\frac{\partial}{\partial t}|\nu(t)\rangle = (H_0 + V)\,|\nu(t)\rangle, \tag{1.47}$$

with the Hamiltonian H_0 and the potential V. The equation for the flavor eigenstates $\nu_\alpha(t) \equiv \langle\nu_\alpha|\nu(t)\rangle$,

$$i\frac{\partial \nu_\alpha(t)}{\partial t} = \Sigma_\beta \left(\Sigma_{ij} U_{\alpha i} E_i \delta_{ij} U^\dagger_{j\beta} + V_\alpha \delta_{\alpha\beta}\right) \nu_\beta(t), \tag{1.48}$$

using the eigen equations $H_0|\nu_i\rangle = E_i|\nu_i\rangle$ and $V|\nu_\alpha\rangle = V_\alpha|\nu_\alpha\rangle$. In matrix form, it is written as

$$\begin{aligned} i\frac{\partial}{\partial t}\begin{pmatrix} \nu_e(t) \\ \nu_\mu(t) \\ \nu_\tau(t) \end{pmatrix} &= \left[U \begin{pmatrix} E_1 & 0 & 0 \\ 0 & E_2 & 0 \\ 0 & 0 & E_3 \end{pmatrix} U^\dagger + \begin{pmatrix} V_e & 0 & 0 \\ 0 & V_\mu & 0 \\ 0 & 0 & V_\tau \end{pmatrix} \right] \begin{pmatrix} \nu_e(t) \\ \nu_\mu(t) \\ \nu_\tau(t) \end{pmatrix} \\ &\equiv H \begin{pmatrix} \nu_e(t) \\ \nu_\mu(t) \\ \nu_\tau(t) \end{pmatrix}. \end{aligned} \tag{1.49}$$

The reactions, which contribute to the potential V_α, are divided into charged current interactions and neutral current interactions shown in Figure 1.12. Electron flavors interact with matters via both interactions $V_e = V_{\rm CC} + V_{\rm NC}$, whereas heavy-lepton flavors interact only via the neutral current interactions $V_{\mu,\tau} = V_{\rm NC}$. The energies $E_i = \sqrt{p^2 + m_i^2}$ can be approximated as $E_i \sim p + m_i^2/2p \sim E + m_i^2/2E$, because the neutrino masses m_i are small.

Vacuum oscillation

When neutrinos propagate in vacuum, the matter potentials become $V_{\rm CC}, V_{\rm NC} = 0$. The equations become simpler and we can analyze them easily. I explain the analysis of flavor conversions in the case of two flavors, i.e. ν_e and ν_x. The Schrödinger equation is

$$\begin{aligned} i\frac{\partial}{\partial t}\begin{pmatrix} \nu_e(t) \\ \nu_x(t) \end{pmatrix} &= H \begin{pmatrix} \nu_e(t) \\ \nu_x(t) \end{pmatrix} \\ H &= \left(E + \frac{m_1^2 + m_2^2}{4E}\right) I + \frac{\Delta m^2}{4E}\begin{pmatrix} -\cos 2\theta & \sin 2\theta \\ \sin 2\theta & \cos 2\theta \end{pmatrix} \end{aligned} \tag{1.50}$$

where the mass difference $\Delta m^2 = m_2^2 - m_1^2$ and the mixing matrix in the case of two flavors U:

$$U = \begin{pmatrix} \cos\theta & \sin\theta \\ -\sin\theta & \cos\theta \end{pmatrix}, \tag{1.51}$$

using the mixing angle θ. Since the first term of the Hamiltonian H can be included in the phase, we redefine the equation as

$$i\frac{\partial}{\partial t}\begin{pmatrix} \nu_e(t) \\ \nu_x(t) \end{pmatrix} = \frac{\Delta m^2}{4E}\begin{pmatrix} -\cos 2\theta & \sin 2\theta \\ \sin 2\theta & \cos 2\theta \end{pmatrix}\begin{pmatrix} \nu_e(t) \\ \nu_x(t) \end{pmatrix}. \tag{1.52}$$

Note that the wave functions ν_α in the above equation are different from those in eq. (1.50). The solution is $\vec{\nu}(t) = e^{-iH't}\vec{\nu}(0)$ where

$$\vec{\nu}(t) = \begin{pmatrix} \nu_e(t) \\ \nu_x(t) \end{pmatrix}, \tag{1.53}$$

$$H' = \frac{\Delta m^2}{4E}\begin{pmatrix} -\cos 2\theta & \sin 2\theta \\ \sin 2\theta & \cos 2\theta \end{pmatrix}. \tag{1.54}$$

If we assume all neutrinos are electron flavor initially, i.e. $\vec{\nu}(0) = (1, 0)$,

$$\vec{\nu}(t) = \begin{pmatrix} \cos\frac{\Delta m^2}{4E}t + i\sin\frac{\Delta m^2}{4E}t\cos 2\theta \\ -i\sin\frac{\Delta m^2}{4E}t\sin 2\theta \end{pmatrix}. \tag{1.55}$$

The probability that neutrinos are observed as electron flavor after t sec, or the survival probability, P_{ee} is

$$P_{ee} = |\nu_e(t)|^2 = 1 - \sin^2\frac{\Delta m^2}{4E}t\sin^2 2\theta. \tag{1.56}$$

We can find the neutrino oscillation occurs with the length $l_{\rm osc} = 4\pi E/\Delta m^2$.

MSW effect

If neutrinos propagate through matters, the potentials have finite values and the Hamiltonian of the Schrödinger equation is described as:

$$H = \left(E + \frac{m_1^2 + m_2^2}{4E} + V_{\rm NC} \right) I + \begin{pmatrix} -\frac{\Delta m^2}{4E}\cos 2\theta + V_{\rm CC} & \frac{\Delta m^2}{4E}\sin 2\theta \\ \frac{\Delta m^2}{4E}\sin 2\theta & \frac{\Delta m^2}{4E}\cos 2\theta \end{pmatrix}. \quad (1.57)$$

As only the second term is related with the neutrino oscillation, the neutral current reactions do not affect it. We define several variables in order that we describe the Schrödinger equation for the mass eigenstates in the diagonalized form:

$$i\frac{\partial}{\partial t}\vec{\nu}_m = H_m \vec{\nu}_m, \quad (1.58)$$

$$H_m \equiv U_m^\dagger H U_m = \begin{pmatrix} E_{m1} & 0 \\ 0 & E_{m2} \end{pmatrix}, \quad (1.59)$$

$$U_m \equiv \begin{pmatrix} \cos\theta_m & \sin\theta_m \\ -\sin\theta_m & \cos\theta_m \end{pmatrix}, \quad (1.60)$$

$$E_{m1,m2} \equiv E + V_{\rm NC} + \frac{m^2_{m1,m2}}{2E}, \quad (1.61)$$

$$m^2_{m1,m2} \equiv \frac{m_1^2 + m_2^2}{2} + \frac{A}{2} \mp \frac{\Delta m_m^2}{2}, \quad (1.62)$$

$$\Delta m_m^2 \equiv \sqrt{(A - \Delta m^2 \cos 2\theta)^2 + (\Delta m^2 \sin 2\theta)^2}, \quad (1.63)$$

$$A \equiv 2EV_{\rm CC} = 2\sqrt{2}G_F n_e E, \quad (1.64)$$

$$\tan 2\theta_m = \frac{\sin 2\theta}{\cos 2\theta - \frac{2E}{\Delta m^2}V_{\rm CC}}. \quad (1.65)$$

In the limit that the number density becomes $n_e \to 0$, these equations are equal to those of the vacuum case, or $m^2_{m1} \to m_1^2, m^2_{m2} \to m_2^2, \theta_m \to \theta$. While in the limit $n_e \to \infty$, $m^2_{m1} \to m_1^2 \sin^2\theta + m_2^2 \cos^2\theta, m^2_{m2} \to A, \theta_m \to \pi/2$. In Figure 1.13, the dependence of the number density for the square masses is shown. Including the matter potentials, the mass eigenstates are changed with the number density. This is called a "Mikheyev-Sumirnov-Wolfenstein (MSW)" effect. If we consider the situation in which neutrinos are emitted from a high density region and propagate to vacuum, the conditions $\nu_1 \sim \nu_\mu$, $\nu_2 \sim \nu_e$ are satisfied initially.

We find that two mass eigenstates are close at the number density N_e^c in Figure 1.13. This point is called a "resonance point" and the most likely to occur flavor conversions. The resonance density N_e^c is described as

$$N_e^c = \frac{\Delta m^2 \cos 2\theta}{2\sqrt{2}G_F E}, \quad (1.66)$$

where the mixing angle becomes $\theta_m = \pi/2$, and we also get the mass difference $\Delta m^2_{m0} = \Delta m^2 \sin 2\theta$ and the oscillation lengh $l_{\rm osc0} = l_{\rm osc}/\sin 2\theta$.

The diagonalization of the Hamiltonian in the mass eigenstates can be achieved when neutrino oscillations occur in the shorter timescale than that for the variation of the electron number density. This approximation is called an "adiabatic

approximation" and the criterion:

$$\gamma \equiv \frac{l_{n_e}}{l_{osc0}} = \frac{\Delta m^2 \sin^2 2\theta}{2E\frac{1}{n_e}|\frac{dn_e}{dr}|\cos 2\theta} \gg 1. \tag{1.67}$$

should be satisfied. We have to take care about the flavor conversions at the resonance points, because the mass difference Δm^2 becomes smaller and there is a possibility that we cannot use the adiabatic approximation. In this case, we have to solve the Schrödinger equation with the non-diagonal components of the Hamiltonian.

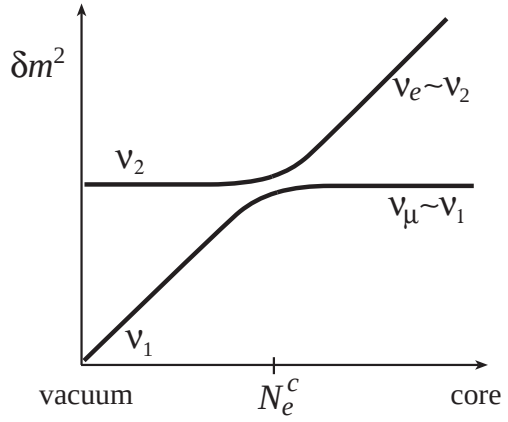

Figure 1.13: The two-flavor level diagram for neutrino propagation from a core to vacuum. The vertical line δm^2 corresponds to Δm^2 in my prescriptions. (Barger et al., 2003)

If we consider pre-SN or SN neutrinos, we have to extend flavor conversions among three flavors. The Schrödinger equation only for the terms related to flavor conversions becomes

$$i\frac{\partial}{\partial t}\begin{pmatrix}\nu_e(t)\\ \nu_\mu(t)\\ \nu_\tau(t)\end{pmatrix} = \left[U\begin{pmatrix}0 & 0 & 0\\ 0 & \frac{\Delta m^2_{21}}{2E} & 0\\ 0 & 0 & \frac{\Delta m^2_{31}}{2E}\end{pmatrix}U^\dagger + \begin{pmatrix}\sqrt{2}G_F n_e & 0 & 0\\ 0 & 0 & 0\\ 0 & 0 & 0\end{pmatrix}\right]\begin{pmatrix}\nu_e(t)\\ \nu_\mu(t)\\ \nu_\tau(t)\end{pmatrix}. \tag{1.68}$$

In this expression, we use the matrix element in the case of three flavor:

$$\begin{aligned} U &= \begin{pmatrix} U_{e1} & U_{e2} & U_{e3}\\ U_{\mu 1} & U_{\mu 2} & U_{\mu 3}\\ U_{\tau 1} & U_{\tau 2} & U_{\tau 3}\end{pmatrix}\\ &= \begin{pmatrix} C_{12}C_{13} & S_{12}C_{13} & S_{13}\\ -S_{12}C_{23} - C_{12}S_{23}S_{13} & C_{12}S_{23} - S_{12}S_{23}S_{13} & S_{23}C_{13}\\ S_{12}S_{23} - C_{12}S_{23}S_{13} & -C_{12}S_{23} - S_{12}C_{23}S_{13} & C_{23}C_{13}\end{pmatrix}, \end{aligned} \tag{1.69}$$

with $C_{ij} \equiv \cos\theta_{ij}$ and $S_{ij} \equiv \sin\theta_{ij}$ and we neglect the CP phase $\delta = 0$.

The mass eigenstates in the case of three flavors are shown in Figure 1.14. The left panel shows the case of the normal hierarchy, whereas the right panel shows the inverted hierarchy. For $\bar{\nu}_e$'s, the matter potential becomes negative $V_{\rm CC} = -\sqrt{2}G_F n_e$

and their mass eigenstates correspond to the left part of each panel. In the high density limit, the mass eigenstates match to the flavor eigenstates: $\nu_e \sim \nu_3$, $\nu_\mu \sim \nu_1$ and $\nu_\tau \sim \nu_2$ for the normal hierarchy and $\nu_e \sim \nu_2$, $\nu_\mu \sim \nu_1$ and $\nu_\tau \sim \nu_3$ for the inverted hierarchy. We find two resonance points in Figure 1.14. One is called "H resonance" related to the mass difference between ν_1 and ν_2 and the other is called "L resonance" related to the mass difference between ν_2 and ν_3. The densities of two resonance points are $\rho_L \sim 4 \times 10$ g/cm^3 and $\rho_H \sim 3 \times 10^3$ g/cm^3 for neutrinos with 10 MeV, respectively. It is known that we can treat L resonance as adiabatic, whereas H resonance is not. In the progenitors of ECSNe with the steep density gradient or in the shock propagation phase, the flavor conversions occur with a finite probability P_H at the H resonance point (Mirizzi et al., 2016).

The observed fluxes at the Earth are described using the survival probabilities P and $\bar{P}$ for ν_e's and $\bar{\nu}_e$'s, respectively:

$$F_{\nu_e}(E) = P(E) F^0_{\nu_e} + (1 - P(E)) F^0_{\nu_x}, \tag{1.70}$$

$$F_{\bar{\nu}_e}(E) = \bar{P}(E) F^0_{\bar{\nu}_e} + \left(1 - \bar{P}(E)\right) F^0_{\bar{\nu}_x}, \tag{1.71}$$

where F^0_* denotes the initial fluxes of neutrinos. The survival probabilities are summarized in Table 1.4.1.

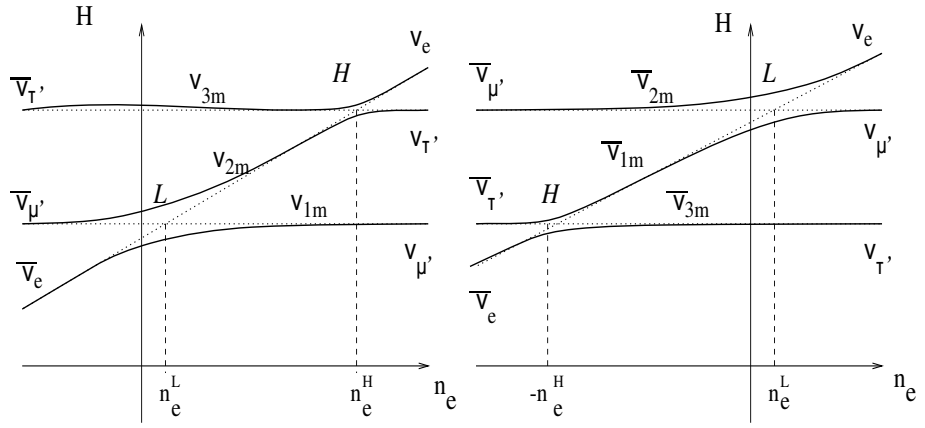

Figure 1.14: The three-flavor level diagram for the propagation of ν_e's and $\bar{\nu}_e$'s from a SN core to vacuum. The left panel shows the diagram for the normal hierarchy, while the right panel shows that for the inverted hierarchy. The matter potentials for ν_e's and $\bar{\nu}_e$'s have opposite sign and the diagram for $n_e < 0$ corresponds to the propagation for $\bar{\nu}_e$'s. (Raffelt, 2012)

Table 1.2: The survival probabilities for ν_e's and $\bar{\nu}_e$'s.

	P	$\bar{P}$
NH	$P_H \sin^2\theta_{12}$	$\cos^2\theta_{12}$
IH	$\sin^2\theta_{12}$	$\bar{P}_H \cos^2\theta_{12}$

Collective oscillation

Neutrino-neutrino interactions cannot be neglected at the high density and then we have to take the neutrino-neutrino potential into account. This effect is called a "collective oscillation". Its Hamiltonian is described as

$$V_{\nu\nu} = \sqrt{2}G_F \int \frac{d^3\mathbf{p}'}{(2\pi)^3} v \cdot v' \left[\rho\left(t, \mathbf{r}, \mathbf{p}'\right) - \bar{\rho}\left(t, \mathbf{r}, \mathbf{p}'\right)\right], \tag{1.72}$$

with the velocity of neutrinos with a finite mass v and the density matrices ρ and $\bar{\rho}$ for ν_e's and $\bar{\nu}_e$'s, respectively. Due to the conservation of lepton numbers, the conversions occur as "pair conversions" $\nu_e\bar{\nu}_e \rightarrow \nu_x\bar{\nu}_x$. When the neutrino-neutrino potential $\mu = \sqrt{2}G_F\left(n_{\nu_e} - n_{\nu_x}\right)$ becomes larger than the matter potential $\lambda = \sqrt{2}G_F\left(n_e - n_{e^+}\right)$, the collective oscillations become important to get the neutrino spectrum.

Since the Hamiltonian includes the neutrino number density, the Schrödinger equation becomes nonlinear and it is difficult to solve it analytically. We usually analyze the collective effects using some approximations, for example, so-called "single-angle" approximation in which we regard a single angular mode as the representative of all the neutrino ensembles (Duan et al., 2006b). Under this approximation, the spectra are changed by the collective oscillations in Figure 1.15. In the case of the inverted hierarchy, the spectra are splitting at $E_{\rm split} \sim 10$ MeV ("spectrum split") and the fluxes are fully exchanged between electron and heavy-lepton neutrinos above this energy ("spectrum swap") (Mirizzi et al., 2016). There are similar features in the spectra of $\bar{\nu}_e$, but above the split energy $E_{\rm splirt} \sim 3$ MeV. The collective effects do not appear in the case of the normal hierarchy.

Recently, multi-angle effects are investigated using the "bulb model" (Duan et al., 2006a), in which neutrinos are emitted from the neutrino sphere uniformly and half-isotropically and it is assumed that there is azimuthal symmetry of the neutrino emission and that the hydrodynamic backgrounds only depend on the radius r. In the neutronization and accretion phases, these effects can be negligible or become sub-leading because of the large flavor hierarchy, whereas more complicated features by the multi-angle effects appear in the spectra in the cooling phase because neutrinos have a moderate flavor hierarchy of fluxes (Esteban-Pretel et al., 2007). The features of the spectral splits and swaps are suppressed by the decoherence of the multi-angle effects.

Although there are many analytical studies about the effects of the collective oscillations for neutrino spectra, they have not been investigated for the three flavor case yet so far. Some studies show a new instability is triggered when we remove the assumption of axial symmetry in the neutrino propagation (Chakraborty and Mirizzi, 2014). It was, however, claimed that faster flavor conversion may occur around the neutrino sphere due to the difference of the angular distribution between ν_e's and $\bar{\nu}_e$'s (Sawyer, 2016). That may change the neutrino spectra behind the shock wave and affect the shock heating. It is one of the hottest topics in the studies of SN neutrinos.

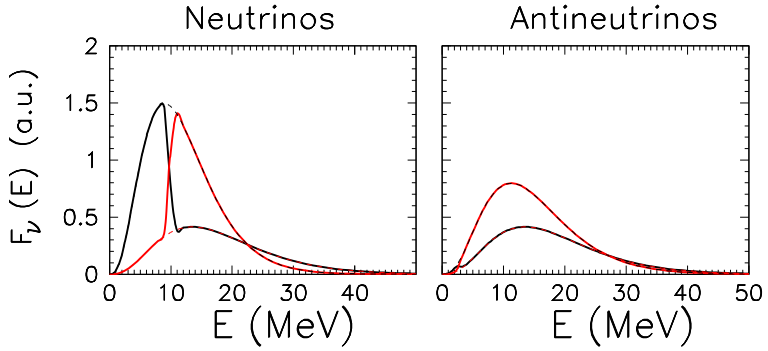

Figure 1.15: The neutrino spectra derived from the two-flavor single-angle simulation in the inverted hierarchy for an initial flux ordering $F^0_{\nu_e} : F^0_{\bar{\nu}_e} : F^0_{\nu_x} = 2.40 : 1.60 : 1.0$. The initial energy spectra for electron neutrinos (black, dashed) and heavy-lepton neutrinos (red, dashed) and after the collective oscillations for electron neutrinos (black, solid) and heavy-lepton neutrinos (red, solid) at $r = 350$ km. (Mirizzi et al., 2016)

1.5 Neutrino observation

A big breakthrough came in neutrino observations at the supernova event SN1987A. The massive star with $\sim 20 M_\odot$ exploded ~ 50 kpc from the Earth in the Large Magellanic Cloud. Their lights arrived at the Earth on February 23, 1987. At the same time, 11 neutrinos were detected during 12 s at the KAMIOKANDE-II (Hirata et al., 1987). From their data, we found the average energy of neutrinos $\langle E_\nu \rangle \sim 10$ MeV and the total luminosity of neutrinos $L_\nu \sim 10^{53}$ erg. These outcomes were consistent with the delayed explosion mechanism, or the neutrino heating mechanism, and had an important role to understand the SN explosions (Sato and Suzuki, 1987). It has been about 30 years since the SN1987A event and neutrino detectors have been developed and the expected number of events in the next galactic SN is more than 10^5. It is expected that the next neutrino events will give constraint on progenitor models, formation scenarios of compact objects, EOS, nucleosynthesis of heavy elements and so on. In this section, I explain how to detect neutrinos and recent preparations of terrestrial detectors for the next galactic SNe.

1.5.1 Mechanism of neutrino detection

We need some special ways to detect neutrinos, because they interact with matters only via weak interactions and their cross sections are small.

Water Cherenkov detectors

Although no matter can be over the speed of light c in vacuum, it becomes c/n using the refractive index n in medium because of the refraction and matters can propagate faster than the speed of light. This is a necessary condition for the emission of Cherenkov lights. Their intensities get stronger along with their frequency, so they look blue. Neutrinos interact with matters in pure water of detectors and produced

charged particles, mainly electrons or positrons, radiate the Cherenkov lights during propagation through the water. These lights are detected at photo-multipliers (PMTs) attached to the wall of the detectors and are converted to electrical signals.

Currently, all the detectors utilize inverse β decays and electron scatterings for the detection of neutrinos. The most powerful tool to detect $\bar{\nu}_e$'s is the inverse β decays:

$$\bar{\nu}_e + p \longrightarrow e^+ + n, \tag{1.73}$$

because there are many protons inside the water. The cross section of this reaction is described as follows:

$$\sigma_\beta(E_\nu) = 0.0952 \left(\frac{E_{e^+} p_{e^+}}{1\mathrm{MeV}^2} \right) \times 10^{-42} \quad \mathrm{cm}^2, \tag{1.74}$$

in which the energy and 3-momentum of the positron are denoted by $E_{e^+} = E_\nu - (m_n - m_p)$ and $p_{e^+} = \sqrt{{E_{e^+}}^2 - {m_e}^2}$, respectively (Odrzywolek et al., 2004).

For the detection of the other neutrino flavors, the neutrino-electron scatterings are used:

$$\nu + e^- \longrightarrow \nu + e^- \tag{1.75}$$

All neutrino flavors can cause this reaction, but the cross section is quite smaller than that of the inverse β decay. Since forward scatterings are dominant because electrons are relativistic, we can determine the directions of neutrinos.

Super-Kamiokande (Abe et al., 2014a) is the largest detector whose fiducial volume is 32 kt at present. The low background technique using neutron capture on gadolinium is being developed to confirm the inverse β decay event precisely (See Section 1.5.2). Moreover, Hyper-Kamiokande (Abe et al., 2018), whose volume is about 20 times larger than that of SK, will run within 10 years. We can expect more events at the future SN events than those at the SN1987A and get much information about sources of neutrinos.

Liquid scintillator detectors

The charged particles, which are emitted via the inverse β decay mainly, excite emission media and we detect their scintillation lights instead of Cherenkov radiations. Although these media cost more than pure waters, the intensity of scintillation lights is 100 times larger than that of Cherenkov lights and we can detect scintillation lights more easily. Moreover, the neutron emitted via the inverse β decay is thermalized by elastic scatterings and captured by proton with γ rays finally:

$$p + n \longrightarrow d + \gamma. \tag{1.76}$$

These γ rays are the delayed scintillation signals to the prompt signals by the charged particles and become the evidence of the inverse β decay. Then, the threshold becomes lower than that of the Cherenkov detectors and neutrinos with lower energy can be detected at the scintillation detectors. However, they are not good at the decision of the direction of neutrinos because the number of electrons are too small to cause the enough number of electron scatterings.

The representative detectors are KamLAND (Berger et al., 2009) and Borexino (Alimonti et al., 2009). The volume of KamLAND, which is the largest volume of the current detectors, is still 1 kt and several larger detectors are being planned in the future, for example SNO+ (Kraus and Peeters, 2010), LENA (Wurm et al., 2012) and JUNO (An et al., 2016).

Liquid argon detectors

Electron neutrinos are normally detected via electron-scattering: $\nu_e + e^- \longrightarrow \nu_e + e^-$, in the currently available detectors as I explained. Its reaction rate is much lower than that of the inverse β decay, however, and the detection of ν_e's in the pre-bounce phase has been thought to be almost impossible. Then the new-type detector using liquid argon has come into view. Deep Underground Neutrino Observatory (DUNE) is a liquid argon detector currently planned to be constructed in 10 years at SURF (Sanford Underground Research Facility) (Acciarri et al., 2016). It deploys 4 detectors filled with liquid argon of 10 kt each and employs the absorption of ν_e by ^{40}Ar:

$$^{40}\mathrm{Ar} + \nu_e \longrightarrow e^- + {}^{40}\mathrm{K}^*. \tag{1.77}$$

Although the detection of SN neutrinos emitted after the core bounce is one of the main targets of DUNE, it should be noted that its energy threshold will be low enough (~ 5 MeV) to detect ν_e's from the progenitors before the SN explosion.

1.5.2 Recent progress of neutrino detectors and preparation for the next supernova event

GADOOKS!

Recently, in order to reduce backgrounds at Super-Kamiokande, the project in which gadolinium will be doped to the pure water, called "GADOOKS!", is planned (Beacom and Vagins, 2004). After the detection of the Cherenkov radiations by the inverse β decay, γ rays which are emitted with ~ 8 MeV by the capture of neutrons on gadolinium reach PMTs about 30 μs later (See Figure 1.16). The coincidence of two signals confirms the inverse β decay and the lower energy threshold is achieved. The main target of this project is to detect SN relic neutrinos, which are emitted from the historical SNe and whose intensities are very low. Moreover, the other reactions except the inverse β decays, i.e. electron scatterings, are distinguishable and we can determine the directions of neutrino sources more precisely. The EGADS experiment was done at the Kamioka mine and the expected influences by adding gadolinium to Super-Kamiokande were investigated. From this October, the doping of gadolinium to the tank of SK was already started.

Coherent scattering by nuclei

We need other reactions to detect ν_x's, which interact with matters only via neutral current reactions. The coherent elastic neutrino-nucleus scattering is one of the candidate reaction:

$$\nu + (A, Z) \longrightarrow \nu + (A, Z). \tag{1.78}$$

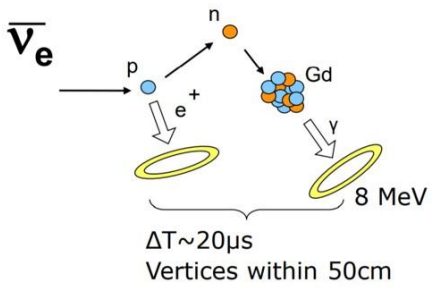

Figure 1.16: The delayed coincidence by gadolinium at the water Cherenkov detectors. (Sekiya, 2017)

We can detect lights from recoiled nuclei. The nuclei with the larger mass number have the larger cross section, but the smaller recoil with $\sim$ a few keV, typically. Although its detection was supposed to be difficult, it was detected using the neutrinos from the spallation neutron source at OaK Ridge National laboratory in 2017 (Akimov et al., 2017). It was the latest breakthrough in the neutrino detection.

SNEWS

As I mentioned, we can get much information about the mechanism of SN explosion or PNS cooling from neutrino observations. The SN rate in our galaxy is, however, once per 100 or 1000 years unfortunately and we never miss the next SN event. The "SuperNova Early Waring System (SNEWS)" is one of the biggest projects as a preparation for the next galactic SN including theorists and experimentalists (Scholberg, 2000). In this system, if there is a coincidence between several events within 10 sec window, a warning alarm is issued. From SN explosions, not only neutrinos but also electromagnetic waves and gravitational waves are emitted. The SNEWS may have a role as a mediation between these different detectors and lead the multi-messenger studies of SN explosions.

Chapter 2

Pre-supernova neutrinos

2.1 Purpose

Neutrinos play an important role in the SN explosions and their progenitor evolutions. In fact, the neutrino heating mechanism is thought to be the currently most promising scenario to revive a stalled shock and produce a successful explosion. CCSNe are one of the most important cosmic neutrino sources from an observational point of view as corroborated by the observation of neutrinos from SN1987A at terrestrial neutrino detectors such as Kamiokande. Before core collapse, on the other hand, neutrinos dominate photons in the stellar cooling after C-burning. As the central temperature and density increase in the progenitor, the number and energy of pre-SN neutrinos also rise. While SN neutrinos are released with several tens of MeV, however, pre-SN neutrinos are mainly emitted with several MeV. Therefore, it is difficult to distinguish them from the background of detectors, and it has never been focused in the observational point of view so far. The low background technology, however, have been developed at SK and DUNE, which will be able to detect ν_e's, is under construction. There is hence a possibility of detecting pre-SN neutrinos from neighborhood ($\sim$ kpc).

In this study, I consider two types of progenitors that are supposed to produce CCSNe: FeCCSNe and ECSNe. Since the evolutions of the central density and temperature in both progenitors are greatly different at the late phase, I discuss whether they can be discriminated from the observations of pre-SN neutrinos. I focus on the observations of not only ν_e's but also $\bar{\nu}_e$'s and discuss their importances for understanding of the stellar evolutions and neutrino physics.

The neutrino emission at different phases, i.e., the progenitor phase, pre-/post-bounce phases and PNS-cooling phase, have been investigated separately so far. Considering, however, the recent progress in the numerical modeling of CCSNe, in which we observe successful explosions rather commonly, I believe that these phases should be handled consistently, based on successful supernova models. This study is the first step in this direction and I attempt to calculate neutrino emission from the progenitor stage up to the pre-bounce time, at which the central density becomes $\rho_c = 10^{13}$ g/cm^3, consistently and seamlessly. The subsequent evolutions of the same models will be studied later.

2.2 Models

In this calculation I consider neutrino emission during both the quasi-static evolutions of progenitors and the hydrodynamical core-collapse. I stop the calculations at the time when the central density reaches $\rho_c = 10^{13}$ g/cm^3. For the former I use the stellar evolution models as described in Section 2.2.1 whereas for the latter I conduct one-dimensional simulations under spherical symmetry, solving radiation-hydrodynamics equations as explained in Section 2.2.2. Note that we need to take into account neutrino transport in the core properly once the density becomes high enough to trap neutrinos. The two evolutionary phases are connected at the time when the central density becomes $\rho_c = 10^{10.3}$ g/cm^3 for FeCCSNe and $10^{10.1}$ g/cm^3 for ECSNe, respectively.

2.2.1 Quasi-static evolutions of progenitors

I employ three progenitor models with $M_{\rm ZAMS} = 9$, 12 and 15 $M_\odot$, which were calculated anew by Takahashi (Takahashi et al., 2013; Takahashi et al., 2016). The first one produces an ONe-core that is supposed to explode as ECSN, while the last two models explode as FeCCSNe if they really succeed to. The latter two models with 12 and 15 $M_\odot$ are indeed identical to those employed in Yoshida et al. (2016) but calculated until the central temperature reaches 10^{10} K with hydrodynamics taken into account.

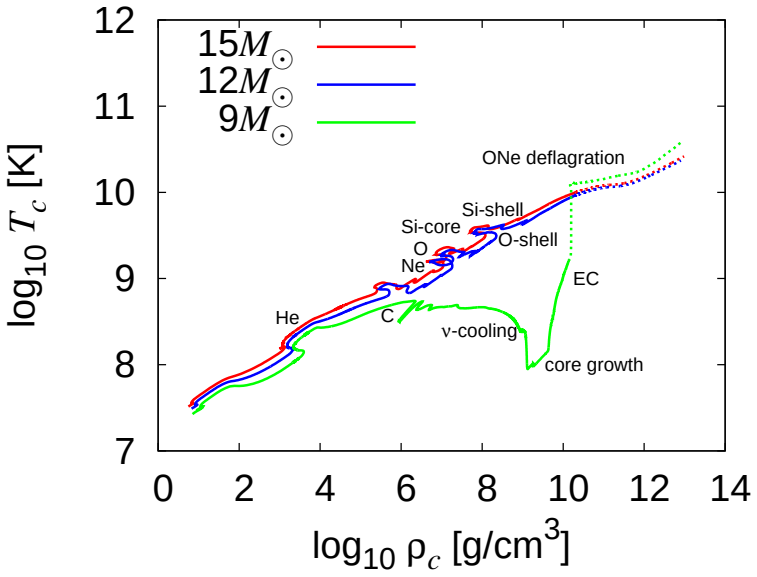

Figure 2.1: The evolutionary paths of the central density and temperature for three progenitors. The red, blue and green curves correspond to the 15, 12 and 9 $M_\odot$ models, respectively. The evolutions in both the progenitor phase (solid lines) and the collapse phase (dotted lines) are presented. The initiation points of some major nuclear-burnings as well as the evolutionary stages defined by Takahashi et al. (2013) for the ONe-core progenitors are marked with labels.

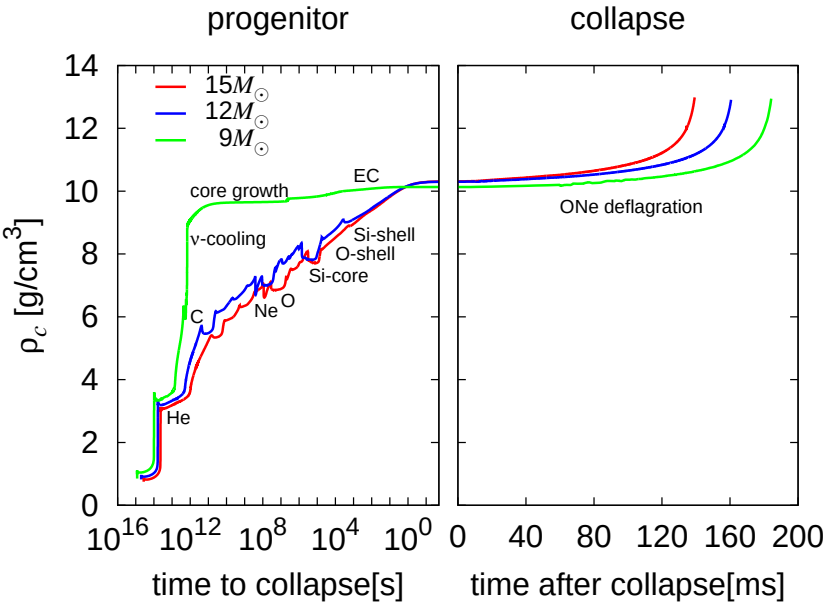

Figure 2.2: The evolutions of the central density as functions of time for the three progenitors. The red, blue and green curves correspond to the 15, 12 and 9 $M_\odot$ models, respectively. The origin of the horizontal axis corresponds to the time, at which the dynamical simulations are started. The initiation points of some major nuclear-burnings as well as the evolutionary stages for the ONe-core progenitors are marked with labels.

Here I summarize the evolutions of these models briefly. Figure 2.1 shows the evolutions of the central density and temperature of the progenitors. The solid lines represent the results of the quasi-static stellar-evolutionary calculations, or "progenitor phase" , whereas the dashed lines correspond to those of the core-collapse simulations, or "collapse phase". In this figure, we also mark the initiation points of major nuclear-burning stages, which are defined to be the points when the element of relevance is ignited at the center; for the ONe-core case more detailed evolutionary stages are indicated as well, which are defined in Takahashi et al. (2013). We see that the two types of progenitors are not much different up to the end of C-burning ($\rho = 10^6$ g/cm^3). After that, however, the evolutionary paths are deviated remarkably from each other. The progenitors with 12 and 15 $M_\odot$ proceed further to burn heavier nuclei stably under the supports of not only thermal but also degenerate pressures and their central densities and temperatures increase gradually up to collapse. In the case of the progenitor with $M_{\rm ZAMS} = 9\ M_\odot$, on the other hand, the Ne-burning does not occur immediately, since the temperature does not become high enough after the C-burning. The core is cooled by neutrino emission and the central temperature is lowered as the ONe-core grows via the shell C-burning and the central density increases. When it reaches the critical value ($\rho = 10^{9.88}$ g/cm^3) for the EC on ^{24}Mg, then the core starts to contract with a shorter time scale and the central temperature also begins to rise again. The contraction is accelerated considerably when the EC on ^{20}Ne sets in at $\rho = 10^{10.3}$ g/cm^3, accompanied by a rapid rise of the central temperature. Finally, Ne and O are ignited at the center

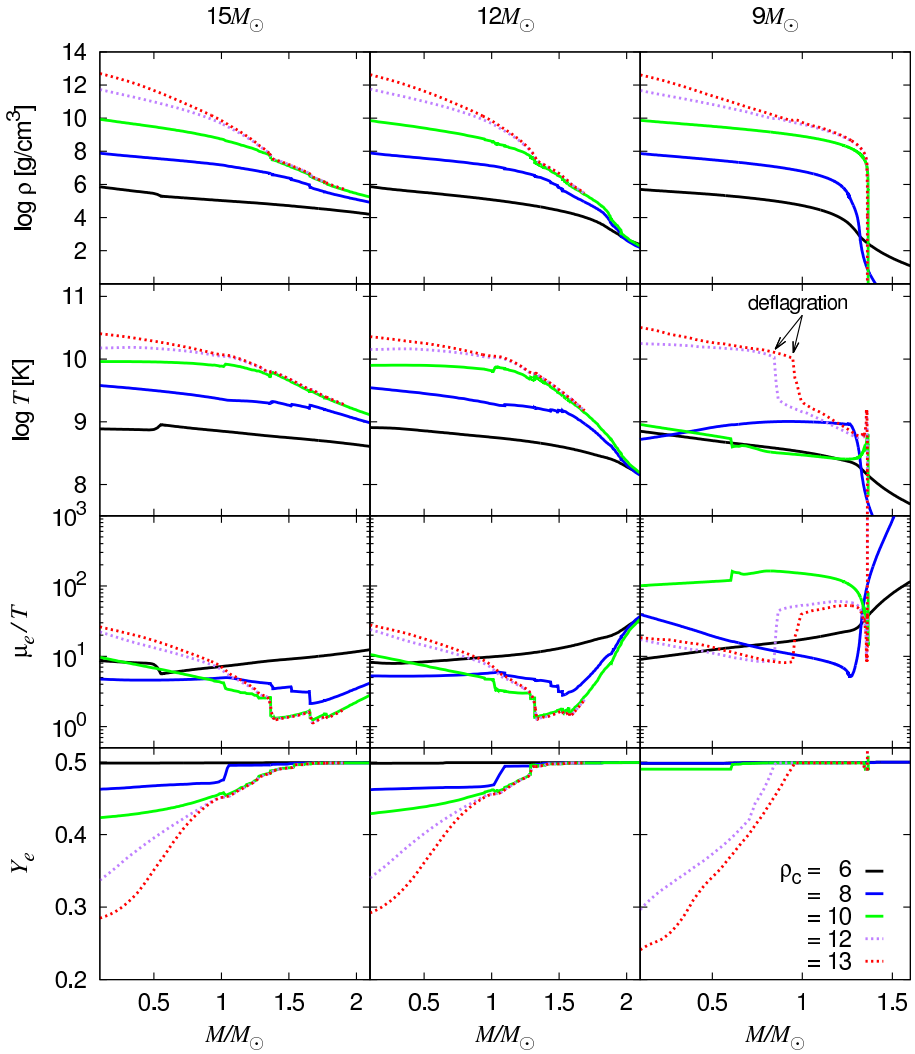

Figure 2.3: The radial profiles of density, temperature, degeneracy, electron fraction at different times. The horizontal axis is the mass coordinate in the solar-mass unit. The left, middle and right columns correspond to the 15, 12 and 9 $M_\odot$ models, respectively. Different colors denote the times, at which the central density becomes $\rho_c = 10^6$ g/cm^3 (black solid), 8 (blue solid), 10 (green solid), 12 (purple dotted) and 13 (red dotted), respectively.

almost simultaneously and the flame front starts to propagate outward as a deflagration. The temperature increases drastically and the NSE is established soon after the passage of the burning front.

The evolutions of the central density for the three progenitors are shown in Figure 2.2. The origin of the time coordinate corresponds to the time, at which the hydrodynamical calculations are initiated. When a new nuclear burning starts, the core expands and the central density is lowered a bit. It is evident also in this figure that the pre-collapse evolution of the 9 $M_\odot$ progenitor is qualitatively different from the other two.

In Figure 2.3, the radial profiles of density ρ, temperature T, electron degeneracy μ_e/T, where μ_e is the chemical potential of electron, and electron fraction Y_e are plotted. The horizontal axis is the mass coordinate in the solar mass unit. Different colors correspond to different times, at which the central densities are $\rho_c = 10^6$, 10^8, 10^{10}, 10^{12} and 10^{13} g/cm^3, respectively. It is clear from the comparison between the progenitors of FeCCSNe and that of ECSN, the temperature profiles become different qualitatively at $\rho_c = 10^8$ g/cm^3. In the case of the 9 $M_\odot$ progenitor, the central part of the core is cooler than the outer part because of the neutrino cooling via plasmon decay. The degeneracy parameter μ_e/T is accordingly higher than those in the 12 and 15 $M_\odot$ models. Rather high electron fractions ($Y_e \sim 0.498$) at early times are a noteworthy feature for the ECSN progenitor. Although EC reactions trigger the core contraction, the change in Y_e is rather minor ($\Delta Y_e \sim 0.008$) in this phase and the main reduction of Y_e occurs only after NSE is established by the O+Ne deflagration.

2.2.2 Core collapse

Once the accelerated gravitational contraction happens after the EC on ^{20}Ne in the core, we have to abandon the quasi-static approximation and need to solve hydrodynamical equations numerically. As explained earlier, interactions of neutrinos with matter become non-negligible as the density increases and neutrinos are eventually trapped in the core. Then we need to take into account the transport of neutrinos appropriately. I hence employ the 1-dimensional hydrodynamical code with a Boltzmann solver developed by Nagakura et al. (2014, 2017) to follow the evolution of core collapse. The hydrodynamics solver is explicit and of second-order accuracy in both space and time, based on the so-called central scheme (Kurganov and Tadmor, 2000; Nagakura and Yamada, 2008; Nagakura et al., 2011); the spherical coordinates are adopted; the Newtonian self-gravity is taken into account. The Boltzmann solver adopts the discrete-ordinate method, or the S_N scheme (Mezzacappa and Bruenn, 1993a; Liebendörfer et al., 2004; Sumiyoshi et al., 2005), finite-differencing both space and momentum space; it is semi-implicit in time; special relativity is fully accounted for by utilizing the two different energy grids: Lagrangian-remapped and laboratory-fixed grids. Although we normally deploy 12-15 energy grid points spaced logarithmically between 1-300 MeV in this sort of simulations, I increase the number to 20, extending at the same time the energy range to lower values 0.1 MeV in this study so that I could obtain better resolution at these low energies. See Nagakura et al. (2014) for more details.

I use Furusawa's EOS (Furusawa et al., 2013), a multi-nuclear species EOS, which is based on the relativistic mean field theory with the TM1 parameter set employed in H. Shen's EOS, or STOS EOS (Shen et al., 2011); it takes into account the NSE among $\sim 8.7 \times 10^5$ nuclides and nucleons by extending a nuclear mass formula (Audi et al., 2012; Koura et al., 2005); electron capture rates for heavy nuclei are also provided by this EOS at high densities (see below).

In the neutrino transport, the following reactions are taken into account in this calculation:

- neutrino emission and absorption: electron captures on nuclei and free nucleons, electron-positron annihilations, nucleon-bremsstrahlungs and their inverse reactions.

- neutrino scattering: isoenergetic scatterings on free nucleons, coherent scatterings on nuclei and non-isoenergetic scatterings on electrons and positrons.

The reaction rates are based on Bruenn (1985) and Mezzacappa and Bruenn (1993b) except for the EC on heavy nuclei, for which we take the values provided by Fuller et al. (1985); Oda et al. (1994); Langanke and Martínez-Pinedo (2001) and Langanke et al. (2003), which are referred to as FFN, ODA, LMP and LMSH, respectively, and average them over the NSE abundance of nuclei given by the EOS. I also employ the approximation formula (see eq. (2.42) below) when none of the tables provides the rate. The luminosity and energy spectrum of ν_e in the collapse phase are obtained directly from the simulations whereas those for other neutrino species are calculated in the post processes (see the next section).

I use for the dynamical simulations only the radial profiles of central cores derived from the quasi-static evolutions of the progenitors. For the Fe-cores of the 12 and 15 $M_\odot$ models, I start the computations from the time when the central density is $\rho_c = 10^{10.3}$ g/cm^3. I first run the Boltzmann solver alone with all quantities other than the neutrino distribution functions being fixed until steady states are reached. This step is necessary to avoid artificial discontinuities in the neutrino luminosities at the point of the switch to the dynamical calculations. The 9 $M_\odot$ model needs a special treatment. As already mentioned, the gravitational contraction starts in the ONe-core via EC. Neons and oxygens are then ignited at the center and the deflagration wave propagates outward in the core, establishing NSE behind. Note that NSE already prevails in the Fe-cores. In the case of the ONe-core, we hence have to handle this nuclear equilibration process, solving network equations in addition to the hydrodynamics and neutrino transport. This has been done recently by Takahashi et al. (2018) and I will use their results in this calculation. I here give important information alone: they modified the 1D radiation-hydrodynamics code developed by Sumiyoshi and Yamada (2012) to compute the nuclear reactions with a network of 49 nuclear species; H. Shen's original EOS is employed instead of Furusawa's extended version; EC rates are adopted from Juodagalvis et al. (2008); Juodagalvis et al. (2010). The radial profile at the time of $\rho_c = 10^{10.1}$ g/cm^3 is used as the initial condition for the simulation. The wave front of the deflagration is described as the discontinuity surface in terms of temperature and chemical composition. The propagation speed is determined by the temperature increase due to adiabatic compression and neutrino-electron scatterings.

In all three cases, I terminate the simulations when the central density exceeds $\rho_c = 10^{13}$ g/cm^3. This is because nuclei become very large thereafter and pastas are supposed to emerge eventually toward core bounce (Ravenhall et al., 1983); then the EC rates on these nuclei are highly uncertain and treated only crudely in the original radiation-hydrodynamics code.

The dotted lines in Figures 2.1 and 2.3 show the evolutions in the collapse phase. The behavior of the central temperature and density in this phase is not much different between the two types of progenitors. In the 9 $M_\odot$ progenitor, however, the temperature is high only inside the deflagration front, which is located at the mass coordinate of ~ 1 $M_\odot$ in Figure 2.3. The NSE condition ($T \gtrsim 5 \times 10^9$ K) is achieved indeed and the degeneracy of electrons is partially lifted there. It is also evident that EC is drastically enhanced once NSE is established. Note in passing that the differences in Y_e between the ONe-core and Fe-cores presented here may partially reflect the differences in the EOS and EC rates adopted in these models.

2.3 Neutrino emission

Neutrinos are emitted via several processes, which are classified into thermal pair emission and nuclear weak interaction as I explained in Section 1.3. In this section, I first describe somewhat in detail the formulae I employ to evaluate the neutrino emissivity for individual processes (§§ 2.3.1-2.3.4). In order to discuss the possibility of observations at terrestrial detectors, flavor oscillations should be taken into account and will be discussed in Section 2.3.5. In the progenitor phase, I simply evaluate the luminosities and spectra of all flavors of neutrinos in post processes, i.e., I extract density-, temperature- and electron fraction profiles from the data obtained in the stellar evolution calculations and core-collapse simulations at appropriate times from $\sim 10^6$ s to a few ms before core bounce. Then I calculate the neutrino emissivities for the thermal pair productions and nuclear weak interactions (See Table.2.1) pointwise and integrate the results outwards from the center of the star until the number luminosities do not change appreciably $\sim 10^{-6}$%.

In the collapse phase, on the other hand, I treat ν_e differently from the other flavors of neutrinos: the luminosity and spectrum of ν_e are derived directly from the radiation-hydrodynamical simulations, since we have to take into account neutrino transport when the opacity for neutrinos gets high enough to hinder their free escape. Note that ν_e's are responsible for the transfer of the electron-type lepton number and hence the evolution of Y_e, and their transport in the core is indispensable for realistic supernova simulations.

Other species of neutrinos in the collapse phase, on the other hand, are treated in post-processes, i.e., I first run simulations neglecting these reactions[1]; I then extract the densities, temperatures and electron fractions as well as the distribution function of ν_e from results of the simulations and plug them into the formulae of emissivities given in the following subsections. Note that the distribution function of ν_e is necessary to take into account the Fermi-blocking in the final state. I

[1]The productions and absorptions of neutrinos via the electron-positron pair annihilations are *included* in the simulations of core collapse. The resolution of the energy spectra obtained in the simulations are rather low, however, and I re-construct them in the post-process.

ignore the transport of these neutrinos, since they are much less abundant than ν_e. In fact, I compare the emissivities of $\bar{\nu}_e$ via β^- decay inside the opaque part of the core ($\rho > 10^{11.5}$ g/cm^3) with those in the whole NSE regions at the time when the central density is $\rho_c = 10^{13}$ g/cm^3 and find that the former contributes only $\sim$0.001% to the total neutrino emissivities because of the high-degeneracy of electrons there. The emission of these neutrinos after matter becomes opaque are hence negligible compared with those before that. The neutrino emission processes and their treatments in my calculations are summarized in Table. 2.1.

Table 2.1: Neutrino reactions considered in this calculation. The forth column gives the treatment of each process in the collapse phase: "T" means that the transport is considered whereas "P" stands for the post-process and "-" implies that the process is neglected. The fifth column lists the color-codes used consistently in Figures 2.7-2.11.

	reactions		collapse phase	colors
thermal	pair	$e^- + e^+ \longrightarrow \nu + \bar{\nu}$	ν_e:T, others:P	red
processes	plasmon	$\gamma^* \longrightarrow \nu + \bar{\nu}$	-	brown
nuclear	EC	$(Z, A) + e^- \longrightarrow (Z-1, A) + \nu_e$	T	black
processes	β^+	$(Z, A) \longrightarrow (Z-1, A) + e^+ + \nu_e$	-	purple
	PC	$(Z, A) + e^+ \longrightarrow (Z+1, A) + \bar{\nu}_e$	P	orange
	β^-	$(Z, A) \longrightarrow (Z+1, A) + e^- + \bar{\nu}_e$	P	green
	free p	$p + e^- \longrightarrow n + \nu_e$	T	blue

2.3.1 Thermal emission of neutrino pairs

As shown in Figure 1.9, I found that the electron-positron pair annihilation is always dominant for the FeCCSN-progenitors with 12 and 15 $M_\odot$, while for the ONeCCSN-progenitor with 9 $M_\odot$ the plasmon decay prevails until Ne and O are ignited at the center and the temperature rises quickly, after which the pair annihilation takes over. See also Patton et al. (2017) and Guo and Qian (2016).

Electron-positron pair annihilation

The number R of reactions to produce the pair of neutrino and anti-neutrino with four momenta $q^\mu = (E_\nu, \boldsymbol{q})$ and $q'^\mu = (E_{\bar{\nu}}, \boldsymbol{q}')$, respectively, per unit time and unit volume[2] is given by the following equation in the natural unit ($c = \hbar = 1$):

$$R = \left(\frac{G_F}{\sqrt{2}}\right)^2 \iint \frac{d^3k}{(2\pi)^3\, 2E_e} \frac{d^3k'}{(2\pi)^3\, 2E'_e} (2\pi)^4\, \delta^4\left(q + q' - k - k'\right) f_{e^-}\left(E_e\right) f_{e^+}\left(E'_e\right)\, 64\, |M|^2\,, \tag{2.1}$$

[2] R is actually a differential number and $Rd^3q/2E_\nu d^3q'/2E_{\bar{\nu}}$ is the true number of reactions per time and volume. See eq. (2.14).

in which $k^\mu = (E_e, \boldsymbol{k})$ and $k'^\mu = (E'_e, \boldsymbol{k}')$ are the 4-momenta for electron and positron, respectively; f_{e^-} and f_{e^+} are the Fermi-Dirac distribution functions of electron and positron, respectively; the matrix element squared for this reaction is expressed as

$$|M|^2 = (C_V - C_A)^2 (q \cdot k)(q' \cdot k') + (C_V + C_A)^2 (q \cdot k')(q' \cdot k) + {m_e}^2 (C_V - C_A)^2 (q \cdot q')^2 . \tag{2.2}$$

In this equation, the coupling constants are given as $C_V = 1/2 + 2\sin^2\theta_w$ and $C_A = 1/2$ with $\sin^2\theta_w = 0.2224$ for the Weinberg angle θ_w. Note that all neutrinos are assumed to be massless, which is well justified for my purposes.

The expression of R in eq. (2.1) can be cast into the following form (Mezzacappa and Bruenn, 1993b; Schinder and Shapiro, 1982):

$$R = \frac{8G_F^2}{(2\pi)^2} [\, \beta_1 I_1 + \beta_2 I_2 + \beta_3 I_3 \,]. \tag{2.3}$$

In the above expression, β's are the following combinations of the coupling constants: $\beta_1 = (C_V - C_A)^2$, $\beta_2 = (C_V + C_A)^2$ and $\beta_3 = C_V^2 - C_A^2$, and I's are the functions of the energies of emitted neutrino E_ν and anti-neutrino $E_{\bar\nu}$ and the angle ψ between their momenta $\boldsymbol{q}$ and $\boldsymbol{q}'$:

$$\begin{aligned} I_1(E_\nu, E_{\bar\nu}, \cos\psi) = & -\frac{2\pi T E_\nu^2 {E_{\bar\nu}}^2 (1-\cos\psi)^2}{\left[\exp\left(\frac{E_\nu + E_{\bar\nu}}{T}\right) - 1\right] {\Delta_e}^5} \\ & \times \left\{ AT^2 \left([G_2(y_{\max}) - G_2(y_{\min})] \right.\right. \\ & \quad + [2y_{\max} G_1(y_{\max}) - 2y_{\min} G_1(y_{\min})] \\ & \quad \left.\left. + \left[y_{\max}^2 G_0(y_{\max}) - y_{\min}^2 G_0(y_{\min}) \right] \right) \right. \\ & + BT \left([G_1(y_{\max}) - G_1(y_{\min})] + [y_{\max} G_0(y_{\max}) - y_{\min} G_0(y_{\min})] \right) \\ & \left. + C [G_0(y_{\max}) - G_0(y_{\min})] \right\}, \end{aligned} \tag{2.4}$$

$$I_2 = I_1(E_{\bar\nu}, E_\nu, \cos\psi), \tag{2.5}$$

$$I_3 = -\frac{2\pi T m_e^2 E_\nu E_{\bar\nu} (1-\cos\psi)}{\left[\exp\left(\frac{E_\nu + E_{\bar\nu}}{T}\right) - 1\right] \Delta_e} [G_0(y_{\max}) - G_0(y_{\min})], \tag{2.6}$$

with

$${\Delta_e}^2 \equiv {E_{\bar\nu}}^2 + {E_\nu}^2 + 2E_\nu E_{\bar\nu} \cos\psi, \tag{2.7}$$

$$A \equiv {E_{\bar\nu}}^2 + {E_\nu}^2 - E_\nu E_{\bar\nu} (3 + \cos\psi), \tag{2.8}$$

$$B \equiv E_\nu \left[-2{E_\nu}^2 + {E_{\bar\nu}}^2 (1 + 3\cos\psi) + E_\nu E_{\bar\nu} (3 - \cos\psi) \right], \tag{2.9}$$

$$C \equiv E_\nu^2 \left[(E_\nu + E_{\bar\nu}\cos\psi)^2 - \frac{1}{2}{E_{\bar\nu}}^2 \left(1 - \cos^2\psi\right) - \frac{1}{2}\left(\frac{m_e \Delta_e}{E_\nu}\right)^2 \frac{1+\cos\psi}{1-\cos\psi} \right], \tag{2.10}$$

and $\eta' = (\mu_e + E_\nu + E_{\bar\nu})/T$, $\eta = \mu_e/T$, $y_{\max} = E_{\max}/T$, $y_{\min} = E_{\min}/T$ and $G_n(y) \equiv F_n(\eta' - y) - F_n(\eta - y)$, in which the Fermi integral $F_n(z)$ is defined as

$$F_n(z) = \int_0^\infty \frac{x^n}{e^{x-z} + 1} dx; \tag{2.11}$$

η_e denotes the chemical potential of electron; the Boltzmann's constant is taken to be unity in these and following equations. The detail of the derivation of these expressions is given in Appendix.

The number spectrum for the neutrino or anti-neutrino (denoted by ν_1) is expressed as an integral of R over the momentum of the partner (referred to as ν_2) as follows:

$$\frac{dQ_N^{\nu_1}}{dE_{\nu_1}} = \frac{E_{\nu_1}}{(2\pi)^2} \iint \frac{d^3q_{\nu_2}}{(2\pi)^3 2E_{\nu_2}} R(E_\nu, E_{\bar{\nu}}, \cos\psi). \tag{2.12}$$

Note that ν_1 may be ν or $\bar{\nu}$ and the natural unit is employed here. The corresponding energy spectrum is just obtained as

$$\frac{dQ_E^{\nu_1}}{dE_{\nu_1}} = E_{\nu_1} \frac{dQ_N^{\nu_1}}{dE_{\nu_1}}. \tag{2.13}$$

The total number emissivity is found by further integrating $dQ_N^{\nu_1}/dE_{\nu_1}$ over E_{ν_1} as

$$Q_N^{\nu_1} = \int dE_{\nu_1} \frac{dQ_N^{\nu_1}}{dE_{\nu_1}} = \iint \frac{d^3q}{(2\pi)^3 2E_\nu} \frac{d^3q'}{(2\pi)^3 2E_{\bar{\nu}}} R(E_\nu, E_{\bar{\nu}}, \cos\psi), \tag{2.14}$$

and the corresponding energy emissivity Q_E is obtained similarly:

$$Q_E^{\nu_1} = \int dE_{\nu_1} \frac{dQ_E^{\nu_1}}{dE_{\nu_1}} = \iint \frac{d^3q}{(2\pi)^3 2E_\nu} \frac{d^3q'}{(2\pi)^3 2E_{\bar{\nu}}} E_{\nu_1} R(E_\nu, E_{\bar{\nu}}, \cos\psi). \tag{2.15}$$

Finally the energy loss rate for this reaction is given by the sum of the energy emissivities over all neutrino species:

$$Q = \sum_{\nu}^{\text{all species}} Q_E^{\nu}. \tag{2.16}$$

In the collapse phase as the matter density increases and the neutrino energy rises, interactions between matter and neutrinos become no longer ignored. Electron-type neutrinos, the most abundant species, are eventually trapped in the core at $\rho \gtrsim 10^{11}$ g/cm^3 and become degenerate. Then the pair creation of ν_e and $\bar{\nu}_e$ is suppressed by the Fermi-blocking in the final state. Considering the inverse process, I should hence modify the differential emissivity of $\bar{\nu}_e$ in this phase as

$$\begin{aligned} \frac{dQ_N^{\bar{\nu}_e}}{dE_{\bar{\nu}_e} d\cos\psi_{\bar{\nu}_e} d\phi_{\bar{\nu}_e}} &= \frac{E_{\bar{\nu}_e}}{2(2\pi)^3} \int \frac{d^3q_{\nu_e}}{(2\pi)^3 2E_{\nu_e}} \\ &\times \left[R^p\left(E_{\nu_e}, E_{\bar{\nu}_e}, \cos\psi\right) \left[1 - f_{\nu_e}\left(E_{\nu_e}, \theta_{\nu_e}\right)\right] \left[1 - f_{\bar{\nu}_e}\left(E_{\bar{\nu}_e}, \theta_{\bar{\nu}_e}\right)\right] \right. \\ &\left. - R^a\left(E_{\nu_e}, E_{\bar{\nu}_e}, \cos\psi\right) f_{\nu_e}\left(E_{\nu_e}, \theta_{\nu_e}\right) f_{\bar{\nu}_e}\left(E_{\bar{\nu}_e}, \theta_{\bar{\nu}_e}\right) \right], \end{aligned} \tag{2.17}$$

where f_{ν_e} and $f_{\bar{\nu}_e}$ are the distribution functions of ν_e and $\bar{\nu}_e$, respectively. The direction of neutrino momentum is specified with the zenith and azimuth angles (θ_ν,ϕ_ν) with respective to the local radial direction. The first term in the integrand on the right hand side is the production rate whereas the second term represents the absorption rate for the inverse reaction: R_p is given by eq. (2.1) while R_a is obtained from R_p via the detailed balance condition: $R_a = R_p \exp((E_\nu + E_{\bar{\nu}})/T)$. I make an approximation $1 - f_{\bar{\nu}_e}\left(E_{\bar{\nu}_e}, \theta_{\bar{\nu}_e}\right) \sim 1$, which is well justified as $f_{\bar{\nu}_e}\left(E_{\bar{\nu}_e}, \theta_{\bar{\nu}_e}\right)$ is small in the collapse phase.

Moreover, we have to take into account matter motions in the collapse phase and distinguish the global inertial frame, or the observer's frame, from the local fluid-rest frame, since the emissivities I have presented so far are all valid in the latter frame. The emissivities in the observer's frame is obtained by the following transformation:

$$\frac{dQ_N^{\bar{\nu}_e}}{dE_{\bar{\nu}_e}^{\rm lab} d\cos\theta_{\bar{\nu}_e}^{\rm lab} d\phi_{\bar{\nu}_e}^{\rm lab}} = J \frac{dQ_N^{\bar{\nu}_e}}{dE_{\bar{\nu}_e}^{\rm fr} d\cos\theta_{\bar{\nu}_e}^{\rm fr} d\phi_{\bar{\nu}_e}^{\rm fr}}, \tag{2.18}$$

where the superscripts "lab" and "fr" stand for quantities in the laboratory and fluid-rest frames, respectively, and J is the Jacobian:

$$J = \frac{\partial\left(E_{\bar{\nu}_e}^{\rm fr}, \cos\theta_{\bar{\nu}_e}^{\rm fr}, \phi_{\bar{\nu}_e}^{\rm fr}\right)}{\partial\left(E_{\bar{\nu}_e}^{\rm lab}, \cos\theta_{\bar{\nu}_e}^{\rm lab}, \phi_{\bar{\nu}_e}^{\rm lab}\right)}, \tag{2.19}$$

for the following transformations:

$$E^{\rm fr} = E^{\rm lab}\gamma\left(1 - \vec{n}^{\rm lab}\cdot\vec{v}\right), \tag{2.20}$$

$$\vec{n}^{\rm fr} = \frac{1}{\gamma\left(1-\vec{n}^{\rm lab}\right)}\left[\vec{n}^{\rm lab} + \left(-\gamma + \frac{\gamma-1}{v^2}\vec{v}\cdot\vec{n}^{\rm lab}\right)\right], \tag{2.21}$$

with $\vec{n}^{\rm lab} = (\sin\theta_\nu\cos\phi_\nu, \sin\theta_\nu\sin\phi_\nu, \cos\theta_\nu)$ being the propagation direction of neutrino.

The left panels of Figure 2.4 show the number spectra, eq. (2.12), of $\bar{\nu}_e$'s for different combinations of ρY_e and T. In the top panel, the value of ρY_e is varied around $\rho Y_e = 10^{10}$ g/cm^3 with the value of T being fixed to $T = 10^{10}$ K, whereas the latter is changed for a fixed value of the former ($\rho Y_e = 10^{10}$ g/cm^3) in the bottom panel. It is evident that the emissivity is very sensitive to temperature. In fact, as the temperature increases by ~ 20 %, the peak number luminosity becomes greater by an order of magnitude. This is simply because the number of electron-positron pairs increases as $\propto T^3$. It is also observed that the average energy increases as the temperature rises. The dependence on ρY_e is much less drastic: the emissivity decreases with the value of ρY_e, since the number of electron-positron pairs is reduced in this case.

For a later comparison, I give here the fitting formula for the energy loss rate Q proposed by (Itoh et al., 1996):

$$\begin{aligned} Q_{\rm pair} &= \frac{1}{2}\left[\left(C_V{}^2 + C_A{}^2\right) + 2\left(C_V'{}^2 + C_A'{}^2\right) + \left\{\left(C_V{}^2 - C_A{}^2\right) + 2\left(C_V'{}^2 - C_A'{}^2\right)\right\} q_{\rm pair}\right] \\ &\times\ g(\lambda)\, e^{-\frac{2}{\lambda}}\, f_{\rm pair}, \end{aligned} \tag{2.22}$$

In which the coupling constants are defined as $C_V' = 1 - C_V$ and $C_A' = 1 - C_A$, and $q_{\rm pair}$, $g\left(\lambda\right)$ and $f_{\rm pair}$ are expressed, respectively, as

$$\begin{aligned} q_{\rm pair} &= \left(10.7480\lambda^2 + 0.3967\lambda^{0.5} + 1.0050\right)^{-1.0} \\ &\quad \times \left[1 + \left(\frac{\rho}{\mu_e}\right)\left(7.692\times10^7\lambda^3 + 9.715\times10^6\lambda^{0.5}\right)^{-1.0}\right]^{-0.3}, \end{aligned} \tag{2.23}$$

$$g\left(\lambda\right) = 1 - 13.04\lambda^2 + 133.5\lambda^4 + 1534\lambda^6 + 918.6\lambda^8, \tag{2.24}$$

$$f_{\rm pair} = \frac{\left(a_0 + a_1\xi + a_2\xi^2\right)e^{-c\xi}}{\xi^3 + b_1\lambda^{-1} + b_2\lambda^{-2} + b_3\lambda^{-3}}, \tag{2.25}$$

with

$$\lambda = \frac{T}{5.9302 \times 10^9 \text{ K}}, \quad \xi = \left(\frac{\rho/\mu_e}{10^9 \ g/cm^3} \right)^{\frac{1}{3}} \lambda^{-1}. \tag{2.26}$$

This fitting formula is supposed to be accurate within 10 % of error in the regime, where the electron-positron pair annihilation is dominant over other neutrino-emitting processes. In the left panel of Figure 2.5, I compare the energy loss rates obtained by the formulae given above (eqs. (2.15) and (2.16)) with those given by the fitting formula, (eq. (2.22)) for different densities and a fixed temperature ($T = 10^{10}$ K) and electron fraction ($Y_e = 0.5$). Only the contribution from electron-type neutrinos is taken into account in this comparison. It is apparent that they are in excellent agreement except at high densities $\rho \gtrsim 10^{10}$ g/cm^3, where the electron-positron annihilation is no longer dominant and the fitting formula is not accurate.

2.3.2 Plasmon decay

I calculate the neutrino emissivity via the plasmon decay, following Braaten and Segel (1993). The detailed derivations are given in Appendix. The number of reactions, R, to produce the pair of neutrino and anti-neutrino with the energies E_ν and $E_{\bar{\nu}}$, respectively, per unit time and volume, R, is given as[3]

$$\begin{aligned}
R = & \left(\frac{G}{\sqrt{2}} \right)^2 \frac{16 {C_V}^2}{e^2} \frac{2 {E_\nu}^2 {E_{\bar{\nu}}}^2 (1 - \cos\psi)}{\left[1 - \exp\left(\frac{E_\nu + E_{\bar{\nu}}}{T}\right)\right]} \\
& \times \left\{ \frac{3 {\omega_p}^2}{{\Delta_e}^2} \delta \left(f_L \left(E_\nu, E_{\bar{\nu}}, \cos\psi \right) \right) \left[\frac{E_\nu + E_{\bar{\nu}}}{2\Delta_e} \ln \frac{E_\nu + E_{\bar{\nu}} - \Delta_e}{E_\nu + E_{\bar{\nu}} + \Delta_e} + 1 \right] \right. \\
& \quad \times \left[-2 \cos\psi \left(E_\nu + E_{\bar{\nu}} \right)^2 - 2 E_\nu E_{\bar{\nu}} \sin\psi^2 + \frac{2 \left(E_\nu + E_{\bar{\nu}} \right)^2}{{\Delta_e}^2} \left(E_\nu + E_{\bar{\nu}} \cos\psi \right) \left(E_{\bar{\nu}} + E_\nu \cos\psi \right) \right] \\
& \quad - \frac{3 {\omega_p}^2 \left(E_\nu + E_{\bar{\nu}} \right)^2}{{\Delta_e}^2} \delta \left(f_T \left(E_\nu, E_{\bar{\nu}}, \cos\psi \right) \right) \left[1 + \frac{E_\nu E_{\bar{\nu}} (1 - \cos\psi)}{\left(E_\nu + E_{\bar{\nu}} \right) \Delta_e} \ln \frac{E_\nu + E_{\bar{\nu}} - \Delta_e}{E_\nu + E_{\bar{\nu}} + \Delta_e} \right] \\
& \quad \left. \times \left[1 - \frac{\left(E_\nu \cos\psi + E_{\bar{\nu}} \right) \left(E_{\bar{\nu}} \cos\psi + E_\nu \right)}{{\Delta_e}^2} \right] \right\}
\end{aligned} \tag{2.27}$$

with the following $f_L \left(E_\nu, E_{\bar{\nu}}, \cos\psi \right)$ and $f_T \left(E_\nu, E_{\bar{\nu}}, \cos\psi \right)$:

$$\begin{aligned}
f_L \left(E_\nu, E_{\bar{\nu}}, \cos\psi \right) = & \ 2 E_\nu E_{\bar{\nu}} (1 - \cos\psi) \\
& + 3 {\omega_p}^2 \frac{2 E_\nu E_{\bar{\nu}} (1 - \cos\psi)}{{\Delta_e}^2} \left\{ \frac{E_\nu + E_{\bar{\nu}}}{2\Delta_\nu} \ln \frac{E_\nu + E_{\bar{\nu}} - \Delta_e}{E_\nu + E_{\bar{\nu}} + \Delta_e} + 1 \right\}
\end{aligned} \tag{2.28}$$

$$\begin{aligned}
f_T \left(E_\nu, E_{\bar{\nu}}, \cos\psi \right) = & \ 2 E_\nu E_{\bar{\nu}} (1 - \cos\psi) \\
& - \frac{3}{2} {\omega_p}^2 \frac{\left(E_\nu + E_{\bar{\nu}} \right)^2}{{\Delta_e}^2} \left[1 + \frac{E_\nu E_{\bar{\nu}} (1 - \cos\psi)}{\left(E_\nu + E_{\bar{\nu}} \right) \Delta_e} \ln \frac{E_\nu + E_{\bar{\nu}} - \Delta_e}{E_\nu + E_{\bar{\nu}} + \Delta_e} \right]
\end{aligned} \tag{2.29}$$

Note that the dispersion relations of the longitudinal and transverse modes are obtained from $f_L \left(E_\nu, E_{\bar{\nu}}, \cos\psi \right) = 0$ and $f_T \left(E_\nu, E_{\bar{\nu}}, \cos\psi \right) = 0$, respectively.

[3] See footnote 2.

The number spectrum dQ_N^ν/dE_ν and total emissivities Q_N^ν and Q_E^ν as well as the energy loss rate Q are calculated in the same way as for the electron-positron pair annihilations by eqs. (2.12), (2.14), (2.15) and (2.16). The right panels of Figure 2.4 show the number spectra for different ρY_e (top panel) and temperatures (bottom panel). It is found from the figure that the number spectrum is much less sensitive to temperature than for the electron-positron pair annihilation but depends more on ρY_e. It is also evident that the peak energy is considerably smaller in the plasmon decay compared with the pair annihilation although the amplitudes are not so different between them. This fact has an important implication for observability of the neutrinos emitted by these processes on the terrestrial neutrino detectors.

The fitting formula to the energy loss rate was provided by Haft et al. (1994) in the following form:

$$Q_{\rm plasma} = \left({C_V}^2 + 2{C_V'}^2 \right) Q_V. \tag{2.30}$$

In the above expression Q_V is given as

$$Q_V = 3.00 \times 10^{21} \lambda^9 \gamma^6 e^{-\gamma} \left(f_T + f_L \right) f_{xy}, \tag{2.31}$$

in which the following notations are employed:

$$\gamma^2 = \frac{1.1095 \times 10^{11} \rho/\mu_e}{T^2 \left[1 + \left(1.019 \times 10^{-6} \rho/\mu_e \right)^{\frac{2}{3}} \right]^{\frac{1}{2}}} \tag{2.32}$$

$$f_T = 2.4 + 0.6\gamma^{\frac{1}{2}} + 0.51\gamma + 1.25\gamma^{\frac{3}{2}} \tag{2.33}$$

$$f_L = \frac{8.6\gamma^2 + 1.35\gamma^{\frac{7}{2}}}{225 - 17\gamma + \gamma^2} \tag{2.34}$$

$$x = \frac{1}{6} \left[17.5 + \log_{10} \left(2\rho/\mu_e \right) - 3 \log_{10} T \right] \tag{2.35}$$

$$y = \frac{1}{6} \left[-24.5 + \log_{10} \left(2\rho/\mu_e \right) + 3 \log_{10} T \right] \tag{2.36}$$

$$f_{xy} = \begin{cases} 1 \qquad (\text{for } |\mathrm{x}| > 0.7 \text{ or } \mathrm{y} < 0) \\ 1.05 + \left\{ 0.39 - 1.25x - 0.35 \sin\left(4.5x\right) - 0.3 \exp\left[-\left(4.5x + 0.9\right)^2 \right] \right\} \\ \quad \times \exp\left\{ -\left[\dfrac{\min\left(0, y - 1.6 + 1.25x\right)}{0.57 - 0.25x} \right]^2 \right\} \ (\text{for otherwise}) \end{cases} \tag{2.37}$$

The error of this fitting formula is less than 5 % in the regime, where the plasmon decay dominates in the cooling over other processes. I compared the energy loss rate obtained by our formula and that given by eq. (2.30) in the right panel of Fig. 2.5, in which the temperature is fixed to $T = 10^{10}$ K just as in the pair annihilation case. Again the contribution from electron-type neutrinos is taken into account in this comparison. It is apparent that they agree with each other excellently. Note that the plasmon decay is dominant at $\rho Y_e \gtrsim 10^{10}$ g/cm^3 (Itoh et al. 1996, Figure 1.9).

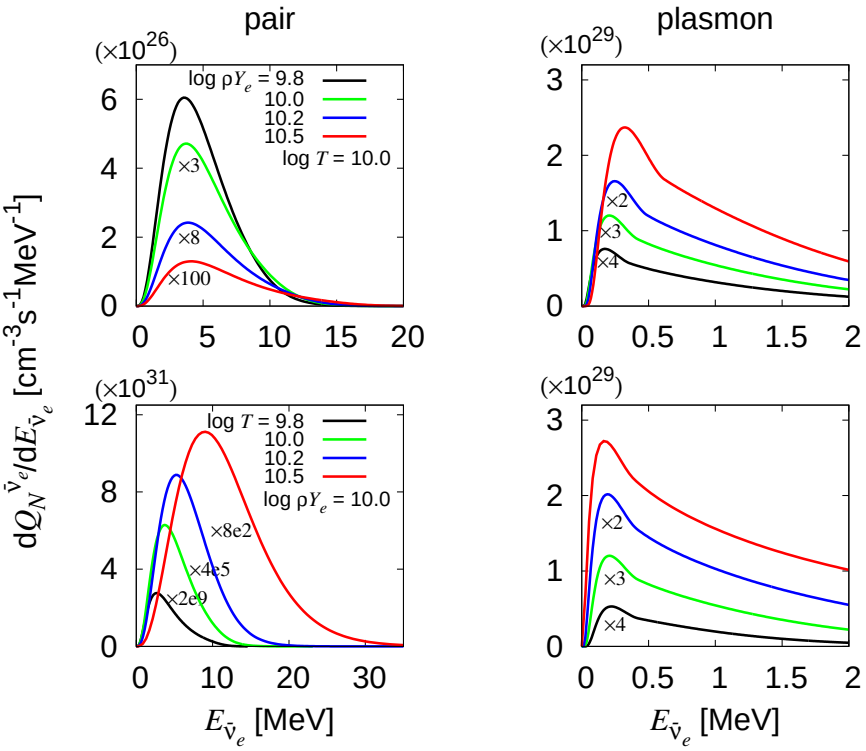

Figure 2.4: The number spectra of the pair annihilation (left panels) and the plasmon decay (right panels) for different combinations of ρY_e and T. The top panels show the dependence on ρY_e, in which T is fixed to 10^{10} K, whereas the lower panels display the dependence on T, where ρY_e is set to 10^{10} g/cm^3.

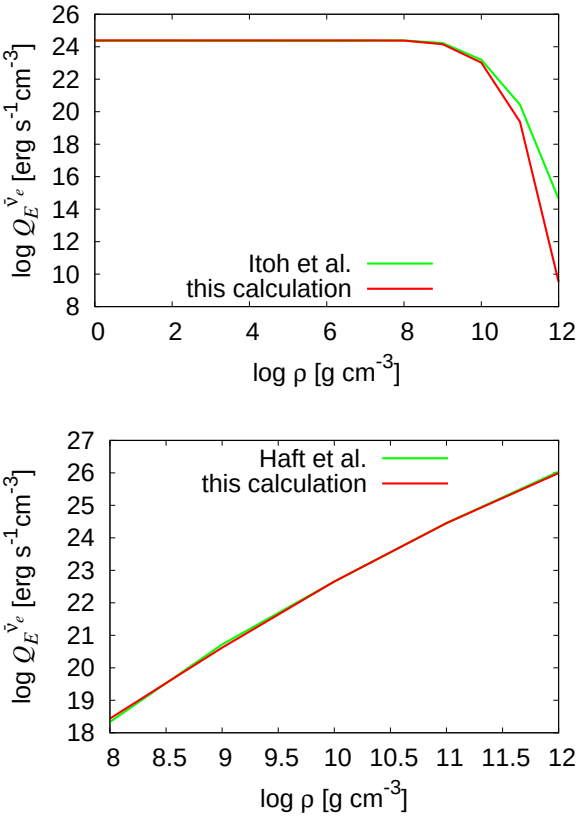

Figure 2.5: Comparisons with the fitting formulae for the pair annihilation (left panel) and plasmon decay (right panel). The temperature and electron fraction are fixed to 10^{10} K and $Y_e = 0.5$, respectively, in both panels.

2.3.3 Nuclear weak interactions

In this calculation I take into account the following reactions:

$$(Z, A) + e^- \longrightarrow (Z - 1, A) + \nu_e \ \text{(EC)} \tag{2.38}$$
$$(Z, A) \longrightarrow (Z - 1, A) + e^+ + \nu_e \ \left(\beta^+\text{decay}\right) \tag{2.39}$$
$$(Z, A) + e^+ \longrightarrow (Z + 1, A) + \bar{\nu}_e \ \text{(PC)} \tag{2.40}$$
$$(Z, A) \longrightarrow (Z + 1, A) + e^- + \bar{\nu}_e \ \left(\beta^-\text{decay}\right) \tag{2.41}$$

I consider in this calculation 17502 nuclei ($6 < Z < 160$, $2 < N < 320$) for EC and 3928 nuclei ($7 < Z < 117$, $9 < N < 200$) for β^- decay (See also Figure 2.6).

For the calculations of the luminosities and energy spectra of neutrinos I use FFN, ODA, LMP and LMSH tables whenever available. They normally give us the total reaction rates and average neutrino energies. If more than one tables are available for the same nucleus, I adopt one of them in the following order: LMSH > LMP > ODA > FFN. Note that the LMSH table includes data only on the ν_e emission via EC. If no information is available from these tables, which actually happens particularly when very heavy and/or neutron-rich nuclei (A, N) become populated at late times in the collapse phase, I employ the approximation formulae for $Q_{N,\mathrm{EC}}$ and $Q_{E,\mathrm{EC}}$ (Fuller et al., 1985; Langanke et al., 2003; Sullivan et al., 2016):

$$\begin{aligned} Q^{\nu_e}_{N,\mathrm{EC}} &= \sum_i \frac{X_i \rho}{m_p A_i} \frac{\ln 2 \cdot B}{K} \left(\frac{T}{m_e c^2}\right)^5 \\ &\quad \times \left[F_4(\eta) - 2\chi F_3(\eta) + \chi^2 F_2(\eta)\right], \end{aligned} \tag{2.42}$$

$$\begin{aligned} Q^{\nu_e}_{E,\mathrm{EC}} &= \sum_i \frac{X_i \rho}{m_p A_i} \frac{\ln 2 \cdot B}{K} \left(\frac{T}{m_e c^2}\right)^6 \\ &\quad \times \left[F_5(\eta) - 2\chi F_4(\eta) + \chi^2 F_3(\eta)\right], \end{aligned} \tag{2.43}$$

where $K = 6146$ s, $\chi = (Q - \Delta E)/T$, $\eta = (\mu_e + Q - \Delta E)/T$; X_i and A_i are the mass fraction and mass number of nuclear species i, respectively; the representative values of the matrix element and the energy level difference between the parent and daughter nuclei are set to $B = 4.6$ and $\Delta E = E_f - E_i = 2.5$ MeV, respectively, following Langanke et al. (2003). For β^- decay in the absence of data, I consult another table compiled by Tachibana (Tachibana and Yamada, 1995; Yoshida and Tachibana, 2000; Tachibana, 2000; Koura, 2004; Koura et al., 2003; Koura et al., 2005). Note that the data in this table were theoretically calculated for the terrestrial environment and hence do not take into account the Fermi-blocking of electrons in the final state. I hence re-incorporated them, albeit crudely, in the reaction rates as a suppression factor $1 - f_e(\langle E_e \rangle)$ based on the average electron energy $\langle E_e \rangle$, which is given in the Tachibana table. In Figure 2.6, I summarize which tables or the approximate formula is used in which region in the nuclear chart.

The energy spectrum is reconstructed for each reaction by using the effective q-value method (Langanke et al., 2001; Kunugise and Iwamoto, 2007; Patton et al.,

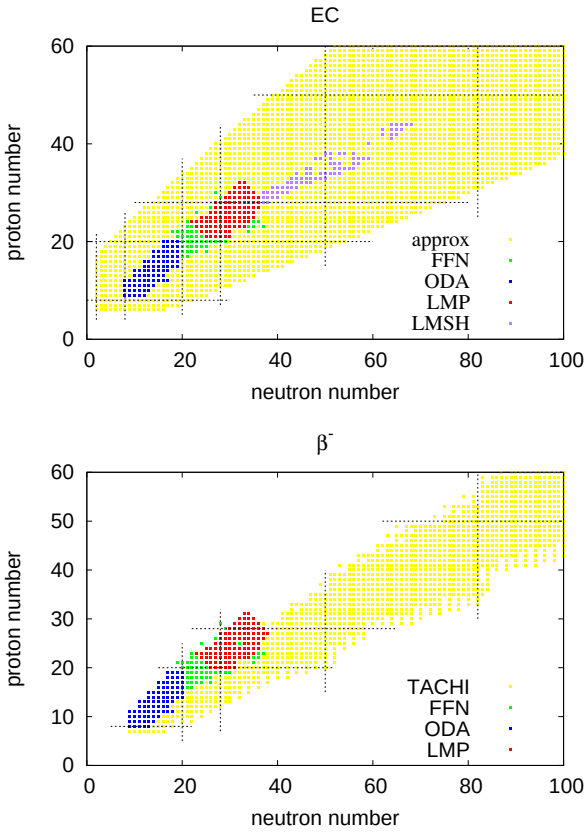

Figure 2.6: Nuclear charts indicating in different colors the nuclear species with the reaction rates for EC (left) and β^- decay (right) given in the LMSH (black, Langanke et al. (2003)), LMP (red, Langanke and Martínez-Pinedo (2001)), ODA (blue, Oda et al. (1994)), FFN (green, Fuller et al. (1985)), TACHI tables (yellow, Tachibana and Yamada (1995); Yoshida and Tachibana (2000); Tachibana (2000); Koura (2004); Koura et al. (2003); Koura et al. (2005)) as well as by the approximate formula (yellow, eq.(2.42)).

2017):

$$\begin{aligned}\frac{dQ^{\nu_j}_{N,k}}{dE_{\nu_j}} &= N_k \frac{{E_{\nu_j}}^2 \left(E_{\nu_j}-q\right)^2}{1+\exp\left(\frac{E_{\nu_j}-q-\mu_e}{T}\right)} \\ &\quad \times\Theta\left(E_{\nu_j}-q-m_e\right), \end{aligned} \tag{2.44}$$

for $k =$ EC, PC and

$$\begin{aligned}\frac{dQ^{\nu_j}_{N,k}}{dE_{\nu_j}} &= N_k \frac{{E_{\nu_j}}^2 \left(q-E_{\nu_j}\right)^2}{1+\exp\left(\frac{E_{\nu_j}-q+\mu_e}{T}\right)} \\ &\quad \times\Theta\left(q-m_e-E_{\nu_j}\right), \end{aligned} \tag{2.45}$$

for $k = \beta^-, \beta^+$, where $\nu_j = \nu_e$ or $\bar{\nu}_e$ and the normalization factor N_k is determined by the following relation:

$$Q_{N,k} = \int \frac{dQ^{\nu_j}_{N,k}}{dE_{\nu_j}} dE_{\nu_j}. \tag{2.46}$$

The effective q-value is actually given from the average energy $\langle E_{\nu_e}\rangle$ as follows:

$$\begin{aligned}\frac{Q^{\nu_e}_{E,\mathrm{EC}} + Q^{\nu_e}_{E,\beta^+}}{\lambda_{\mathrm{EC}}+\lambda_{\beta^+}} &= \langle E_{\nu_e}\rangle \\ &= \frac{\int E_{\nu_e} \frac{dQ^{\nu_e}_N}{dE_{\nu_e}}\left(E_{\nu_e}\right) dE_{\nu_e}}{\int \frac{dQ^{\nu_e}_N}{dE_{\nu_e}}\left(E_{\nu_e}\right) dE_{\nu_e}}, \end{aligned} \tag{2.47}$$

where the following notation is used:

$$\frac{dQ^{\nu_e}_N}{dE_{\nu_e}}\left(E_{\nu_e}\right) = \frac{dQ^{\nu_e}_{N,\mathrm{EC}}}{dE_{\nu_e}} + \frac{dQ^{\nu_e}_{N,\beta^+}}{dE_{\nu_e}}. \tag{2.48}$$

For $\bar{\nu}_e$, we replace the subscripts of EC and β^+ with PC and β^-.

2.3.4 Electron capture on free proton

The reaction rate is given by Bruenn (1985) as

$$\begin{aligned}\frac{dQ^{\nu_e}_{N,\mathrm{p}}}{dE_{\nu_e}} &= \frac{{G_F}^2}{\pi}\eta_{\mathrm{pn}}\left({g_V}^2+3{g_A}^2\right)\left(E_{\nu_e}+Q\right)^2 \\ &\quad \times\sqrt{1-\frac{m_e^2}{\left(E_{\nu_e}+Q\right)^2}}\, f_e\left(E_{\nu_e}+Q\right), \end{aligned} \tag{2.49}$$

where the mass difference between neutron and proton is given as $Q = m_n - m_p$, and the form factors for the vector and axial vector currents are given as $g_V = 1$ and $g_A = 1.23$, respectively; η_{pn} is defined as

$$\begin{aligned}\eta_{\mathrm{pn}} &\equiv \int \frac{2d^3p}{\left(2\pi\right)^3}\tilde{F}_p\left(\tilde{E}\right)\left[1-\tilde{F}_n\left(\tilde{E}\right)\right] \\ &= \frac{n_n - n_p}{\exp\left(\frac{\mu_n^0-\mu_p^0}{T}\right)-1}. \end{aligned} \tag{2.50}$$

In the above expression, the Fermi-Dirac distributions are denoted by $\tilde{F}_i(\tilde{E}) = 1/[1+\exp(\tilde{E}-\mu_i)/T]$ $(i=p,n)$, and the number densities and chemical potentials not including the rest-mass energies of proton and neutron are written as n_n, n_p and μ_p^0, μ_n^0, respectively; the non-relativistic expression $\tilde{E} \sim p_i^2/2m$ is employed for the kinetic energies of nucleons.

In my calculations, the PC and β^- decay on neutrons were ignored because they make very little contributions. This is simply because the free neutron is scarce. In addition, the β^- decay of free neutron is severely suppressed by the Fermi-blocking of electrons in the final state. Note also that the energy of neutrinos emitted by free neutrons are lower than those by nuclei.

2.3.5 Neutrino oscillations

The electron neutrinos and anti-neutrinos may convert to ν_x's and $\bar{\nu}_x$'s, respectively, and vice versa during propagation as a result of flavor oscillations. I take into account only the vacuum oscillations and MSW effect and ignore the collective oscillations, which will probably not occur in the pre-bounce phase. The so-called survival probabilities of ν_e and $\bar{\nu}_e$ denoted by p and p', respectively, are given in the adiabatic limit as

$$p = \begin{cases} \sin^2\theta_{13} = 0.0234 & \text{for NH,} \\ \sin^2\theta_{12}\cos^2\theta_{13} = 0.300 & \text{for IH,} \end{cases} \tag{2.51}$$

$$p' = \begin{cases} \cos^2\theta_{12}\cos^2\theta_{13} = 0.676 & \text{for NH,} \\ \sin^2\theta_{13} = 0.0234 & \text{for IH,} \end{cases} \tag{2.52}$$

with $\cos^2\theta_{12} = 0.692, \cos^2\theta_{13} = 0.977$ (Olive, 2014). The definition of the mixing angles is common and given in eq. (1.69).

Since stars are not homogeneous, I need to calculate the number and energy emissivities per volume and time, Q_N^ν and Q_E^ν, as well as the spectra, dQ_N^ν/dE_ν, as a function of radius and integrate them over the star to obtain the number and energy luminosities, L_N^ν and L_E^ν, together with the observed spectra, dL_N^ν/dE_ν for all flavors of neutrinos in the progenitor phase and for neutrinos other than ν_e in the collapse phase. I take the stellar radius as the upper limit of the integrals in principle although the integration started from the center is terminated at some radius when the value does not change appreciably any longer. For the nuclear weak processes, I take the upper limit as the radius of NSE region. I evaluate above quantities at different times so that their time evolutions could be obtained.

As for the pair processes in the collapse phase, I need actually to conduct two more integrals concerning the zenith and azimuth angles (see eq. (2.17)). In so doing, I distinguish the observer's frame from the local fluid-rest frame in the collapse phase (see eq. (2.18)). Then the differential and total number luminosities are given as

follows:

$$\begin{aligned}\frac{dL_N^{\bar{\nu}_e}}{dE_{\bar{\nu}_e}^{\rm lab}} &= \int \left.\frac{dQ_N^{\bar{\nu}_e}}{dE_{\bar{\nu}_e}^{\rm lab} d\cos\theta_{\bar{\nu}_e}^{\rm lab} d\phi_{\bar{\nu}_e}^{\rm lab}}\right|_{\theta_{\bar{\nu}_e}^{\rm lab}=\theta_s, \phi_{\bar{\nu}_e}^{\rm lab}=180^\circ} dV \\ &= \int \left.\frac{dQ_N^{\bar{\nu}_e}}{dE_{\bar{\nu}_e}^{\rm lab} d\cos\theta_{\bar{\nu}_e}^{\rm lab} d\phi_{\bar{\nu}_e}^{\rm lab}}\right|_{\theta_{\bar{\nu}_e}^{\rm lab}=\theta_s, \phi_{\bar{\nu}_e}^{\rm lab}=180^\circ} \\ &\qquad \times 2\pi r^2 dr d\cos\theta_s, \qquad (2.53) \\ L_N^{\bar{\nu}_e} &= \int \frac{dL_N^{\bar{\nu}_e}}{dE_{\bar{\nu}_e}^{\rm lab}} dE_{\bar{\nu}_e}^{\rm lab}. \qquad (2.54)\end{aligned}$$

In writing these expressions, I assume that the observer is located at infinity on the positive z-axis. Note that I employ these formulae only for the electron-positron annihilation, since it is dominant over the plasmon decay in the collapse phase. As for the latter, I give only a rough estimate, ignoring the frame difference and the Fermi-blocking in the final state.

The differential luminosities, or energy spectra, of ν_e and $\bar{\nu}_e$ with the vacuum and MSW neutrino oscillations being taken into account in the adiabatic limit are given as follows:

$$\left(\frac{dL_N^{\nu_e}}{dE_{\nu_e}}\right)_{\rm osc} = p\left(\frac{dL_N^{\nu_e}}{dE_{\nu_e}}\right)_0 + (1-p)\left(\frac{dL_N^{\nu_x}}{dE_{\nu_x}}\right)_0, \qquad (2.55)$$

$$\left(\frac{dL_N^{\bar{\nu}_e}}{dE_{\bar{\nu}_e}}\right)_{\rm osc} = p'\left(\frac{dL_N^{\bar{\nu}_e}}{dE_{\bar{\nu}_e}}\right)_0 + (1-p')\left(\frac{dL_N^{\bar{\nu}_x}}{dE_{\bar{\nu}_x}}\right)_0. \qquad (2.56)$$

In these expressions, the subscript 0 means the original spectra before the neutrino oscillations are considered; ν_x stands for ν_μ or ν_τ, both of which I assume are produced solely by electron-positron pair annihilations and have the same spectrum.

2.4 Results

In the following I present the main results: the number luminosities as well as the energy spectra for different neutrino flavors as functions of time. Based on them, I then estimate the expected numbers of detection events for different terrestrial neutrino detectors.

2.4.1 Luminosity and spectrum

In Figure 2.7, I show the time evolutions of the number luminosities of ν_e and $\bar{\nu}_e$ for the 15 $M_\odot$ progenitor model. The left and right panels display the progenitor and collapse phases, respectively. The origin of the time coordinate corresponds to the time, at which the hydrodynamical calculations are initiated. The solid and dashed lines denote $\bar{\nu}_e$ and ν_e, respectively. The colors of lines indicate the contributions from different processes as shown in the legend. Note that for ν_e in the collapse phase I show only the total luminosity, since it is all that the transport calculations produce. The nuclear weak processes are considered in the NSE regions alone and, as a result, they arise only after the temperature becomes $T \gtrsim 5 \times 10^9$ K. It is

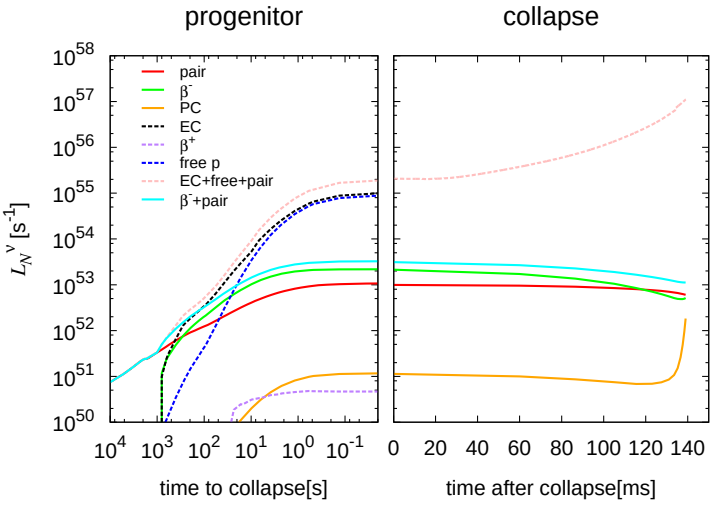

Figure 2.7: The time evolution of neutrino number luminosity for the 15 $M_{\odot}$ progenitor model. The origin of the horizontal axis corresponds to the time, at which the dynamical simulation is started. Dotted and solid lines show the results for the electron-type neutrino and anti-neutrino, respectively. Colors distinguish the different reactions. In the collapse phase, only total luminosity is shown for ν_e (pink dotted), since it is the quantity the dynamical simulation provides. Note that the same number of ν_e and $\bar{\nu}_e$ is produced from the electron-positron pair annihilations (red solid).

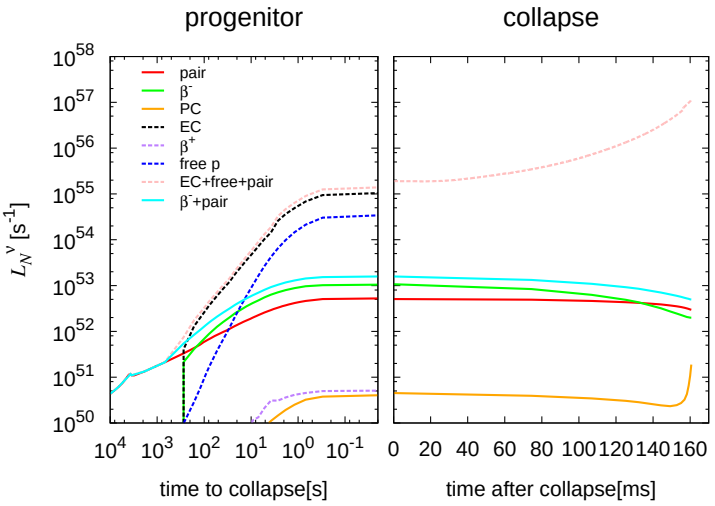

Figure 2.8: The same as Fig. 2.7 but for the 12 $M_{\odot}$ progenitor model.

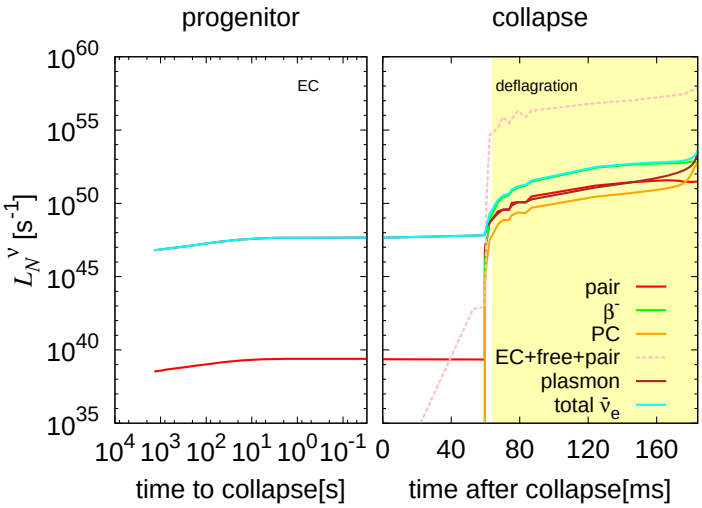

Figure 2.9: The same as Figs. 2.7 and 2.8 but for the 9 $M_\odot$ progenitor model. The region painted in yellow corresponds to the phase, in which the O+Ne deflagration takes place.

found that EC's on heavy nuclei and free protons are dominant in the emission of ν_e during the progenitor phase, while the emission of $\bar{\nu}_e$ occur mainly via the electron-positron pair annihilation until around a few hundreds of seconds before collapse and thereafter the β^- decay dominates, which is a new finding in this calculation. Although ν_e overwhelms $\bar{\nu}_e$ in the collapse phase as expected, this is also true in the progenitor phase. It is particularly the case at ∼100 seconds prior to collapse when the electron captures on free protons become appreciable.

Figure 2.8 is the same as Figure 2.7 but for the 12 $M_\odot$ progenitor model. The results are similar to those of the 15 $M_\odot$ model except that the numbers of emitted ν_e and $\bar{\nu}_e$ are slightly smaller for the 12 $M_\odot$ model than for the 15 $M_\odot$ model because the Fe-core of the 12 $M_\odot$ model has slightly high densities and low temperatures compared to the 15 $M_\odot$ model (see Figure 2.3).

Figure 2.9 shows, on the other hand, the temporal evolutions of the number luminosities in the 9 $M_\odot$ progenitor model, in which the ONe-core collapses to produce an ECSN. The strong degeneracy of electrons suppresses the electron-positron annihilation in this case and, as a result, the plasmon decay dominates initially until 60 ms after we switch to the hydrodynamical simulation when Ne and O are ignited at the center and the deflagration wave starts to propagate outward to produce NSE behind. The region painted in yellow corresponds to this O+Ne deflagration phase in the figure. Then, $\bar{\nu}_e$ emission by the β^- decay and ν_e emission via the EC's on heavy nuclei as well as on free protons overtake those through the plasmon decay.

In Figure 2.10 I present the radial profiles of the energy emissivities, Q_E^ν, from different processes for the 15 $M_\odot$ progenitor model at different times before collapse. The top panels display the results at a very early time in the progenitor phase ($\rho_c = 10^{9.1}$ g/cm^3), with both the radius (left) and mass coordinate (right) being employed as the horizontal axis. We define the Fe-core as the region, where the electron fraction satisfies $Y_e < 0.495$, and paint it in yellow. It is seen that all

emission processes occur rather uniformly in the region, $r \lesssim 2 \times 10^7$ cm, in this early phase. As the density increases with time, the $\bar{\nu}_e$ emission are all suppressed toward the center and the peaks in the emissivities appear off center and are shifted to the peripheral, $r \sim 5 \times 10^7$ cm, as shown in the bottom panels of the figure, which correspond to a later time ($\rho_c = 10^{10.3}$ g/cm^3). This is both due to the depletion of positrons in the initial state and to the Fermi-blocking of electrons in the final state as a consequence of the electron degeneracy. As for the ν_e emission, such a suppression does not occur and the emissivities are greatest in the central region.

Figure 2.11 exhibits the differential luminosities or the energy spectra normalized by the corresponding total luminosities. The colors and types of lines are the same as those in Fig. 2.7. One can see that $\bar{\nu}_e$'s emitted via PC on heavy nuclei (orange solid lines) have the highest average energies at all times. Recall, however, that the luminosity is very low for this process (see Figures 2.7-2.9). It should be also mentioned that the transport is not solved for $\bar{\nu}_e$, which will not be justified at high densities ($\rho_c \gtrsim 10^{11}$ g/cm^3) for these high-energy $\bar{\nu}_e$'s. Regardless, the dominant process in the $\bar{\nu}_e$ emission is either the electron-positron annihilation or the β^- decay and they both have average energies of 2-5 MeV at most, which may justify the neglect of transport. As for the ν_e emission, the EC's on heavy nuclei and free protons are mostly dominant and produce ν_e's with $\sim$10 MeV. In this case the transport in the core should be computed for the quantitative estimate of the luminosity and spectrum. A comparison between the results for the two types of progenitors indicates that neutrinos emitted from the ONe-core progenitor, especially those generated via the electron-positron annihilation, have higher energies than those from the Fe-core progenitors. This is because electrons are more strongly degenerate and have greater chemical potentials in the former.

In Table 2.2, I list the top five contributors to the EC and β^- decay, the dominant processes to produce ν_e and $\bar{\nu}_e$, respectively, at the time when $\rho_c = 10^{10.3}$ g/cm^3 in the 15 $M_\odot$ model. Note that the EC occurs mostly in the central region whereas the β^- decay happens off center mainly. I hence evaluate the EC rates at $r = 3.1 \times 10^5$ cm, where the density, temperature and electron fraction are $\rho = 10^{10.3}$ g/cm^3, $T = 0.861$ MeV, $Y_e = 0.417$ and $\mu_e = 11.9$ MeV. The β^- decay rates are presented, on the other hand, for the condition at $r = 2.7 \times 10^7$ cm, i.e., $\rho = 10^{9.79}$ g/cm^3, $T = 0.856$ MeV, $Y_e = 0.423$ and $\mu_e = 7.87$ MeV. I find that although the emissivities for individual nuclei are proportional to the product of their mass fraction and the reaction rate, the former is more important, since the latter changes by a factor whereas the former varies by an order. It is noteworthy in this respect that the top two contributors to the EC and the top one to the β^- decay are those nuclei with magic proton numbers, which is the reason why they are more abundant than others. Note again that their reaction rates are not the greatest.

In Figure 2.12, I show the energy spectra of neutrinos emitted from these nuclei. It is recognized that the spectra for the β^- decay presented in the lower panel are not much different among the nuclei. It is also evident that the average energies are lower than those for the ν_e's emitted through the EC's as exhibited in the upper panel. This is because the latter includes the contribution from the kinetic energy of degenerate electrons. The variation among the nuclei is also larger for the EC.

Once the NSE is established after the passage of the deflagration wave in the 9

$M_\odot$ model, the composition is simply determined by the density, temperature and electron fraction. The iron-group elements hence become dominant for EC and β^- decay also in the $9M_\odot$ model just as in the 12 and $15M_\odot$ models.

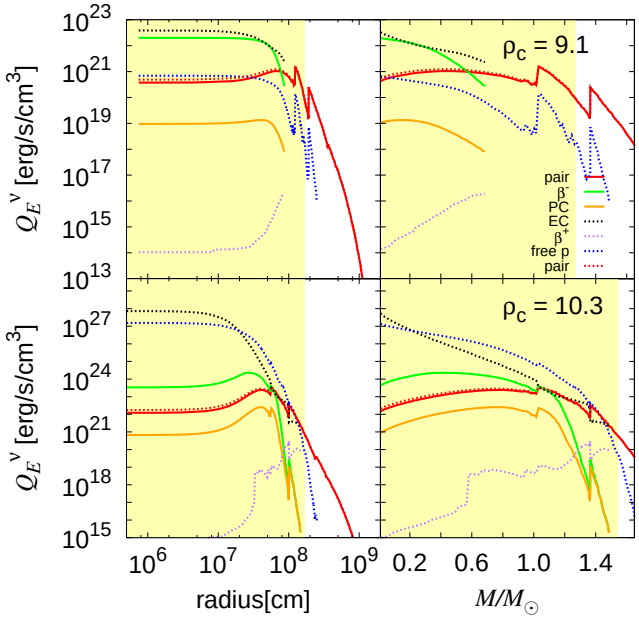

Figure 2.10: The radial profiles of the energy emissivities from different processes for the 15 $M_\odot$ progenitor model. Top and bottom panels show the results when the central density is $\rho_c = 10^{9.1}$ and $10^{10.3}$ g/cm^3, respectively. In the left panels the radius is used as the horizontal axis whereas in the right panels the mass coordinate is employed. The line types and color coding are the same as in Figure 2.7. We define the Fe-cores as the regions, where the electron fraction satisfies $Y_e < 0.495$, and they are painted in yellow in this figure.

2.4.2 Event numbers at detectors

Based on the results obtained so far, I estimate the numbers of detection events for some representative detectors, which include those under planning at present. For the detection of $\bar{\nu}_e$, almost all detectors utilize the inverse β decay. I express the cross section $\sigma(E_\nu)$ of this interaction as eq. (1.74).

Electron neutrinos are normally detected via the electron-scattering: $\nu_e + e^- \longrightarrow \nu_e + e^-$, in the currently available detectors. Its reaction rate is much lower than that of the inverse β decay, however, and the detection of ν_e's in the pre-bounce phase has been thought to be almost impossible. Then the new-type detector using liquid Argon has come into view. The planned deep underground neutrino observatory, or DUNE, is one of the such detectors (Acciarri et al., 2016). It employs the absorption of ν_e by ^{40}Ar and its cross section of this reaction is obtained numerically with SNOwGLOBES(ver1.1).

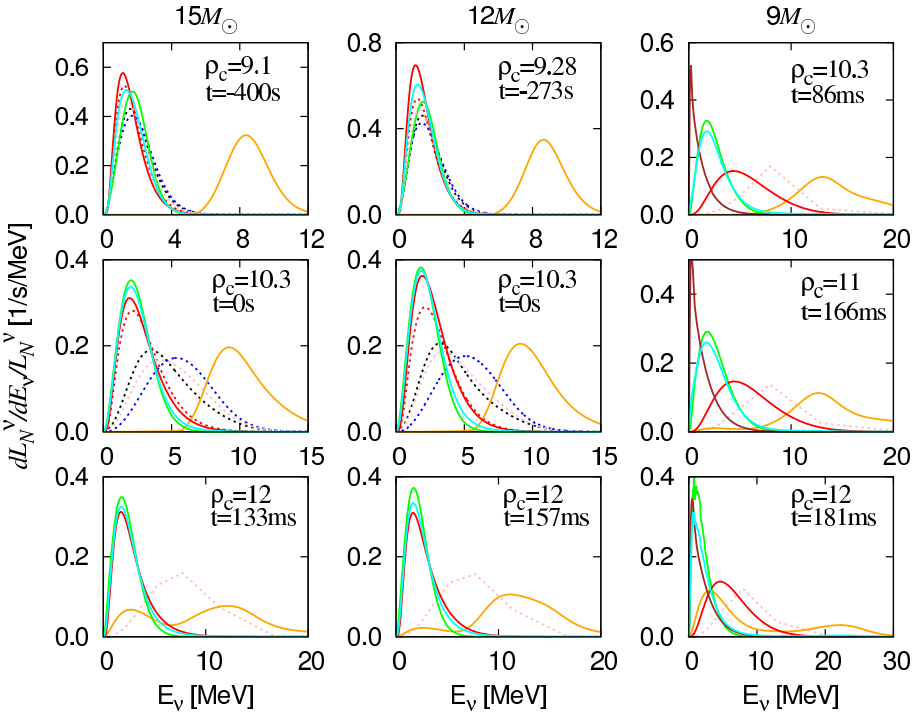

Figure 2.11: The spectra of neutrinos emitted from the entire star at indicated times for the three progenitor models. They are normalized by the corresponding number luminosities. Colors indicate different emission processes as in Figure 2.7. Note that the scale of the horizontal axes are different among the three models.

Table 2.2: Weak reaction rates and mass fractions of the top five nuclei contributing to the total number luminosities from EC and β decay in the 15 $M_\odot$ progenitor model at the time when the central density is $\rho_c = 10^{10.3}$ g/cm^3. This density corresponds to the time, at which we switch to the dynamical calculation ($t = 0$). The EC rates are evaluated at $r = 3.1 \times 10^5$ cm, where the density, temperature and electron fraction are $\rho = 10^{10.3}$ g/cm^3, $T = 0.861$ MeV, $Y_e = 0.417$, $\mu_e = 11.9$ MeV. The rates of β^- decays are calculated at $r = 2.7 \times 10^7$ cm, where they are largest and $\rho = 10^{9.79}$ g/cm^3, $T = 0.856$ MeV, $Y_e = 0.423$, $\mu_e = 7.87$ MeV.

EC				β^-			
	(N, Z)	X_i	R_i		(N, Z)	X_i	R_i
^{66}Ni	(38,28)	7.76×10^{-2}	10.57	^{49}Ca	(29,20)	1.88×10^{-2}	3.64×10^{-2}
^{64}Ni	(36,28)	1.99×10^{-2}	11.89	^{53}Ti	(31,22)	1.29×10^{-2}	5.56×10^{-2}
^{76}Ge	(44,32)	5.88×10^{-3}	32.59	^{65}Co	(38,27)	4.60×10^{-3}	1.78×10^{-1}
^{87}Kr	(51,36)	7.85×10^{-3}	26.37	^{59}Mn	(34,25)	9.78×10^{-3}	5.20×10^{-2}
^{70}Zn	(40,30)	5.32×10^{-3}	30.04	^{55}V	(32,23)	6.05×10^{-3}	7.62×10^{-2}

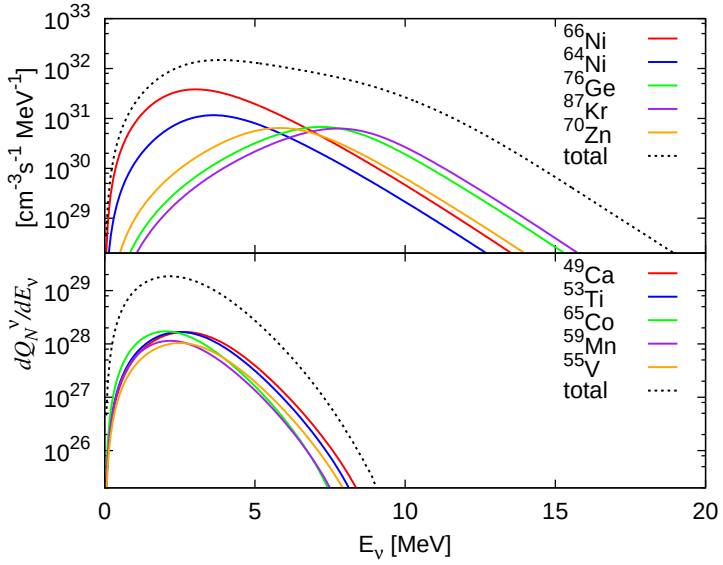

Figure 2.12: The energy spectra for the EC and β^- decay by the dominant heavy nuclei given in Table 2.2 at the time when the central density becomes $\rho_c = 10^{10.3}$ g/cm^3. The top panel shows the ν_e spectrum for EC, while the bottom panel displays the $\bar{\nu}_e$ spectrum for β^- decay.

Then the event rate, r, at a detector is expressed as

$$r = \frac{N}{4\pi D^2} \int_{E_{\rm th}}^{\infty} dE_{\nu_1} \sigma\left(E_{\nu_1}\right) \frac{dL_N^{\nu_1}}{dE_{\nu_1}}, \tag{2.57}$$

in which N and D denote the target number in the detector and the distance to the star from the detector, respectively. For simplicity, we assume that the detection efficiency is 100 % above the threshold energy $E_{\rm th}$. The features of relevance for the detectors that we consider in this calculation, i.e, Super-Kamiokande, KamLAND, Hyper-Kamiokande, JUNO and DUNE, are summarized in Table 2.3. The cumulative number of events, $N_{\rm cum}$, is obtained by integrating the rate up to the given time:

$$N_{\rm cum}(t) = \int_{t_{\rm ini}}^{t} r\, dt. \tag{2.58}$$

In order to give quantitative estimates to the numbers of detection events, I need to take into account neutrino oscillations appropriately. For that purpose, not only the luminosities of ν_e's and $\bar{\nu}_e$'s but also those of ν_μ's and ν_τ's are required. In this calculation I have calculated them for the electron-positron annihilation on the same basis as ν_e and $\bar{\nu}_e$. I give the results in Fig. 2.13, in which the time evolution of the number luminosities as well as the energy spectra at three different epochs are displayed in the upper and lower panels, respectively. It is observed that the luminosities are much smaller than those of ν_e as expected and are somewhat lower even compared with $\bar{\nu}_e$. This is simply because that ν_μ's and ν_τ's lack charged-current reactions and are produced solely from the electron-positron annihilation.

Table 2.3: The detector parameters assumed in this calculation. The numbers given here are not very precise and just meant for a rough estimate. JUNO is assumed to be a scale-up of KamLAND by a factor of 20. We also assume that the energy threshold of Hyper-Kamiokande will be somewhat higher than that of Super-Kamiokande. I use the total volume for the 2 tank-design of Hyper-Kamiokande. The energy threshold of DUNE is still uncertain and we employ both an optimistic (5 MeV) and more realistic (10.8 MeV) values in this study. (Smy et al., 2004; Berger et al., 2009; Abe et al., 2018; An et al., 2016; Acciarri et al., 2016)

Detector	Mass [kt]	Target number N	Energy threshold [MeV]
Super-K	32	2.14×10^{33}	5.3
KamLAND	1	8.47×10^{31}	1.8
Hyper-K	516	3.45×10^{34}	8.3
JUNO	20	1.69×10^{33}	1.8
DUNE	40	6.02×10^{32}	5.0, 10.8

The average energies are $\lesssim$ 2 MeV, much lower than that of ν_e and, as a result, the opacities for these heavy-lepton neutrinos are smaller, justifying the neglect of transport in their calculations.

Figures 2.14, 2.15 and 2.16 present the time evolutions of event rates (top) and cumulative numbers of detection events (bottom) for different detectors in the progenitor (left) and collapse (right) phases for the three progenitors. For the 9 $M_\odot$ model, only the collapse phase is shown, since the progenitor phase will not be observed even at the distance as close as 200 pc. The normal (inverted) hierarchy is assumed in the upper (lower) half of the top panels in each figure. All the detectors except DUNE, which will detect ν_e's, will observe $\bar{\nu}_e$'s mainly. From the comparison of the left and right panels I find that the progenitor phase is dominant over the collapse phase for $\bar{\nu}_e$ with the latter contributing only a few percent. This is due to the electron degeneracy, which suppresses both the β^- decay via the Fermi-blocking of the electron in the final state and the electron-positron annihilation through the depletion of the positron in the initial state.

In the case of ν_e, the collapse phase is much more important although it lasts for much shorter periods. This is because both the luminosity and the average energy rise with the density. The detections of $\bar{\nu}_e$'s in the pre-bounce phase are hence more suitable for the alert of the imminent supernova (Asakura et al., 2016; Yoshida et al., 2016). In fact, we may be able to issue an alert a few days before the core collapse for the Fe-core progenitors if neutrinos obey the normal mass hierarchy. The ν_e emission from the ONe-core progenitor, on the other hand, are much shorter than those from the Fe-core progenitors presented in Figure 2.16. They become appreciable only after NSE is established in the collapsing core by the passage of the deflagration wave. DUNE will detect ν_e's only from less than 100 ms prior to bounce, and may be hence possible to distinguish the two types of progenitors by the time of the first detection of ν_e's.

Depending on the mass hierarchy, the neutrino oscillations affect either ν_e or $\bar{\nu}_e$

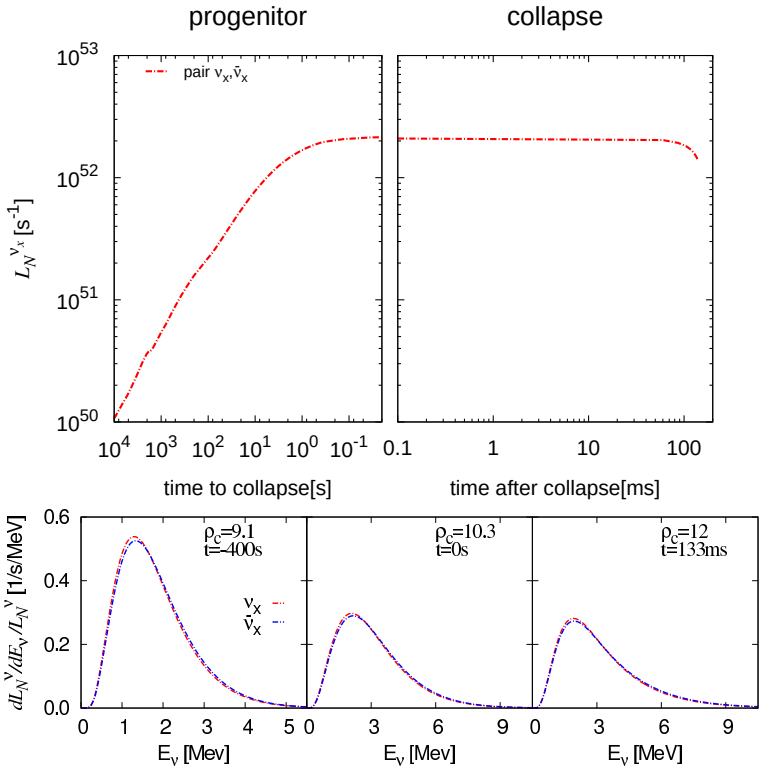

Figure 2.13: The number luminosity (top) and normalized spectra (bottom) of ν_x and $\bar{\nu}_x$ emitted via the electron-positron annihilation. Note that the number luminosities of ν_x and $\bar{\nu}_x$ are identical to each other.

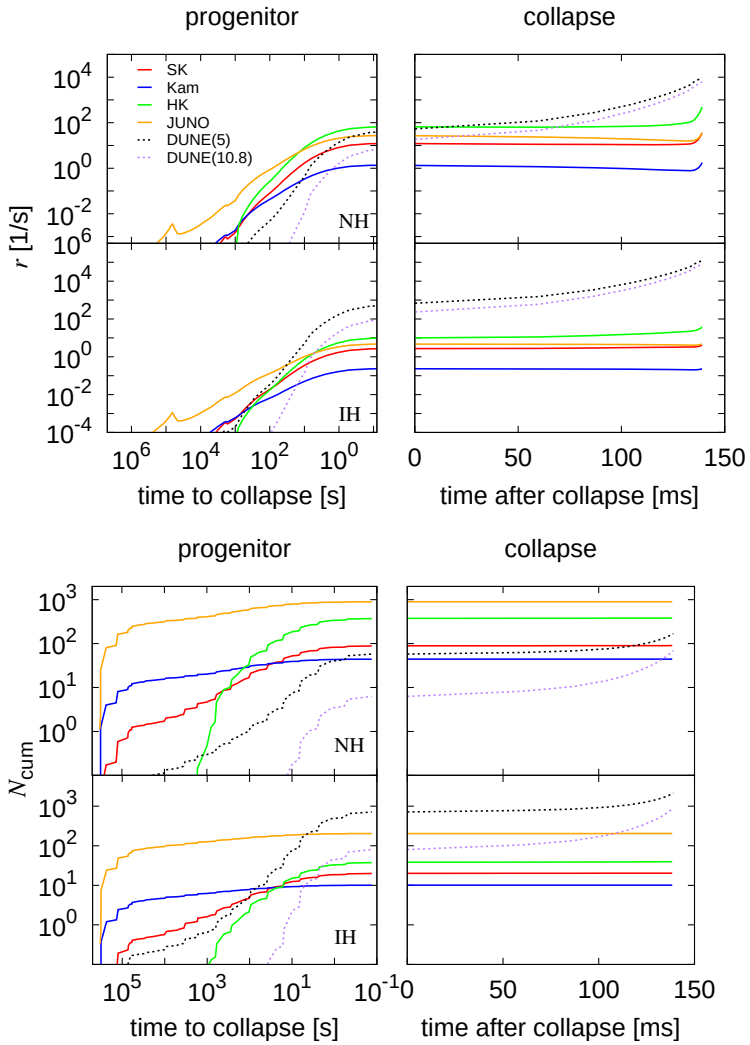

Figure 2.14: The time evolutions of event rates (top panels) and the cumulative numbers of events (bottom panels) for the 15 $M_\odot$ progenitor model. The upper half of each panel shows the results for the normal mass hierarchy, while the lower half presents those for the inverted mass hierarchy. Colors specify neutrino detectors. We consider ν_e for DUNE (dotted line) and $\bar{\nu}_e$ for other detectors (solid lines).

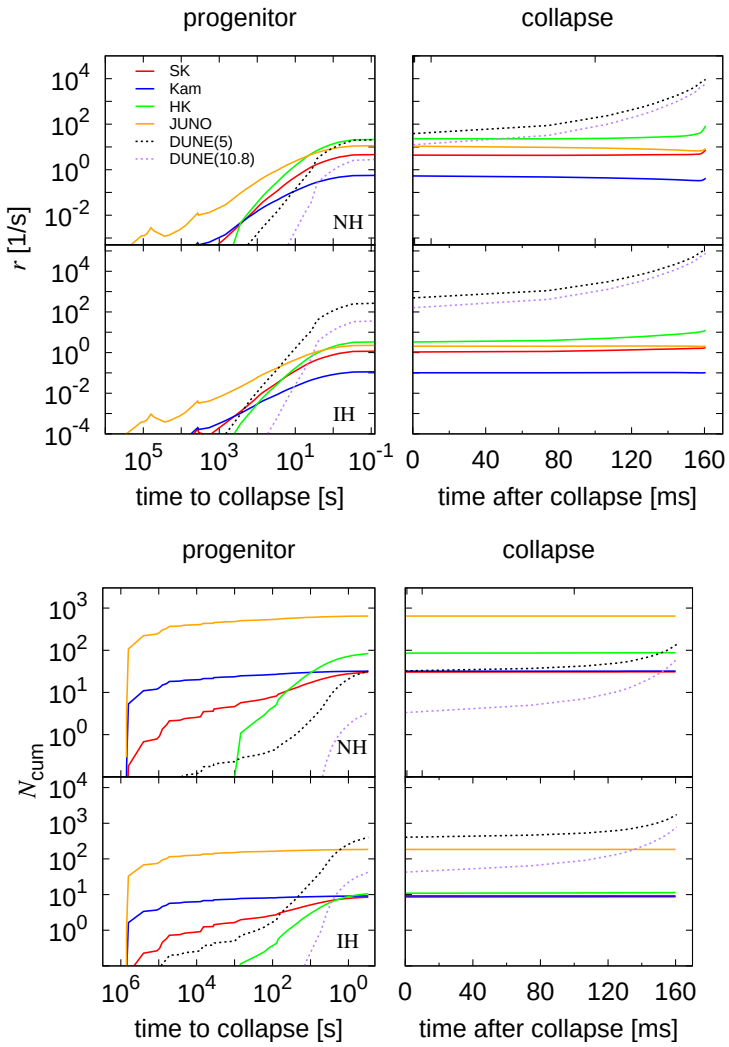

Figure 2.15: The same as Figure 2.14 but for the 12 $M_\odot$ progenitor.

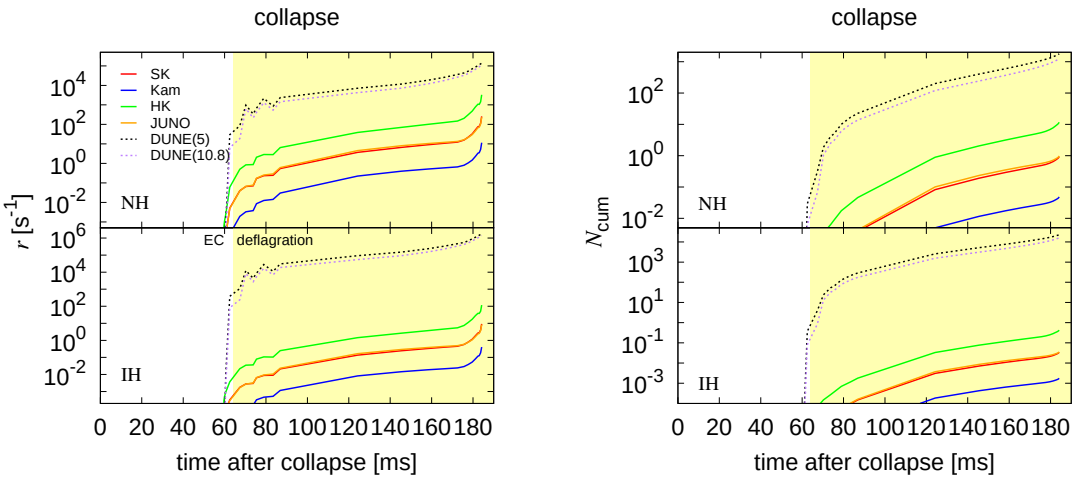

Figure 2.16: The same as Figures 2.14 and 2.15 but for the 9 $M_\odot$ progenitor. Only the collapse phase is shown.

predominantly. In fact, in the normal hierarchy, the spectrum of ν_e is exchanged with that of ν_τ in the adiabatic MSW oscillation and is further mixed among three flavors in the vacuum oscillations whereas the spectrum of $\bar{\nu}_e$ is mixed with those of $\bar{\nu}_\mu$ and $\bar{\nu}_\tau$ only in the vacuum oscillations. The situation is the other way around in the case of the inverted hierarchy, in which the MSW affects $\bar{\nu}_e$ also. It is recalled that the luminosities of ν_x and $\bar{\nu}_x$ are lower than those of ν_e and $\bar{\nu}_e$.

As a consequence, the chance to observe $\bar{\nu}_e$'s is higher for the normal hierarchy and JUNO will see more than 850 of them in the progenitor phase from as early as a few days prior to collapse, which is roughly the end of O burning, if the 15 $M_\odot$ progenitor is located at 200 pc from the earth. The event number will be reduced by a factor of $\sim$4 in the case of the inverted hierarchy. The detection of ν_e's on DUNE will be more plausible for the inverted hierarchy and, in fact, the expected event number may exceed 2000 if the distance to the source is again 200 pc, i.e., the distance to Betelgeuse and the energy threshold is optimistically assumed to be 5 MeV. The first ν_e may be observed several tens of minutes before collapse, which corresponds to the end of Si-burning. In the normal hierarchy, on the hand, the number of detections will be reduced by more than a factor of 10. Such a large difference in the number of detections suggests a possibility to judge the neutrino mass hierarchy. It is interesting to point out that as far as the ν_e is concerned, the ONe-core progenitor may offer a better chance of detection at DUNE. This is because the temperature in the NSE region behind the O+Ne deflagration is higher than in the Fe-core. As long as the Fe-core progenitors are concerned, the more massive it is, the larger number of detection events are expected both for ν_e and $\bar{\nu}_e$.

Table 2.4: The expected numbers of detection events for different detectors. The numbers are pertinent to ν_e for DUNE and to $\bar{\nu}_e$ for other detectors. In the case of the Fe-core progenitors, the individual contributions from the progenitor and collapse phases are also shown in the parentheses in this order. The source is assumed to be located at 200 pc from the earth. Both the normal and inverted mass hierarchies are considered in the adiabatic oscillation limit.

detector	9 $M_\odot$		12 $M_\odot$		15 $M_\odot$	
	normal	inverted	normal	inverted	normal	inverted
Super-K	0.93	0.03	30.8	8.68	89.9	20.3
			(30.1+0.71)	(8.48+0.20)	(88.3+1.61)	(19.9+0.41)
KamLAND	0.05	0.002	32.0	9.15	44.3	10.1
			(31.9+0.07)	(9.13+0.02)	(44.2+0.15)	(10.1+0.03)
Hyper-K	11.6	0.42	83.9	10.9	363	37.7
			(80.0+3.85)	(10.1+0.76)	(353+9.84)	(35.9+1.82)
JUNO	0.98	0.04	645	184	894	204
			(644+1.47)	(184+0.33)	(891+3.07)	(203+0.63)
DUNE	1765	22685	137	1756	169	2142
(5MeV)			(32.4+105)	(406+1350)	(57.8+111)	(713+1429)
DUNE	1238	15910	61.3	789	69.3	895
(10.8MeV)			(3.33+58.0)	(42.7+746)	(6.27+63)	(80.1+815)

In Table 2.4.2, I summarize the expected numbers of events at Super-Kamiokande, KamLAND, Hyper-Kamiokande, JUNO and DUNE, assuming that progenitors are

200 pc away from us. They are the numbers of ν_e events for DUNE and those of $\bar{\nu}_e$ events for other detectors. In the table, the contributions from both the progenitor and collapse phases are exhibited. It is found that $\bar{\nu}_e$'s from the 12 and 15 $M_\odot$ progenitors can be detected at all detectors if the source is this close. In particular, the planned detectors such as Hyper-Kamiokande and JUNO look promising if one considers the number of events alone: they will detect a few tens of $\bar{\nu}_e$'s even if they are emitted from 1kpc away. The detection of $\bar{\nu}_e$'s from the ONe-core progenitor seems to be nearly impossible even with the planned detectors. I will be hence able to distinguish the two types of progenitors, i.e., ONe-core progenitors and Fe-core progenitors, by detection or non-detection of $\bar{\nu}_e$. It is stressed, however, that in this calculation I have incorporated nuclear processes, such as β^- decay, which are demonstrated to be dominant in the production of $\bar{\nu}_e$. I show the expected numbers of ν_e events for the values of two energy thresholds, 5 and 10.8 MeV, considering its uncertainties at present. The former is somewhat optimistic and the latter may be more realistic. The first detection of ν_e will be delayed for the latter case to a few tens of seconds before core bounce. Note, however, that the energy of ν_e's in the collapse phase is high ($\sim$8 MeV) and we will be still able to detect a large number of ν_e's. In this calculation, I do not treat the neutrino emission at $\rho > 10^{13}$ g/cm^3 because the compositions and weak reaction rates of heavy nuclei are highly uncertain there. The number of events for $\bar{\nu}_e$ will not increase much by the time of core bounce, however. In fact, it is expected to increase by $\sim$200 for ν_e if one simply extrapolates the results obtained for $\rho_c < 10^{13}$ g/cm^3 up to core bounce in the inverted hierarchy. This issue will be addressed in a future publication.

2.5 Summary and discussion

I calculated $\bar{\nu}_e$ emission via thermal processes and nuclear weak processes from both the Fe-core progenitors and the ONe-core progenitor in the quasi-static evolutionary phase and the collapse phase. It should be stressed here that no quantitative estimate has been done so far on the neutrino emission during the collapse phase mainly because neutrinos are emitted more intensively in the post-bounce phase and the proto-neutron star cooling phase that follows. This calculation is hence the first to demonstrate that the collapsing phase has a potential to provide new insights.

I have investigated the emission of all-types of neutrinos from the progenitor phase up to the pre-bounce time, at which the central density reaches $\rho_c = 10^{13}$ g/cm^3. I have compared the two types of progenitors of CCSNe: one that produces the Fe-core and the other that yields the ONe-core before core collapse, to see whether I can get some information on the cores deep inside massive stars, which would be inaccessible to other means, by observing the neutrinos they emit. I have first re-calculated the neutrino emission from the realistic progenitor models with 9, 12 and 15 $M_\odot$ on the zero age main sequence with both the thermal and nuclear weak processes being taken into account. Note again that the 9 $M_\odot$ model is a progenitor with the ONe-core that collapses to produce the ECSN and the other two are supposed to be progenitors of the FeCCSNe.

I have then switched to hydrodynamical simulations of core collapse up to the pre-bounce time, at which the central density reaches $\rho_c = 10^{13}$ g/cm^3, with the

transfer of ν_e in the core being treated appropriately. Since other types of neutrinos are much less abundant and have lower energies typically, I have treated them in the post-process, in which I have extracted the time evolutions of density, temperature, Y_e and f_{ν_e}, the distribution function of ν_e, from results of the simulations and calculated the emissivities of these neutrinos with possible minor back-reactions to dynamics being ignored. Finally, based on the luminosities and spectra of neutrinos thus obtained, I have estimated the expected numbers of detection events on some representative neutrino detectors. In so doing I have taken into proper account the vacuum and MSW oscillations of neutrino flavors.

I have found that the β^- decay and the EC on heavy nuclei and free protons dominate the number luminosities of $\bar{\nu}_e$ and ν_e, respectively, from several tens of minutes before core bounce. To these reactions heavy nuclei not with large reaction rates but with large mass fractions contribute most. Because of the Fermi-blocking of electrons in the final state, the β^- decay is suppressed at high densities, where electrons are strongly degenerate, and the number luminosity of $\bar{\nu}_e$ is decreased toward core bounce. As a consequence, the progenitor phase is dominant over the collapse phase in the $\bar{\nu}_e$ emission. In contrast, the ν_e emission occurs predominantly in the collapse phase although it is much shorter than the progenitor phase that precedes it. The detection of $\bar{\nu}_e$'s in the pre-SN phase is hence more suitable for the alert of the imminent supernova, which may be indeed possible a few days before core bounce for the Fe-core progenitors if neutrinos obey the normal mass hierarchy.

The electron-type antineutrinos from the 12 and 15 $M_\odot$ progenitors can be detected by all detectors, especially on the planned detectors such as Hyper-Kamiokande and JUNO if the distance to them is $\lesssim 1$ kpc. The 9 $M_\odot$ progenitor will be quite difficult to observe with $\bar{\nu}_e$'s even if it is as close to us as 200 pc, the distance to Betelgeuse. I may hence conclude that I can distinguish the two types of progenitors by detection or non-detection of $\bar{\nu}_e$ prior to collapse. With DUNE, on the other hand, we will be able to detect more than a thousand of ν_e's from all the progenitor models if the distance to the source is again 200 pc and neutrinos have the inverted mass hierarchy. The event numbers are reduced by a factor of $\sim$10 if they obey the normal mass hierarchy. Such a large difference in the number of detections suggests a possibility to judge the neutrino mass hierarchy. It is interesting to see that the ONe-core progenitor offers the best chance in this case. This implies that irrespective of the type and mass of progenitor we may be able to confirm our current understanding of the physics in the collapse phase. Note, however, that ν_e's are not useless in distinguishing the progenitor types. Although it will not be easy observationally, the fact that the ν_e emission from the ONe-core progenitor in the pre-bounce phase occurs in much shorter periods than those from the Fe-core progenitors may be utilized to discriminate the former from the latter.

My estimates admittedly include several uncertainties. In the following we comment on them in turn. In this calculation, I began the hydrodynamical simulations of the collapse phase when the central density becomes $\rho_c = 10^{10.3}$ g/cm^3 for the Fe-core progenitors, which is rather arbitrary. In fact, the cores are already unstable at this point and have started to collapse in the quasi-static evolutionary calculations, which means that we could have switched to the dynamical simulations a bit earlier. Indeed, if I switch at $\rho_c = 10^{10}$ g/cm^3, the time it takes to reach core bounce

is shortened by more than a second. This is due to artificially accelerated collapse in the new calculation, which is in turn caused mainly by differences between the EOS used in the stellar-evolution calculation and that employed in the dynamical simulation. The EC rates are also different. Although the discrepancy of more than a second in the time up to core bounce may seem not small, the difference in the event numbers may not be so large, since most of the deviation occurs immediately after the onset of the simulation, when the density is still not very high.

The uncertainty in the EOS also affects the EC rates through the mass fractions of heavy nuclei in the NSE composition. Buyukcizmeci et al. (2013) compared the nuclear composition of three multi-species EOS's including ours that are recently constructed for supernova simulations. According to their results, differences in the mass fractions of heavy nuclei increase with temperature and/or density and become as large as a factor of two at $T = 2$ MeV and $\rho = 10^{11}$ g/cm^3. The different treatments of the surface, bulk and shell energies of heavy nuclei are the main cause for the discrepancies. In fact, the temperature dependence of the shell energies that is incorporated in Furusawa et al. (2017b) tends to smooth out the mass distribution around closed shell nuclei and may reduce the EC rate at early times in the collapse phase by $\sim$20% (Furusawa et al., 2017a). The shell quenching considered in Raduta et al. (2017) may also affect the nuclear weak rates during the collapse phase.

As explained in Section 2.3.3, I have employed the nuclear weak interaction rates obtained by detailed calculations for individual heavy nuclei whenever they are available. As the density and temperature increase in the collapse phase, however, there appear heavy nuclei that are not included in these tables. I am then forced to use for these nuclei the approximate formula, eq.(2.42), for EC and another table (Tachibana and Yamada, 1995) for β^- decay. Since the approximate formula is based on the data of nuclei around β stable line, it may not be applicable to neutron-rich nuclei. The rates in Tachibana's table, on the other hand, are not meant for supernova simulations originally and calculated for isolated nuclei under the terrestrial condition. I have hence included the Fermi-blocking of electrons in the final state very crudely. Moreover, the data in this table do not include the contribution from excited states. When the central density exceeds $\rho_c \sim 10^{11.4}$ g/cm^3, most of $\bar{\nu}_e$'s come from the β^- decays of nuclei, the rates of which are derived from this table. I certainly need to improve them in the future. In this calculation, I have not treated the neutrino emission at $\rho \gtrsim 10^{13}$ g/cm^3 on purpose because nuclei become more and more exotic with their mass and atomic numbers getting larger to produce so-called nuclear pastas before uniform nuclear matter is realized. The compositions and weak reaction rates of these nuclei are highly uncertain at such high densities. Moreover, the dynamical simulations handle them in a very crude way, ignoring a possible variety of pasta configurations and interpolating the reaction rates between a certain sub-nuclear density and the nuclear saturation density. As mentioned earlier, one can crudely estimate the number of detections of ν_e during the period from the time, at which $\rho_c = 10^{13}$ g/cm^3, until core bounce by simply extrapolating the event rates obtained in Figures 2.14-2.16. I have found then that $\sim$200 more ν_e's may be observed by DUNE for the inverted hierarchy. I certainly need improvements in the treatment of this phase, which will be a future work.

Although it is much beyond the scope of this calculation to take into account in

detail the background noise for each detector and discuss the detection possibility quantitatively, I touch the issue briefly, since the actual detectability depends on it crucially. If I adopt several hundreds of events/day as the typical noise level of Super-Kamiokande at present, $\bar{\nu}_e$'s may not be detected even from FeCCSNe located at 200 pc. However, the background will be reduced remarkably to 0.21 events per hour after Gadolinium is doped as designed (Beacom and Vagins, 2004). An accompanied reduction of the energy threshold may increase the number of events by a factor of $\gtrsim 10$ as demonstrated by Yoshida et al. (2016). The background for KamLAND is already very low $\sim$1 event/day and will not be a problem. In the case of Hyper-Kamiokande, on the other hand, the reduction of the energy threshold, if possible, will have a big impact on the event number as mentioned earlier.

In this calculation, I have considered only two relatively light Fe-core progenitors. It is certainly important, though, to study other more massive progenitors systematically. It should be also emphasized that the expected event numbers for the present models may change by a factor of a few if one considers various uncertainties in the current stellar-evolution calculation. As stated at the beginning, my ultimate goal is to extend the current investigation until the end of the cooling phase of proto neutron stars seamlessly and consistently. It is stressed again that most of the studies on the neutrino emission from CCSNe and their detections at terrestrial detectors done so far have treated the post-core bounce phase and the subsequent phase of the proto neutron star cooling separately and very little attention has been paid to the phase preceding them. Now that we have a lot of CCSN simulations that are successful to obtain explosions, I believe that we should make a serious effort to draw light curves and spectral evolutions of neutrinos that span the entire period from the progenitor phase up to the formation of the normal neutron star. These calculations are just the first step.

Chapter 3

Supernova neutrinos

3.1 Purpose

In the neutrino heating mechanism, which is the most promising scenario in the revival of the stalled shock, neutrinos have different roles depending on flavors. The shock wave is heated by charged current reactions of ν_e's and $\bar{\nu}_e$'s and their spectra at the shock wave are critical for the shock revival. On the other hand, ν_x's are emitted from the PNS with the largest average energy and contribute to the cooling of the PNS, which decides the temperature inside the PNS and affects the neutrino luminosities from the PNS surface. Moreover, ν_x's may convert to ν_e's or $\bar{\nu}_e$'s via the neutrino oscillations near the PNS surface, and the neutrino luminosities and spectra are changed during propagation. Due to the development of detectors, their observations at the future galactic SNe will give us various information about the SN explosions such as their mechanism, EOS at the high density and temperature, the formation scenarios of compact objects, neutrino physics and so on. The precise theoretical predictions of SN neutrinos are absolutely required. It is, therefore, necessary to deal with the neutrino emission inside the PNS and scattering processes with matters during propagation from the PNS surface to the shock wave in detail.

I focus on the energy exchange by neutrino-nucleon scatterings, or nucleon recoils, for the first step. In the recent numerical studies, the number of energy and angle bins are not enough to resolve the small energy exchange. The number of scatterings is, however, large because of numerous nucleons inside stars, and it is necessary to investigate how much neutrino spectra are changed by nucleon recoils. Actually, Raffelt (2001) and Keil et al. (2003) claim the importance of nucleon recoils for heavy-lepton neutrinos, especially. In this study, I hence carry out steady-state calculations of the neutrino transport from the PNS surface to the region, where neutrino reactions can be neglected, based on the hydrodynamic backgrounds derived from the dynamical SN simulations. Then I estimate the change of neutrino spectra by nucleon recoils and discuss which reaction dominates in the thermalization of neutrino spectra.

3.2 Numerical methods of Monte Carlo simulation

3.2.1 Monte Carlo methods

There are two approaches to solve the radiation transport equations: discretized method and Monte Carlo method. In discretized methods, for example S_N method (Castor, 2004), we discretize the transport equations on a phase space and get their solutions under given boundary conditions. This method is favorable for global simulations and we can find the global natures of radiation fields easily, whereas the discretization causes truncation errors depending on the number of bins for the phase space. This disadvantage is critical for the small energy exchanges by nucleon-neutrino scatterings, because their reaction rates are assumed to be "flat" in each energy bin and it is difficult to estimate the energy transfer between energy bins unless we adopt large number of energy bins to simulations. In the numerical calculations of the photon transport, such a small energy exchange is sometimes treated using the Fokker-Planck approximation, in which we expand the distribution function to second-order of the difference between energyies before and after scatterings. Although we can apply this approximation to the calculations of the neutrino transport in the same way and estimate the number flux between energy bins correctly, it remains a critical problem that we can not adopt the large number of energy bins in numerical simulations. Neutrinos, which across the boundary of energy bins, should be located near the boundary due to the small energy exchange. The flatness assumption in energy bins, however, destroys this feature and may lead to overestimate down-scatterings even if we estimate number flux between energy bins.

In Monte Carlo methods, we follow the tracks of "sample particles", which represent a bundle of radiation particles, interacting with matters. We adopt random numbers to solving the radiation transport, for example to choose which reaction will occur among neutrino reactions included in calculations and to determine the energy and angle of neutrinos after reactions. The physical quantities, such as distribution function or number density of radiation fields, correspond to the average behavior of sample particles in the spatial or phase-spatial zone of interest. Monte Carlo methods are favorable for multi-dimensional radiation transports, because we can follow the tracks of sample particles propagating through complicated hydrodynamic backgrounds easily. We can treat physical processes in a simple and direct way in this approach. Statistical errors are, however, big problems for Monte Carlo methods, because they are scaled as $\sqrt{N}$ with the number of sample particles N and the large number of sample particles is necessary to get correct solutions.

In my study, I employ the Monte Carlo method for solving the neutrino transport for two reasons. First, I focus on the specific physical process, or nucleon recoil, which is the strongest point of Monte Carlo methods. Second, it is enough to calculate the neutrino transports in the specific regions, where neutrino spectra may be changed by neutrino-nucleon scatterings. Inside the neutrino sphere, neutrinos experience many times of other reactions with matters and are already thermalized without nucleon recoils. Due to the density and temperature decreases, the number

of reactions also decreases and neutrinos become free-streaming at the outer part of the core. Neutrino-nucleon scatterings may hence affect neutrino spectra between two regions and we do not need to solve the wide region, which is usually focused in dynamical SN simulations.

In the following sections (§§ 3.2.2-3.2.6), I describe the numerical treatments adopted in my Monte Carlo code of neutrino transports. The Monte Carlo approach is usually applied to solving the transport of photons (Lucy, 1999a,b; Kasen et al., 2006; Maeda, 2006). The basic ideas are same as those for photons, except for the Fermi-blocking of neutrinos. For example, the emission rates of neutrinos depend on the blocking factor $1-f$ with the distribution function f. The distribution function changes with time due to absorptions, emissions or scatterings by matters and we have to update it within an appropriate timescale (See Sections 3.2.3, 3.2.4).

3.2.2 Sample particles

In Monte Carlo methods, we follow the tracks of the sample particles, which represent a bundle of neutrinos, interacting with matters. The numbers of sample particles N_s and physical neutrinos N_ν are related with the weight W_s as follow:

$$W_s = \frac{N_\nu}{N_s}. \tag{3.1}$$

In my simulations, the weight is constant for all the time and space.

3.2.3 Treatments of the transport of sample particles

Each sample particle has 6-dimensional information about a space (r, θ, ϕ) and a phase space $(E_\nu, \theta_\nu, \phi_\nu)$ and we calculate their time evolutions by solving geometric equations. To calculate the transport of sample particles, I introduce three lengths : "the reaction length" $l_{\rm r}$, "the background length" $l_{\rm b}$ and "the distribution length" $l_{\rm f}$ for every sample particle.

1. the reaction length $l_{\rm r}$
   I define "the reaction length", which is a distance to the point where the sample particle interacts with matter subsequently, by the optical depth:

   $$\tau(S, E_\nu) = \int_0^S \frac{1}{\lambda(r, E_\nu)} ds, \tag{3.2}$$

   using the local mean free path of all reactions λ:

   $$\lambda(r, E_\nu) = \frac{1}{\sigma_{\rm tot}} \tag{3.3}$$

   where the total cross section $\sigma_{\rm tot} = \sum_\alpha \sigma_\alpha(r, E_\nu)$ using the cross section of α-th type of reaction σ_α. The reaction occurs at $\tau(l_{\rm r}, E_\nu) = \tau_{\rm max}$, which is determined by the random number obeying the Poisson distribution whose average becomes 1.

2. the background length $l_{\rm b}$
   I employ the results of the dynamical SN simulations as a background for the neutrino transport calculations (See Section 3.4.1). In these calculations, the hydrodynamic values, i.e. density, temperature and chemical potential of matters, are uniform in each spatial zone. The length to the nearest spatial boundary of the hydrodynamical background, called "the background length", is defined by the difference between the radial components of the spatial boundary and the current position of sample particle.

3. the distribution length $l_{\rm f}$
   The distribution function of neutrinos changes with time because of interactions with matters or advections. I have to update it within an appropriate timescale, because the Fermi blocking of neutrinos should be taken into account for neutrino reactions. "The distribution length" is defined as $cdt_{\rm f}$ with the remaining time until the update of the distribution function $dt_{\rm f}$ ("distribution time").

Sample particles can propagate independently, but their global times have to be coincident updating the neutrino distribution function. I hence take a time step of calculations as the distribution length $dt = dt_{\rm f}$ and calculate the individual evolution of the sample particle during each time step. If the other two lengths are longer than the distribution length, sample particle of interest just propagates freely during this time step. If not, comparing between the reaction and background lengths, this sample undergoes the process with the shorter length subsequently and I recalculate these length. I repeat this cycle for each sample particle until the distribution time $dt_{\rm f}$ elapses. After calculating the evolutions of all sample particles individually, I update the distribution function described in Section 3.2.4.

3.2.4 Formation of the neutrino distribution function

In this calculation, I employ the spherical symmetric background and the neutrino distribution function is reduced to $f(r, E_\nu, \theta_\nu)$. At every time step $dt_{\rm f}$, I count the number of sample particles inside each volume element in a space and a phase space, and calculate the i, k, j-th discretized neutrino distribution function f_{ijk}:

$$f_{ijk} = \frac{N_{ijk} W_s}{V_i V_{\epsilon,kj}}, \tag{3.4}$$

where i, j and k describe the components of r, E_ν and θ_ν, respectively; the total number of sample particles in the i, k, j-th volume element N_{ijk}; the i-th spatial volume element $V_i = 4\pi \left(r_i^3 - r_{i-1}^3\right)/3$ and the j, k-th phase space volume element $V_{\epsilon,kj} = 2\pi \left(\theta_{\nu,j} - \theta_{\nu,j-1}\right) \left(E_{\nu,k}^3 - E_{\nu,k-1}^3\right)/3$.

3.2.5 Treatment of neutrino reactions

Neutrinos interact with matters via several reactions inside stars (See Table 3.1). I divide neutrino reactions into three processes: absorptions, emissions and scatterings, and adopt different treatments in my Monte Carlo code.

Absorptions and Scattering processes

Existing samples are absorbed or scattered by matters. After the subsequent reaction point is determined by "the reaction length", which is defined by the mean free path of all absorptions and scatterings taken into account, I choose which reaction will occur actually using the uniform random number x whose range is [0, 1]. If we get the random number in the range of $\Sigma_{\alpha=1}^{i-1}\sigma_\alpha/\sigma_{\rm tot} \leqq x < \Sigma_{\alpha=1}^{i}\sigma_\alpha/\sigma_{\rm tot}$, sample particle will undergo the i-th reaction (Tubbs, 1978; Lucy, 2003). If the i-th reaction is an absorption process, such as $\nu_e + n \rightarrow p + e^-$, I stop following the track of this sample particle at this point. If the i-th reaction is a scattering process, such as $\nu + N \rightarrow \nu + N$, on the other hand, I calculate the zenith angle $\psi(\theta_\nu, \phi_\nu)$ and the energy E'_ν after the scattering from the normalized distributions ω_1 and ω_2, following the distribution of the reaction rate $R_i(E_\nu, E'_\nu, \psi)$ defined in Section 3.3. The azimuth angle $\Psi(\theta_\nu, \phi_\nu)$ is determined randomly in the range of [0, 2π]. Then, the angles after the scattering (θ'_ν, ϕ'_ν) are given by the coordinate transformation about the angles (ψ, Ψ).

Note that the normalized distributions ω_1 and ω_2 do not include the blocking factor $1 - f$ (See Section 3.3). Finally, I judge whether this scattering actually occurs or not by using the uniform random number z in the range of [0, 1] after the decision of the angles and energy after scattering. If it satisfies the condition $0 \leq z \leq f(r, E_\nu, \theta_\nu)$, this scattering dose not occur, that is "blocked", and the energy and angles are not changed from thos before scattering. Although the mean free paths of these sample particles seem to be longer than the correct ones, it does not matter because I derive the reaction lengths $l_{\rm r}$ from the cross sections σ_i without the blocking factor. In this case, the reaction lengths are estimated shorter than the correct mean free paths and sample particles interact with matters at the correct frequency finally. In other words, I divide the cross section into two parts: the blocking factor and the other part. The main reason why I adopt this complicated method for the scattering processes is I have to include their reaction rates as a table in my code because of the computational cost.

The table for scattering processes contains the reaction rates only for the part of $E_{\rm in} \leq E_{\rm out}$ with the hydrodynamic values of the given background. In order to guarantee the detail balance, the reaction rates for the other part, $E_{\rm in} > E_{\rm out}$, are calculated using the detail balance relation. These treatments are summarized in Appendix.

Emission processes

The total number of neutrinos emitted during a time step $dt_{\rm f}$ and in a spatial volume element is caluclated by the reaction rates $R_{i,{\rm ems}}$ and I add the corresponding number of sample particles uniformly in that volume element at the beginning of each time step. The energies and angles of sample particles are distributed following the distribution of the reaction rates. I put the distribution time $dt_{\rm f}$ into sample particles randomly in the range of [0, $l_{\rm f}$] in order to get the constant emission rate, and I calculate their evolutions during the remaining time $dt_{\rm f}$ in the same way as the evolutions of the existing sample particles.

3.2.6 Sample input from the boundary

I prepare the inner and outer boundary regions with a finite volume outside of the active region. The number flux of neutrinos from the boundary regions to the active region is given by the distribution function at the boundary. In this study, I employ the distribution functions derived from the background SN simulations and estimate the total number of sample particles in the boundary regions. They are distributed uniformly in a space. Although I solve the transport of the sample particles in the boundary regions, I assume that the sample particles do not interact with matters and change their status in a phase space, in order to get a constant number flux. It is clear that neutrinos come from the active region never go back again. Moreover, I take the width of the boundary regions longer than the distribution length $l_{\rm f}$ and reset sample particles in the boundary regions at the beginning of each time step.

Table 3.1: Neutrino reactions and their set up included in my calculations. Neutrino reactions in the "base" setup are taken into usual dynamical simulations. In the "r1" setup, nucleon recoils of neutrino-nucleon scatterings are added in order to investigate nucleon recoils in Section 3.5.1. In the "e1" setup, I add electron scatterings and investigate which reaction dominates in the thermalization of neutrino spectra in Section 3.5.2.

reactions		model
pair	$e^- + e^+ \longrightarrow \nu + \bar{\nu}$	base, r1, e1
brems	$N + N \longrightarrow N + N + \nu + \bar{\nu}$	base, r1, e1
ecp	$p + e^- \longleftrightarrow n + \nu_e$	base, r1, e1
pc	$n + e^+ \longleftrightarrow p + \bar{\nu}_e$	base, r1, e1
Nsc(iso)	$N + \nu \longrightarrow N + \nu$	base
Nsc(rec)		r1, e1
esc	$e^- + \nu \longrightarrow e^- + \nu$	e1

3.3 Neutrino reactions

3.3.1 Neutrino-nucleon scattering

The reaction rate of neutrino-nucleon scatterings is described as (Mezzacappa and Bruenn, 1993b):

$$R_{\rm Nrec}\left(q, q'\right) = \frac{G_F^2}{2\pi^2\hbar c}\frac{1}{E_\nu E'_\nu}\left[\beta_1 I_1 + \beta_2 I_2 + \beta_3 I_3\right]. \tag{3.5}$$

In the above expression, β's are the following combinations of the coupling constants: $\beta_1 = \left(C_V - C_A\right)^2$, $\beta_2 = \left(C_V + C_A\right)^2$ and $\beta_3 = C_A^2 - C_V^2$, and I's are the functions of

E_ν, E'_ν and the angle ψ between their momenta q and q':

$$\begin{aligned} I_1 &= \frac{2\pi T}{\Delta^5} E_\nu^2 E_\nu'^2 (1-\cos\psi)^2 \frac{1}{\exp\left(\frac{E_\nu - E'_\nu}{T}\right) - 1} \\ &\quad \times \left[AT^3 \left(G_2(y_0) + 2y_0 G_1(y_0) + y_0^2 G_0(y_0) \right) \right. \\ &\quad \left. + BT^2 \left(G_1(y_0) + y_0 G_0(y_0) \right) + CTG_0(y_0) \right], \qquad (3.6) \\ I_2 &= I_1(-q, -q'), \qquad (3.7) \\ I_3 &= \frac{2\pi T m_N^2}{\Delta} E_\nu E'_\nu (1-\cos\psi) \frac{1}{\exp\left(\frac{E_\nu - E'_\nu}{T}\right) - 1} G_0(y_0), \qquad (3.8) \end{aligned}$$

with

$$\begin{aligned} \Delta^2 &\equiv E_\nu^2 + E_\nu'^2 - 2E_\nu E'_\nu \cos\psi, \qquad (3.9) \\ A &\equiv E_\nu^2 + E_\nu'^2 + E_\nu E'_\nu (3 + \cos\psi), \qquad (3.10) \\ B &\equiv E'_\nu \left[2E_\nu'^2 + E_\nu E'_\nu (3 - \cos\psi) - E_\nu^2 (1 + 3\cos\psi) \right], \qquad (3.11) \\ C &\equiv E_\nu'^2 \left[\left(E'_\nu - E_\nu \cos\psi \right)^2 - \frac{E_\nu^2}{2} \left(1 - \cos^2\psi \right) \right. \\ &\quad \left. - \frac{1}{2} \frac{1+\cos\psi}{1-\cos\psi} \frac{m_N^2}{E_\nu'^2} \Delta^2 \right]. \qquad (3.12) \end{aligned}$$

If I assume the energy exchange is much smaller than the neutrino energy before scattering $\Delta E/E_\nu \ll 1$ and the nucleon mass is infinity $m_N \to \infty$, the reaction rate with nucleon recoils returns back to that given by Bruenn (1985), which is incorporated in usual dynamical SN simulations:

$$R_{\rm Niso} = \frac{2\pi G_F^2}{\hbar c} \eta_{NN} \left\{ \left(h_V^N \right)^2 + 3 \left(h_A^N \right)^2 + \left[\left(h_V^N \right)^2 - \left(h_A^N \right)^2 \right] \cos\psi \right\} \delta\left(E_\nu - E'_\nu \right), \qquad (3.13)$$

where η_{NN} is defined as

$$\eta_{NN} \equiv \int \frac{2d^3 p_N}{(2\pi)^3} \tilde{F}_N \left(\tilde{E} \right) \left[1 - \tilde{F}_N \left(\tilde{E} \right) \right]. \qquad (3.14)$$

The cross section for neutrino-nucleon scatterings is calculated by the reaction rates $R_* = R_{\rm Nrec}, R_{\rm Niso}$:

$$\begin{aligned} \sigma_{\rm N} &= \int \tilde{R}_* d\cos\psi, \qquad (3.15) \\ \tilde{R}_* &= \frac{1}{(2\pi)^3} \int 2\pi E_\nu'^2 R_* dE'_\nu. \qquad (3.16) \end{aligned}$$

I decide the energy E'_ν and the angles $\cos\theta'_\nu$, ϕ'_ν after scattering by the following procedures. At first, I get the angle ψ using random numbers and the normalized spectrum:

$$\omega_1(E_\nu, \cos\psi_k) = \frac{\int_{\cos\psi_{k-1}}^{\cos\psi_k} \int 2\pi E_\nu'^2 R_*(E_\nu, E'_\nu, \cos\psi_k) dE'_\nu d\cos\psi}{\int_{-1}^{1} \int 2\pi E_\nu'^2 R_*(E_\nu, E'_\nu, \cos\psi) dE'_\nu d\cos\psi}. \qquad (3.17)$$

Using the derived ψ_k, the energy after scattering is derived in the same way:

$$\omega_2\left(E_\nu, E'_{\nu,i}, \cos\psi_k\right) = \frac{\int_{E'_{\nu,i-1}}^{E'_{\nu,i}} 2\pi E'^2_\nu R_*\left(E_\nu, E'_{\nu,i}, \cos\psi_k\right) dE'_\nu}{\int_{E'_{\min}}^{E'_{\max}} 2\pi E'^2_\nu R_*\left(E_\nu, E'_\nu, \cos\psi_k\right) dE'_\nu}. \tag{3.18}$$

I define the minimum and maximum energies $E'_{\min}$, $E'_{\max}$, at which the reaction rates become 10^{-5} times smaller than the maximum rate.

3.3.2 Neutrino-electron or neutrino-positron scatterings

The reaction rates of neutrino-electron and neutrino-positron scatterings are derived from those of neutrino-nucleon scatterings in eqs. (3.5)-(3.12), if I change the coefficients β's summarized in Table 3.2, the target mass $m_N \to m_e$ and the chemical potential $\mu_N \to \mu_e, -\mu_e$ for electrons and positrons, respectively. In this paper, I denote the total reaction rates of electron- and positron-scatterings as $R_{\rm esc}$ and define the cross section $\sigma_{\rm esc}$ and the normalized spectra ω_1 and ω_2 in the same way as those for nucleon scatterings.

Table 3.2: The coefficients for the reaction rates of neutrino-electron and neutrino-positron scatterings. In this expression, $C'_{Ve} = C_{Ve} + 1$ and $C'_{Ae} = C_{Ae} + 1$ with $C_{Ve} = -1/2 + 2\sin^2\theta_w$ and $C_{Ae} = 1/2$.

reaction	β_1	β_2	β_3
$\nu_e e^- \ / \ \bar{\nu}_e e^+$	$\left(C'_{Ve} + C'_{Ae}\right)^2$	$\left(C'_{Ve} - C'_{Ae}\right)^2$	$C'^2_{Ae} - C'^2_{Ve}$
$\nu_e e^+ \ / \ \bar{\nu}_e e^-$	$\left(C'_{Ve} - C'_{Ae}\right)^2$	$\left(C'_{Ve} + C'_{Ae}\right)^2$	$C'^2_{Ae} - C'^2_{Ve}$
$\nu_x e^- \ / \ \bar{\nu}_x e^+$	$\left(C_{Ve} + C_{Ae}\right)^2$	$\left(C_{Ve} - C_{Ae}\right)^2$	$C^2_{Ae} - C^2_{Ve}$
$\nu_x e^+ \ / \ \bar{\nu}_x e^-$	$\left(C_{Ve} - C_{Ae}\right)^2$	$\left(C_{Ve} + C_{Ae}\right)^2$	$C^2_{Ae} - C^2_{Ve}$

3.3.3 Electron capture on free proton and positron capture on free neutron

The emission rate of EC's on free protons is the right hand side of eq. (2.49):

$$R_{\rm EC,ems} = \frac{{G_F}^2}{\pi\hbar c}\eta_{\rm pn}\left({g_V}^2 + 3{g_A}^2\right)\left(E_{\nu_e} + Q\right)^2\sqrt{1 - \frac{m_e^2}{\left(E_{\nu_e} + Q\right)^2}}f_e\left(E_{\nu_e} + Q\right).$$

The expression of the emission rate for PC on free neutrons is very similar to that of EC on free protons except for the threshold for the neutrino energy (Bruenn, 1985).

$$\begin{aligned} R_{\rm PC,ems} = {} & \frac{{G_F}^2}{\pi\hbar c}\eta_{\rm np}\left({g_V}^2 + 3{g_A}^2\right)\left(E_{\nu_e} - Q\right)^2\sqrt{1 - \frac{m_e^2}{\left(E_{\nu_e} - Q\right)^2}} \\ & \times f_{e^+}\left(E_{\nu_e} - Q\right)\Theta\left(E_{\nu_e} - Q - m_e\right). \end{aligned} \tag{3.19}$$

The absorption rates are derived from the detailed balance relations $R_{*,\rm ems}(1 - f_{*,\rm eq}) = R_{*,\rm abs} f_{*,\rm eq}$ with the Fermi-Dirac distribution $f_{*,\rm eq}$ with the chemical potential μ_e for EC and $-\mu_e$ for PC. The cross sections are calculated by the reaction rates $R_* = R_{\rm EC,abs}, R_{\rm PC,abs}$:

$$\sigma_* = R_{*,\rm abs}. \tag{3.20}$$

3.3.4 Electron-positron pair annihilation

I use the reaction rate of electron-positron pair annihilations described in the previous section:

$$\begin{aligned}
R_{\rm pair} &= \frac{8G_F^2}{(2\pi)^2 \hbar c} \left[\beta_1 I_1 + \beta_2 I_2 + \beta_3 I_3 \right] \\
I_1 (E_\nu, E_{\bar\nu}, \cos\psi) &= -\frac{2\pi T E_\nu^2 {E_{\bar\nu}}^2 (1-\cos\psi)^2}{[\exp(E_\nu + E_{\bar\nu})/T - 1] {\Delta_e}^5} \left\{ AT^2 \left([G_2(y_{\rm max}) - G_2(y_{\rm min})] \right.\right. \\
&\quad + [2y_{\rm max} G_1(y_{\rm max}) - 2y_{\rm min} G_1(y_{\rm min})] + \left.\left[y_{\rm max}^2 G_0(y_{\rm max}) - y_{\rm min}^2 G_0(y_{\rm min}) \right] \right) \\
&\quad + BT \left([G_1(y_{\rm max}) - G_1(y_{\rm min})] + [y_{\rm max} G_0(y_{\rm max}) - y_{\rm min} G_0(y_{\rm min})] \right) \\
&\quad + C [G_0(y_{\rm max}) - G_0(y_{\rm min})] \Big\}, \\
I_2 &= I_1 (E_{\bar\nu}, E_\nu, \cos\psi), \\
I_3 &= -\frac{2\pi T m_e^2 E_\nu E_{\bar\nu} (1-\cos\psi)}{[\exp(E_\nu + E_{\bar\nu})/T - 1] \Delta_e} [G_0(y_{\rm max}) - G_0(y_{\rm min})],
\end{aligned}$$

with

$$\begin{aligned}
{\Delta_e}^2 &\equiv {E_{\bar\nu}}^2 + {E_\nu}^2 + 2E_\nu E_{\bar\nu} \cos\psi, \\
A &\equiv {E_{\bar\nu}}^2 + {E_\nu}^2 - E_\nu E_{\bar\nu} (3 + \cos\psi), \\
B &\equiv E_\nu \left[-2{E_\nu}^2 + {E_{\bar\nu}}^2 (1 + 3\cos\psi) + E_\nu E_{\bar\nu} (3 - \cos\psi) \right], \\
C &\equiv E_\nu^2 \left[(E_\nu + E_{\bar\nu} \cos\psi)^2 - \frac{1}{2} {E_{\bar\nu}}^2 \left(1 - \cos\psi^2\right) - \frac{1}{2} \left(\frac{m_e \Delta_e}{E_\nu} \right)^2 \frac{1+\cos\psi}{1-\cos\psi} \right].
\end{aligned}$$

The emission rate for neutrinos is derived from the integration of the reaction rate over the energy of anti-neutrinos $E_{\bar\nu}$:

$$R_{\rm pair,ems} = \int\int \frac{1}{2E_\nu (2\pi)^3} \frac{2\pi E_{\bar\nu}^2}{2E_{\bar\nu} (2\pi)^3} R_{\rm pair} (1 - f_{\bar\nu}) \, d\cos\psi dE_{\bar\nu}. \tag{3.21}$$

The cross section is calculated by the reaction rate:

$$\sigma_{\rm pair} = \int\int \frac{1}{2E_\nu (2\pi)^3} \frac{2\pi E_{\bar\nu}^2}{2E_{\bar\nu} (2\pi)^3} R_{\rm pair} f_{\bar\nu} d\cos\psi dE_{\bar\nu}. \tag{3.22}$$

For the emission rate and cross section of anti-neutrinos, I integrate the reaction rate over E_ν instead of $E_{\bar\nu}$. In this calculation, I employ the distribution function for the other neutrinos derived from the background simulations.

3.3.5 Nucleon bremsstrhlung

I calculate the reaction rate of nucleon bremsstrhlungs $R_{\rm brem}$ based on Friman and Maxwell (1979); Maxwell (1987). The emission and absorption rates $R_{\rm brem,ems}$, $R_{\rm brem,abs}$ and the cross section $\sigma_{\rm brem}$ are derived in the same way as those of pair annihilations.

3.4 Code check

3.4.1 Comparison between Monte Carlo code and discretized Boltzmann solver

Set up of the comparison

I perform the comparison study between my Monte Carlo code and discretized Boltzmann solver developed by Nagakura et al. (2014, 2017) for steady-state neutrino transport calculations in spherical symmetry. The results of the dynamical SN simulation of the progenitor with $M_{\rm ZAMS} = 11.2\ M_\odot$ at 100 ms after the core bounce are employed on the static hydrodynamical background in this comparison. Figure 3.1 shows the radial profiles of density, temperature and electron fraction of this model. I find that the shock wave is stalled at the radius $\sim$ 100-200 km. I focus on the deepest region (r = 20-25 km) and the middle region (r = 28-34 km) in this comparison. The number fluxes of neutrinos from the outer and inner boundaries are estimated by the neutrino distribution functions derived from the background simulation. The setup of neutrino reactions included in this comparison is named as "base" in Table 3.1. I use 2×10^6 sample particles and take $dt_{\rm f} = 10^{-7}$ for the distribution time. I define a steady-state as the condition in which the total number of sample particles fluctuates around a certain value. As neutrino distribution functions fluctuate at each time step even in the steady-state, I take their average over 10000 time steps after the steady-state is achieved and calculate number spectra of neutrinos from the averaged distribution functions.

Figure 3.2 shows the comparison of the number spectra for ν_e's (top), $\bar{\nu}_e$'s (middle) and ν_x's (bottom) between the Monte Carlo code and the discretized Boltzmann solver. The left panels show number spectra from 20-25 km in the deepest region. The color lines show the results of the Monte Carlo code at the different radius and I plot the neutrino spectra with different angles $\cos\theta_\nu$ in the same color. Neutrino spectra with $\cos\theta_\nu = 0.973$ derived from the discretized Boltzmann solver are shown by gray dots. I find that neutrinos are thermalized and have a isotropic distribution in this region and that the neutrino spectra derived from both methods are consistent. In the right panels, I pick up the neutrino spectra at r = 34 km in the middle region, where the distribution of neutrinos becomes forward-peaked gradually. The different colors denote the different angle $\cos\theta_\nu$ and I find that both results are also consistent in this region.

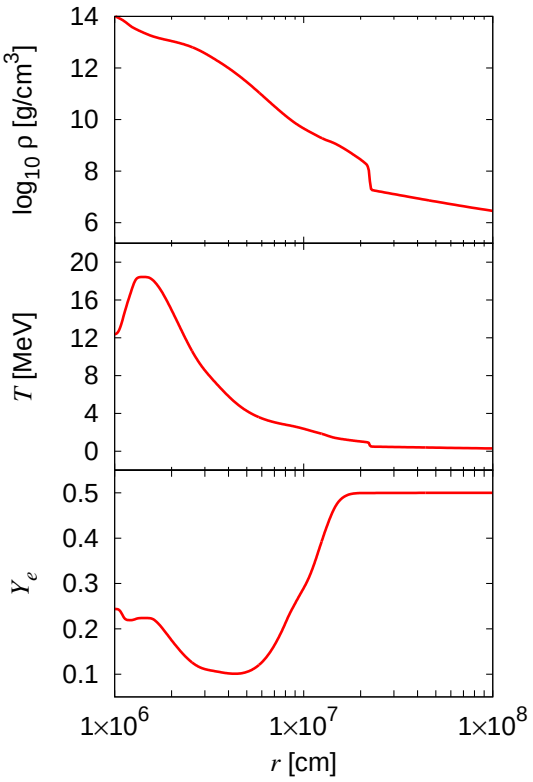

Figure 3.1: The radial profiles of density, temperature and electron fraction of the progenitor model with $M_{\rm ZAMS} = 11.2\ M_\odot$ at 100 ms after the core bounce, which is employed on the static hydrodynamical background (Nagakura et al., 2014, 2017).

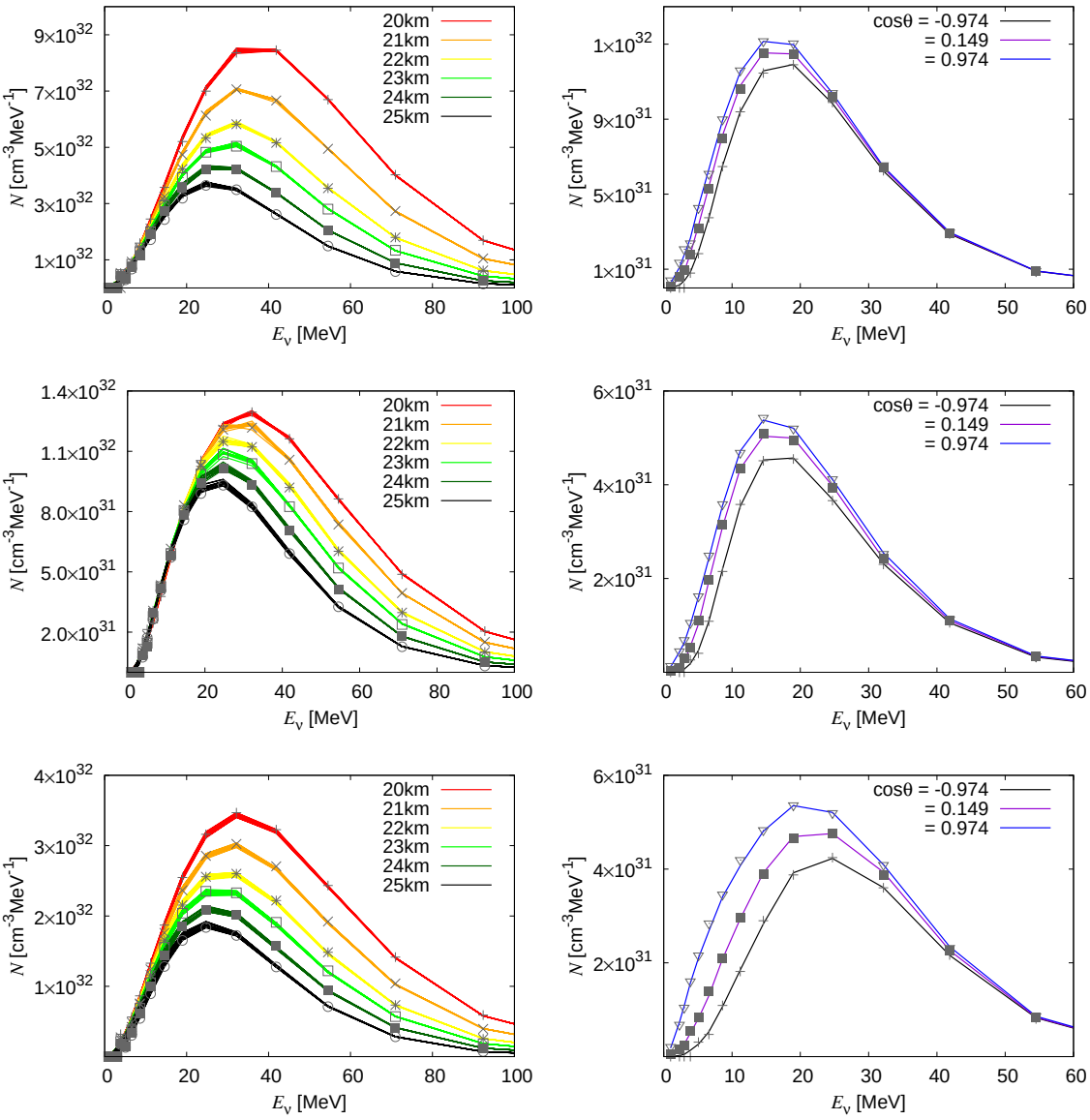

Figure 3.2: The comparison of the number spectra of ν_e's (top), $\bar{\nu}_e$'s (middle) and ν_x's (bottom) between the Monte Carlo code and the discretized Boltzmann solver. In the left panels, color lines denote the number spectra at the different radius derived from the Monte Carlo code and the results with the different angle $\cos\theta_\nu$ are plotted in the same color. The gray plots are derived from the discretized Boltzmann solver. In the right panels, the number spectra with the different angle $\cos\theta_\nu$ at the radius $r = 34$ km are plotted with different colors.

3.4.2 Detailed balance by nucleon recoils

I focus on the effects of nucleon recoils in this paper. The detailed balance condition for neutrino-nucleon scatterings:

$$R'_{\rm Nrec}\left(E_\nu, E'_\nu\right) f_{\rm eq}\left(E_\nu\right)\left(1 - f_{\rm eq}\left(E'_\nu\right)\right) = R'_{\rm Nrec}\left(E'_\nu, E_\nu\right)\left(1 - f_{\rm eq}\left(E_\nu\right)\right) f_{\rm eq}\left(E'_\nu\right) \quad (3.23)$$

should be satisfied in order to treat the thermalization of neutrino spectra precisely. In this expression, $R'_{\rm Nrec}$ is the integrated reaction rate over the angle ψ:

$$R'_{\rm Nrec}\left(E_\nu, E'_\nu\right) \equiv \int_{-1}^{1} 2\pi E'^2_\nu R'_{\rm Nrec}\left(E_\nu, E'_\nu, \cos\psi\right) d\cos\psi. \quad (3.24)$$

I incorporate the table of reaction rates for $E_\nu \leq E'_\nu$, which are calculated by the hydrodynamic values, i.e. temperature T and chemical potential of nucleons μ_N. In order to guarantee the detailed balance, the reaction rates for $E'_\nu > E_\nu$ are derived from those for $E_\nu \leq E'_\nu$ in the table. The detailed derivation is described in Appendix.

Figure 3.3 shows the thermalization of neutrino spectrum by neutrino-nucleon scatterings. I assume the uniform and homogeneous neutrons with $T = 10.181$ MeV and $\mu_n = 920.93$ MeV as a background and give all the sample particles 30 MeV initially. Different colors denote the different time steps. The expected thermal spectrum (red dotted) is defined by the Fermi-Dirac distribution:

$$N\left(E_\nu\right) = \frac{1}{\left(2\pi\hbar c\right)^3} \frac{4\pi E_\nu^2}{1 + \exp\left(\frac{E_\nu - \mu_\nu}{T}\right)}. \quad (3.25)$$

Since the total number of neutrinos n_ν is conserved in this calculation, the chemical potential of neutrinos μ_ν can be derived from n_ν and T. I find that neutrino spectrum approaches the expected thermal one and they are good agreement with each other finally (See red dotted and black solid lines in Figure 3.3). Then, I confirm that the detailed balance by neutrino-nucleon scatterings is achieved in my code surely.

3.5 Results

3.5.1 The effect of nucleon recoils

Iso-energy scattering and nucleon recoils

Neutrino-nucleon scattering is assumed to be iso-energy, which means that only the angles are changed by scatterings, because the energy exchange by nucleon recoils is too small to be resolved in the recent dynamical SN simulations. At first, I investigate the effect of nucleon recoils for the reaction rates compared with those under the assumption of iso-energy scattering. The reaction rates for the iso-energy scattering, eq. (3.13), are derived from those of non-iso energy scattering, eq. (3.5), taking a limit of $m_N \to \infty$. The top panel of Figure 3.4 shows the dependence of the proton mass for the reaction rates of neutrino-proton scatterings. The vertical line is the reaction rates $R_{\rm Nrec}$, eq. (3.5), and the horizontal line is the ratio of

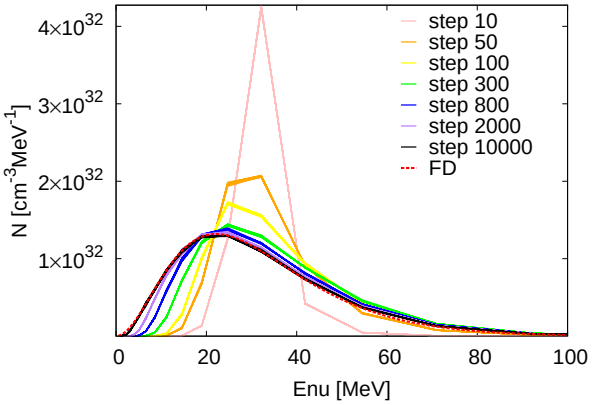

Figure 3.3: The thermalization of neutrino spectrum by neutrino-nucleon scatterings. Solid lines denote the time evolution of the neutrino spectrum and red dotted line denotes the expected thermal distribution defined by the Fermi-Dirac distribution with $T = 10.181$ MeV and $\mu_\nu = -2.496$ MeV.

the energy difference to the initial energy $\Delta\epsilon/E_\nu$. If I increase the proton mass practically, the distribution of the reaction rates becomes sharp with a large peak at $\Delta\epsilon/E_\nu = 0$, where there is no energy change by proton scatterings, or iso-energy. Note that I conserve the number of protons and change their chemical potential with the increase of their mass.

In addition to the broadening of energy spectra, the main effects of nucleon recoils are the reduction of the cross sections at the high energy (middle) and the change of their angle dependence (bottom) shown in Figure 3.4. I calculate the cross sections $\sigma_{\rm N}$ for protons at $T = 13.95$ MeV, $\rho = 10^{14}$ g/cm^3 and $\mu_p = 876.92$ MeV and find that they are reduced especially at the high energy in the middle panel. The reaction rates $\tilde{R}_{\rm Nrec}$ for protons are calculated at the same condition assuming that the initial energy $E_\nu = 40$ MeV and find that they are reduced in the case of back-scatterings.

Steady-state calculation

In order to investigate the effect of nucleon recoils, I perform the steady-state calculation of the neutrino transport using the Monte Carlo method on a static background. I use the same progenitor model as that employed in the code comparison shown in Figure 3.1 and the inner and outer boundaries are put at 20 and 100 km, respectively, at which neutrinos interact enough number of times to follow thermal distribution and escape freely. In this calculation, I prepare two setups of neutrino reactions, "base" and "r1" in Table 3.1. In "r1" set up, nucleon recoils of neutrino-nucleon scatterings are taken into account in addition to the "base" setup. The neutrino fluxes from the boundary regions are estimated by the neutrino distribution functions of the background simulations. For both calculations, I use 2×10^6 sample particles and take $dt_{\rm f} = 10^{-7}$ for the distribution time.

Figure 3.5 shows the number spectra of neutrinos for both setups of reactions. Line colors denote the different radius and the solid and dotted lines denote the

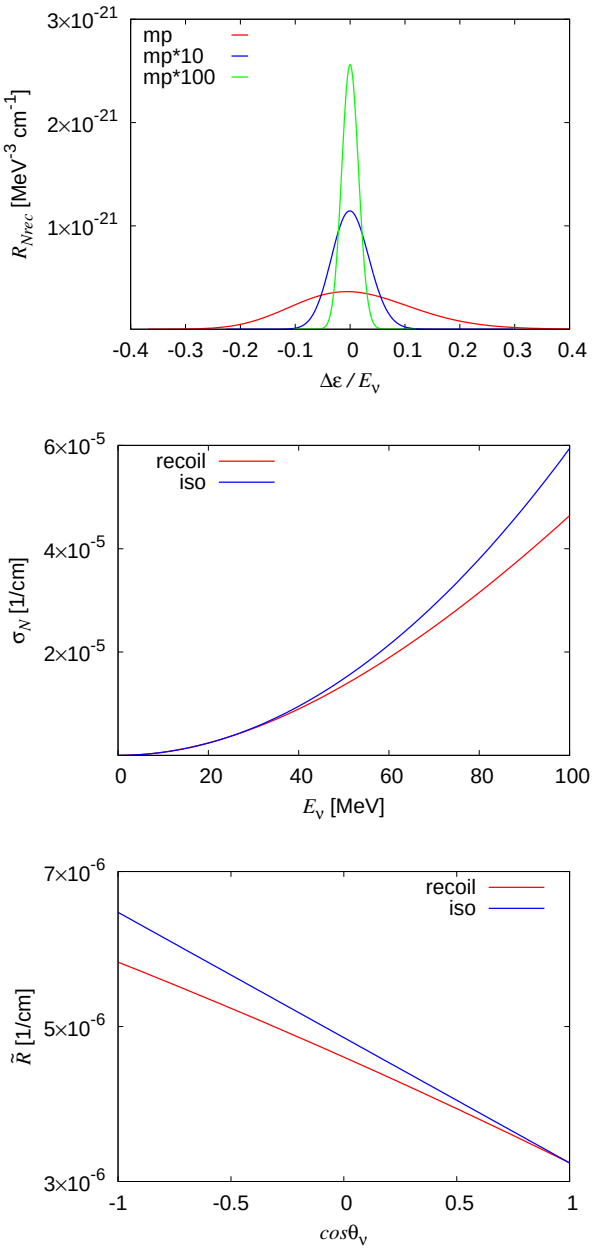

Figure 3.4: *Top panel*: The dependence of proton mass. I calculate the reaction rates for three proton mass, i.e., m_p (red), $10m_p$ (blue) and $100m_p$ (green). The horizontal line shows the ratio of the energy difference to the initial energy. At $\Delta\epsilon/E_\nu = 0$, proton scatterings are regarded as iso-energy. *Middle panel*: The energy dependences of the cross sections for iso- (blue) and non-iso energy scatterings (red). *Bottom panel*: The angle dependences of the reaction rates at input energy $E_\nu = 40$ MeV for iso- (blue) and non-iso energy scatterings (red).

results of "r1" and "base" setup, respectively. The number spectrum is defined as

$$N\left(r, E_\nu\right) = \frac{1}{\left(2\pi\hbar c\right)^3} \int 2\pi E_\nu^2 f\left(r, E_\nu, \theta_\nu\right) d\cos\theta_\nu. \tag{3.26}$$

The spectra of ν_e's (top) and $\bar{\nu}_e$'s (middle) do not change even if nucleon recoils are taken into account, whereas in that of ν_x's (bottom) the number of neutrinos with high energy decreases due to the down-scatters by nucleons. The average energy of ν_x's is reduced $\sim$15% in Figure 3.6 and the number density also decreases $\sim$7% because the opacity is reduced by nucleon recoils and the decrease of average energy also reduces the reaction rates, which are proportional to the square of energy.

In order to understand the different responses to nucleon recoils in flavors, I investigate the number of neutrino reactions. The radial profiles of the number of neutrino reactions included in my calculations are shown in the left panels of Figure 3.7. Line colors denote the different reactions. The vertical line shows the number of sample particles, which experience each neutrino reaction per unit time and volume, denoted as n_s. I find that EC dominates the other reactions for ν_e's in the top panel, so the spectrum is not changed by nucleon recoils. The dominant reaction for ν_x's is, on the other hand, neutrino-nucleon scattering, which makes the spectrum pinched in the "r1" setup (See bottom panel). For $\bar{\nu}_e$'s in the middle panel, I find that the number of neutrino-nucleon scattering is larger than those of the other reactions. This consequence seems to be inconsistent with the result that the spectrum of $\bar{\nu}_e$'s do not change by nucleon recoils, but I find that this can be attributed to the small energy exchange by neutrino-nucleon scattering.

The right panels of Figure 3.7 show the energy exchanged between neutrinos and matters. The vertical line shows the energies which are exchanged between sample particles and matters by each neutrino reaction per unit time and volume, denoted as E_s. The exchange energy by neutrino-nucleon scattering is defined as $|E'_\nu - E_\nu|$ and those by absorption and emission are defined as the neutrino energy of absorbed or emitted sample particles. In these figures, the energy exchanged via pair-annihilation and bremsstrhlung are put together as "other". I find the same consequences for ν_e's (top) and ν_x's (bottom) as their number of reactions n_s, whereas PC dominates the other reactions for the energy exchange between matters and $\bar{\nu}_e$'s (middle) unlike the results of n_s.

As a result, nucleon recoils of neutrino-nucleon scattering reduce the average energy of ν_x's and make their spectra pinched. This feature is consistent with the previous work by Keil et al. (2003).

3.5.2 Electron scattering and nucleon scattering

Although the electron fraction behind the shock wave is $Y_e < 0.5$ in Figure 3.1, the energy exchanged by electron scatterings is larger than that by nucleon scatterings because of the smaller mass of electrons $m_e = 0.511$ MeV. In the top panel of Figure 3.8, I compare the energy exchange by nucleon- and electron-neutrino scatterings for $E_\nu = 25$ MeV and $\cos\theta_\nu = -1.0$. The vertical line is the normalized reaction rate and the horizontal line shows the ratio of the energy difference to the input energy as same as Figure 3.4. The peak of the reaction rates for electron

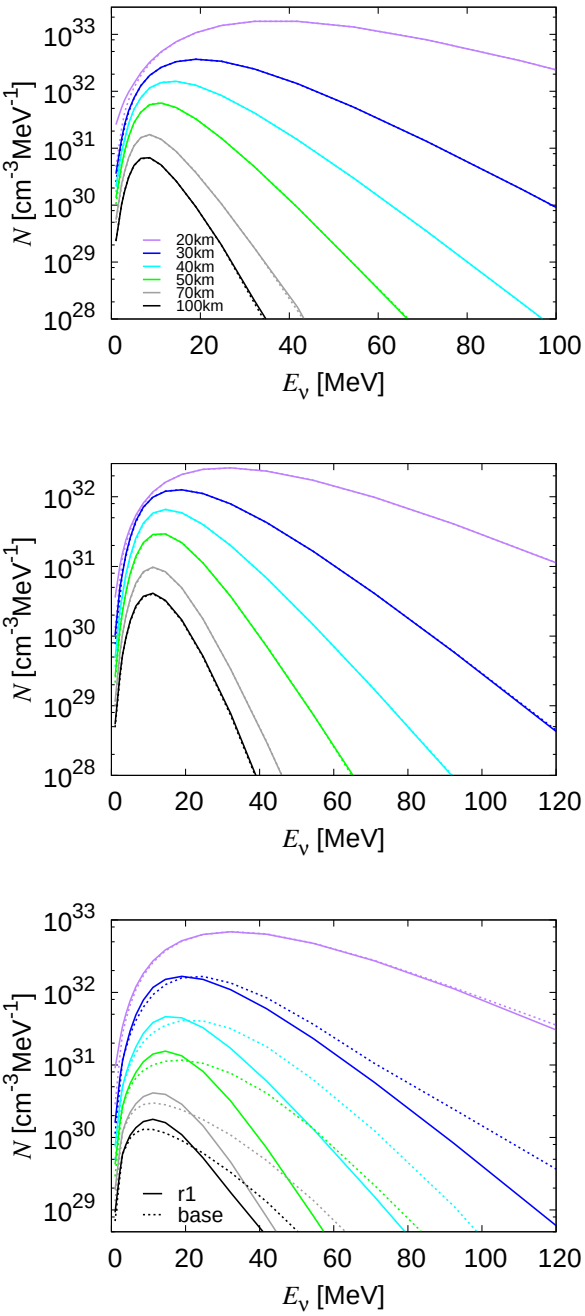

Figure 3.5: The number spectra of neutrino for the "base" (dotted) and "r1" (solid) setups. Line colors denote the different radius. The top panels show the spectra of ν_e's, the middle ones show those of $\bar{\nu}_e$'s and the bottom ones show those of ν_x's.

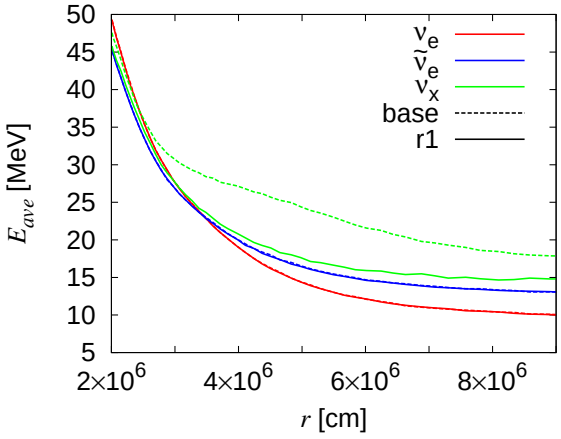

Figure 3.6: The radial profile of the average energy of ν_e's (red), $\bar{\nu}_e$'s (blue) and ν_x's (green). Solid line denotes the "r1" setup, whereas dotted line denotes the "base" setup of neutrino reactions.

scattering is located farther from the iso-energy condition $\Delta\epsilon/E_\nu = 0$, which means that neutrinos give larger energy to matters by electron scatterings than that by nucleon scatterings. The cross section of nucleon scatterings $\sigma_{\rm N}$ is, on the other hand, larger than that of electron scatterings $\sigma_{\rm esc}$ with the energy $E_\nu \gtrsim$ a few MeV in the bottom panel of Figure 3.8. I calculate these cross sections at $T = 15.109$ MeV, $\rho = 1.113 \times 10^{13}$ g/cm^3, $\mu_p = 874.02$ MeV, $\mu_n = 911.01$ MeV and $\mu_e = 53.148$ MeV.

In order to investigate which reaction is important for the thermalization of neutrino spectra, I perform the steady-state calculations using the same Monte Carlo code. In this calculation, I include "e1" setup of the neutrino reactions in Table 3.1, in which electron-neutrino scatterings are taken into account in addition to "r1" setup. The number of sample particles and the distribution time are same as those in the previous calculations. Figure 3.9 shows the energy difference same as the left panels of Figure 3.7 except that electron-neutrino scattering (orange) is added. I find that the energy exchanged by nucleon scatterings is larger than that by electron scatterings in all flavor. Thompson et al. (2000) calculated the thermalization of ν_x's at a uniform background and investigate which reaction is important for the thermalization. They also claimed that nucleon scatterings are more important than electron scatterings for the thermalization, which is consistent with my results.

3.6 Summary and discussions

I focus on the energy exchange by neutrino-nucleon scatterings, or nucleon recoils, for the first step to make a precise theoretical prediction of SN neutrino luminosities and spectra. In the recent numerical studies, the number of energy and angle bins are not enough to resolve the small energy exchange. The number of scatterings is, however, large because of numerous nucleons inside stars, and it is necessary to investigate how much neutrino spectra are changed by nucleon recoils. In this

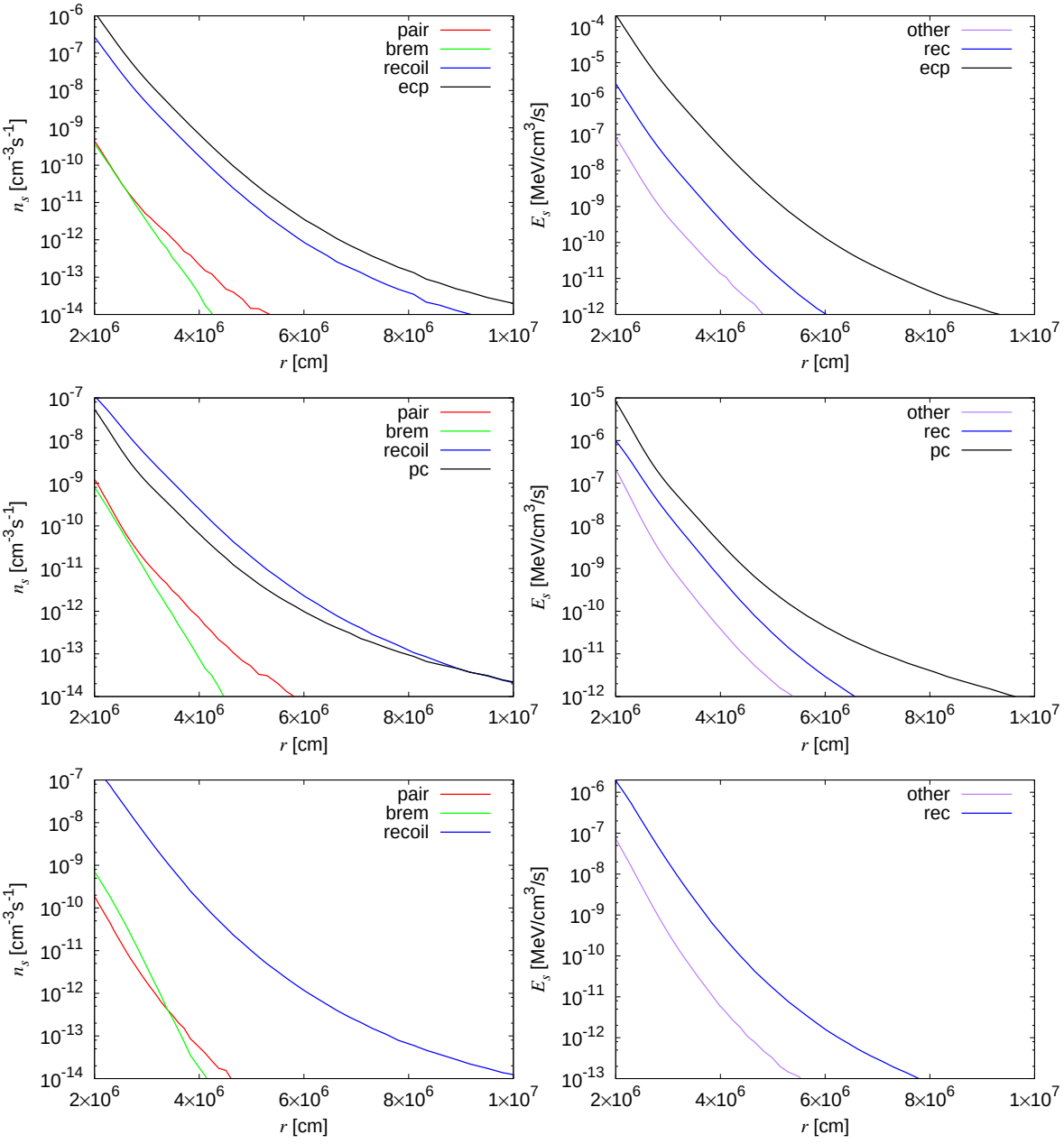

Figure 3.7: The radial profiles of the number of reactions (left) and the energy exchanged between neutrinos and matters (right) for ν_e's (top), $\bar{\nu}_e$'s (middle) and ν_x's (bottom). In the right panels, the energy exchanges by the pair-annihilation and bremsstrhlung are put together as "other".

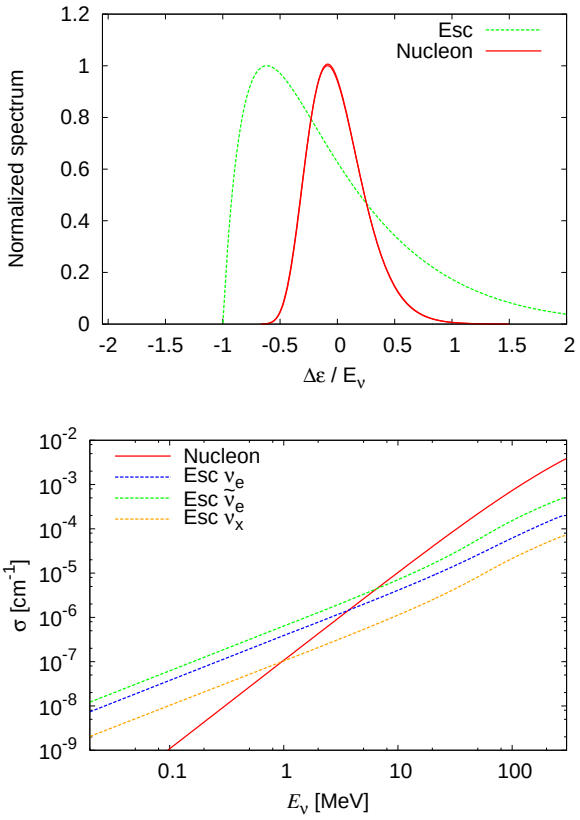

Figure 3.8: The top panel shows the comparison of energy exchanges between nucleon- (red solid) and electron-scatterings (green dotted). The bottom panel shows the comparison of the cross sections. The cross section of electron scatterings (dotted) depends on neutrino flavors.

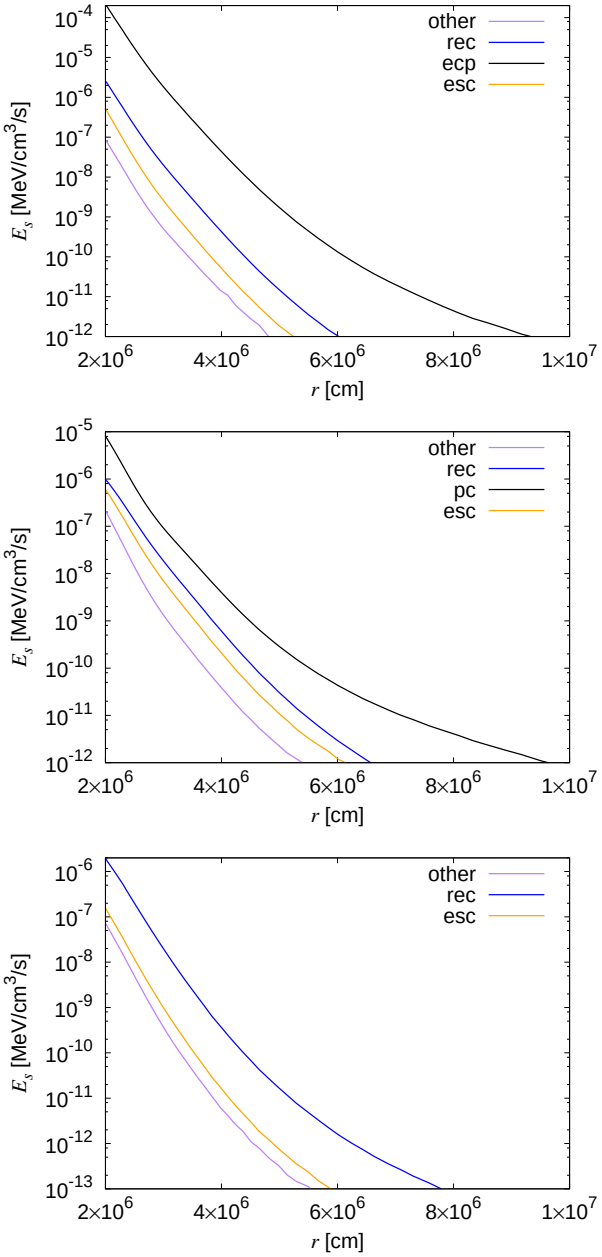

Figure 3.9: The same as the left panels of Figure 3.7 except that electron scattering (orange) is added.

study, I hence carry out the steady-state calculations of the neutrino transport from the PNS surface to the region, where neutrino reactions can be neglected, based on the hydrodynamical backgrounds derived from the dynamical SN simulations. Then I estimate the change of neutrino spectra by nucleon recoils and discuss which reaction dominates in the thermalization of neutrino spectra.

Since we can treat the physical processes in a simple and direct way, I adopt the Monte Carlo method to the neutrino transport and develop a new Monte Carlo code for the steady-state calculations of the neutrino transport. For the credibility of my code, I perform two test calculations. At first, I compare neutrino spectra derived from the steady-state neutrino transport calculations in spherical symmetry using my Monte Carlo code with those by the discretized Boltzmann solver developed by Nagakura et al. (2014, 2017), employing the results of the dynamical SN simulation for the progenitor with $M_{\rm ZAMS} = 11.2\ M_\odot$ at 100 ms after the core bounce on the static hydrodynamic background. Their neutrino spectra are in good agreement with each other. Second, I confirm the detailed balance for neutrino-nucleon scatterings, which are a main interest in this study. In my code, the reaction rates of scattering processes are included as table and I derive the reaction rates for the part of $E_\nu > E'_\nu$ from those for the part of $E_\nu \leq E'_\nu$, which are included in the table, in order to guarantee the detailed balance. From the calculation of thermalization of neutrino spectra at the uniform background, I confirm that the detailed balance is achieved by neutrino-nucleon scatterings in my code surely.

Due to nucleon recoils, there are three effects for the reaction rates: the broadening of the distribution of energy after scattering, the reduction of the cross section and the change of the angle dependence of reaction rate. In order to investigate nucleon recoils, I perform the steady-state calculation of the neutrino transport using Monte Carlo method on a static background. I use the same progenitor model as that employed in the code comparison and the inner and outer boundaries are put at 20 and 100 km, respectively. I prepare two setups of neutrino reactions: base and r1 and in the latter setup nucleon scatterings are taken into account. As a result, I find that the number spectra of ν_x's are changed significantly by nucleon recoils. The number of ν_x's at high energy decreases because of down-scatterings and their average energy is reduced $\sim 15\%$. This is because the number of nucleon scatterings is larger than those of the other reactions. For ν_e's and $\bar{\nu}_e$'s, the number spectra do not change even if I take nucleon recoils into account. This consequence for ν_e's can be understood easily comparing the number of reactions among all neutrino reactions taken into account and the charged current reactions dominate neutrino-nucleon scatterings for ν_e's. On the other hand, the number of nucleon scatterings is larger than the charged current reactions for $\bar{\nu}_e$'s. This is due to the small energy exchange by nucleon scatterings. I find that the energy exchanged by nucleon scatterings is smaller than that by charged current reactions, which means that the spectra of $\bar{\nu}_e$'s are thermalized by the latter reactions mainly. The reduction of average energy of ν_x's makes faster contraction of PNS and increases the temperature inside PNS. The following increase of the luminosities of ν_e's and $\bar{\nu}_e$'s enhances the explosion probability.

Although the electron fraction is $Y_e < 0.5$ behind the shock wave, the energy exchanged by electron scatterings is larger than that by nucleon scatterings because

of the smaller mass of electrons $m_e = 0.511$ MeV. The cross section of nucleon scatterings is, on the other hand, larger than that of electron scatterings with the energy $E_\nu \gtrsim$ a few MeV. In order to investigate which reaction is important for the thermalization of neutrino spectra, I perform the steady-state calculations using Monte Carlo method with the setup "e1" of neutrino reactions. I find that nucleon scatterings dominate electron scatterings in the thermalization of neutrino spectra in all flavor. This is consistent with the results derived from the calculations at the uniform background (Thompson et al., 2000).

This study is just the fist step for my project, in which we get the precise prediction of SN neutrinos. In order to achieve the goal of my research, a few important physics still remain. First, I have to take the corrections for neutrino reactions into my code, for example weak magnetism, strange quark effects and medium modifications of nucleons. Although they are high order corrections and change the reaction rates slightly as well as nucleon recoils, several numerical studies find that they reduce the neutrino opacities and affect the dynamics of PNS (Melson et al., 2015; Kotake et al., 2018). In the recent dynamical simulations, the reduction by these corrections is taken into account using the approximation formula by (Horowitz, 2002) but there is still problem to employ them in the dynamical simulations because of the small energy exchanges. Second, the multi-dimensional studies are inevitable. The dynamical instabilities, such as convection or SASI, form the non-spherical symmetric density and temperature profiles, which may affect neutrino reactions. I should extend my Monte Carlo code to the neutrino transport calculation using the multi-dimensional hydrodynamic backgrounds. The most serious problem in the current SN neutrino studies is the neutrino oscillations. Sawyer (2016) claimed that neutrino pair conversions $\nu_e\bar{\nu}_e \rightarrow \nu_x\bar{\nu}_x$ occur near the PNS surface in the faster timescale. Due to the flavor conversions, ν_e's convert to ν_x's and reduce their number flux at high density (spectral swap) because the number flux of ν_x's is smaller than thot of ν_e's and the number of ν_x's, which are converted to ν_e's by flavor conversion, is small (See Section 1.4). The oscillation scale of fast conversions is much smaller that the scale height of hydrodynamical values in PNS and it is difficult to take them in the dynamical simulations. I think that Monte Carlo method is favorable for this short scale conversion because their consequences do not depend on the number of bins so much. In order to take neutrino oscillations into account, the multi-flavor transport scheme is necessary. Not only neutrino oscillations but also μ creation inside PNS requests the same thing. The creation of μ's makes a difference between ν_μ and ν_τ because ν_μ's can interact with matters via the charged current reactions (Bollig et al., 2017). I have to solve these remaining problems individually in the future.

Chapter 4

Conclusion

At the SN explosion in 1987 (SN1987A), Koshiba et al. observed the supernova neutrinos released from the PNS and contributed greatly to the understanding of the explosion mechanism. Thirty years have passed since then, and neutrino detectors have been developed further and more detailed observation will be possible. At the Super Kamiokande, which observes $\bar{\nu}_e$'s, the low background technology have been developed, and DUNE, which will be able to detect ν_e's, is under construction. More realistic theoretical predictions on neutrinos are, therefore, strongly required to derive more detailed information with the observation of the next galactic SN explosions. We usually calculate the evolutions of massive stars dividing into three stages: the quasi-stationary evolution phase of the progenitors, the SN explosion phase and the PNS cooling phase. In the recent 30 years, the numerical simulations of these phases are developed by many theorists in the techniques of numerical schemes and the input physics individually and we have found some numerical studies got the successful explosions recently. Several problems are still remaining because of the huge calculation costs, however. Moreover, although the results of the numerical simulations in each phase depend on the initial conditions drastically, there is no comprehensive studies so far. We should make a serious effort to draw light curves and spectral evolutions of neutrinos that span the entire period from the progenitor phase up to the formation of the normal neutron star. I hence have tried to solve the remaining problems in each phase for the first step.

First of all, I focus on the "pre-SN neutrinos" released from the center of the progenitors at the first evolutionary stage. It is well known that the energy losses by neutrinos become dominant to those by electronmagnetic waves, and these effects are already taken into the numerical simulations of the stellar evolutions. While SN neutrinos are released with several tens of MeV, however, pre-SN neutrinos are mainly emitted with several MeV. Therefore, it is difficult to distinguish them from the background of detectors, and it has never been focused in the observational point of view so far. However, with the developments of neutrino detectors in recent years, there is a possibility of detecting pre-SN neutrinos from neighborhood ($\sim$ kpc). In this study, I calculate the luminosities and spectra of pre-SN neutrinos emitted from the progenitors with different initial masses for all flavors and examine their detectability. In particular, I focus on the difference between the progenitors of "ONeCCSN" and "FeCCSN". Since it is well known that the evolutions of the

central density and temperature in both progenitors are greatly different at the late phase, I discuss whether they can be discriminated from the observations of pre-SN neutrinos. I employ the results of the latest stellar evolutin model as a background and obtain the evolutions of the neutrino luminosities and spectra. As a result, the neutrino luminosity and average energy of the FeCCSN progenitors gradually increase from several days before the explosion, whereas those from the ONeCCSN progenitors sharply rise from tens of milliseconds before the explosion. Finally, estimating the number of pre-SN neutrinos detected at the terrestrial detectors, the $\bar{\nu}_e$'s from the ONeCCSN prognitor can not be detected by almost all detectors, whereas for the FeCCSN progenitor all detectors can detect pre-SN neutrinos. On the other hand, the number of events of the ν_e's is largely depending on the mass hierarchy of the neutrinos and it is expected to contribute to the determination of the neutrino mass hierarchy.

Secondly, I pay attention to the "SN neutrinos" accompanying the explosion. Although SN explosion occurs when the shock wave formed at the center reaches the stellar surface, it stagnates inside the core because of the matter accretion and the additional heating sources are necessary for the shock to revive. The most promising source is the neutrinos emitted from PNS and they interact with matters behind the shock wave. This is called "neutrino heating mechanism". In this scenario, the energy given to the shock wave is determined by the total number and the average energy of neutrinos emitted inside PNS. Therefore, it is necessary to deal with the emission processes of neutrinos inside PNS and the scattering processes with matters during propagation from the surface of PNS to the shock wave in detail. In the recent numerical studies, the number of energy and angle meshes are not enough to resolve the small energy exchanged by the scatterings with heavy nucleons. However, since there are many nucleons inside the star, the number of scatterings is large and it is necessary to investigate how much the neutrino spectrum is changed by nucleon recoils. In this study, I carry out the steady-state calculations of the neutrino transport from the PNS surface to the region, where neutrino reactions can be neglected, using Monte Carlo method based on the dynamical SN simulation. Then I calculate the change of neutrino spectra due to nucleon recoils and investigate whether it is necessary to incorporate them in the dynamical SN simulations. The effects of nulceon recoils appear in the different way depending on neutrino flavors. For ν_e's and $\bar{\nu}_e$'s, the charged current reactions with nucleons dominate other reactions and the recoil effects do not change the spectra. On the other hand, for ν_x's, which do not cause the charge current reactions, the average energy and the number of neutrinos existing in the calculation domain are reduced by $\sim 15\%$ and $\sim 7\%$, respectively, due to the nucleon recoils. The reduction of neutrino opacities enhances the PNS contraction and increase of temperature, which increase the luminosities of ν_e's and $\bar{\nu}_e$'s and the heating behind the shock wave. I also compare the energy exchanged by nucleon scatterings with that by electron scatterings and find that the former is important for the thermalization of neutrinos for all flavors.

Appendix A

Reaction rates of neutrino emissions

In the following I give detailed derivations of the expressions for the reaction rates of the electro-positron pair annihilation and the plasmon decay in turn.

A.1 Reaction rate of electron-positron pair annihilation

The rate of the reaction, R, to produce a pair of neutrino and anti-neutrino via the annihilation of a pair of electron and positron, which corresponds to the left Feynman diagram in Fig. 1.8 to the lowest order, is given by the low-energy limit of the Weinberg-Salam theory, which is actually identical to the Fermi's theory, as follows:

$$R = \left(\frac{G}{\sqrt{2}}\right)^2 \iint \frac{d^3k}{(2\pi)^3 2E_e} \frac{d^3k'}{(2\pi)^3 2E_e{}'} (2\pi)^4 \delta^4 (q + q' - k - k') f_{e^-}(E_e) f_{e^+}(E'_e) \\ \times 64 \left[(C_V - C_A)^2 (q \cdot k)(q' \cdot k') + (C_V + C_A)^2 (q \cdot k')(q' \cdot k) + m_e \left(C_V^2 - C_A^2\right)(q \cdot q') \right], \tag{A.1}$$

in which $k = (E_e, \boldsymbol{k})$, $k' = (E_e{}', \boldsymbol{k}')$, $q = (E_\nu, \boldsymbol{q})$ and $q' = (E_{\bar{\nu}}, \boldsymbol{q}')$ denote the four momenta of electron, positron, neutrino and anti-neutrino, respectively. Following Schinder and Shapiro (1982); Mezzacappa and Bruenn (1993a), we re-cast the above equation into the following form:

$$R = \frac{8G^2}{(2\pi)^2} [\beta_1 I_1 + \beta_2 I_2 + \beta_3 I_3], \tag{A.2}$$

in which the factors are given as $\beta_1 = (C_V - C_A)^2, \beta_2 = (C_V + C_A)^2, \beta_3 = C_V^2 - C_A^2$ and the integrals are grouped into

$$I_1 = \iint \frac{d^3k}{E_e}\frac{d^3k'}{E_e{}'}\delta^4(q+q'-k-k')\, f_{e^-}(E_e)\, f_{e^+}(E'_e)\,(q\cdot k)^2, \tag{A.3}$$

$$I_2 = \iint \frac{d^3k}{E_e}\frac{d^3k'}{E_e{}'}\delta^4(q+q'-k-k')\, f_{e^-}(E_e)\, f_{e^+}(E'_e)\,(q\cdot k')^2, \tag{A.4}$$

$$I_3 = \iint \frac{d^3k}{E_e}\frac{d^3k'}{E_e{}'}\delta^4(q+q'-k-k')\, f_{e^-}(E_e)\, f_{e^+}(E'_e)\, m_e^2\,(q\cdot q')^2. \tag{A.5}$$

These integrals are evaluated as follows. We begin with I_1. Using three of the four δ-functions we can easily accomplish the integrals over the positron momentum k' to get

$$\begin{aligned}&\int \frac{d^3k'}{E_e{}'} f_{e^+}(E'_e)\,\delta^4(q+q'-k-k') \\ &\quad = 2 f_{e^+}(E_\nu + E_{\bar\nu} - E_e)\,\Theta(E_\nu + E_{\bar\nu} - E_e)\,\delta\left(q+q'-k^2-m_e^2\right),\end{aligned} \tag{A.6}$$

in which the Heaviside function is denoted by Θ. The remaining integrals over the electron momentum k are performed on the spherical coordinates in the momentum space with the volume element written as $d^3k = |\boldsymbol{k}|E_e dE_e d(\cos\theta_e)d\phi_e$. The ϕ_e integral is trivial to give a factor of 2π. The integral over θ_e can be accomplished with the use of the last δ-function. The resultant expression is given as

$$\begin{aligned}I_1 &= \int_{E_{\min}}^{E_{\max}} 2\pi\, dE_e\, f_{e^-}(E_e)\, f_{e^+}(E_\nu + E_{\bar\nu} - E_e) \\ &\quad \times \frac{{E_\nu}^2 {E_{\bar\nu}}^2}{\Delta_e^5}(1-\cos\psi)^2\left[AE_e^2 + BE_e + C\right],\end{aligned} \tag{A.7}$$

in which θ is the angle between $\boldsymbol{q}$ and $\boldsymbol{q}'$ and ${\Delta_e}^2$ is given by

$${\Delta_e}^2 \equiv {E_{\bar\nu}}^2 + {E_\nu}^2 + 2E_\nu E_{\bar\nu}\cos\psi, \tag{A.8}$$

and A, B and C are defined as

$$\begin{cases} A \equiv {E_{\bar\nu}}^2 + {E_\nu}^2 - E_\nu E_{\bar\nu}(3+\cos\psi), \\ B \equiv E_\nu\left[-2{E_\nu}^2 + {E_{\bar\nu}}^2(1+3\cos\psi) + E_\nu E_{\bar\nu}(3-\cos\psi)\right], \\ C \equiv E_\nu^2\left[(E_\nu + E_{\bar\nu}\cos\psi)^2 - \frac{1}{2}{E_{\bar\nu}}^2(1-\cos^2\psi) - \frac{1}{2}\left(\frac{m_e\Delta_e}{E_\nu}\right)^2\frac{1+\cos\psi}{1-\cos\psi}\right] \end{cases} \tag{A.9}$$

The lower and upper limits of the remaining integral with respect to E_e are given as

$$\begin{cases} E_{\min} = \max\left[m_e, \dfrac{E_\nu + E_{\bar\nu}}{2} - \dfrac{\Delta_e}{2}\sqrt{1 - \dfrac{2{m_e}^2}{E_\nu E_{\bar\nu}(1-\cos\psi)}}\,\right], \\ E_{\max} = \min\left[E_\nu + E_{\bar\nu} - m_e, \dfrac{E_\nu + E_{\bar\nu}}{2} + \dfrac{\Delta_e}{2}\sqrt{1 - \dfrac{2{m_e}^2}{E_\nu E_{\bar\nu}(1-\cos\psi)}}\,\right]. \end{cases} \tag{A.10}$$

Finally, we express the integral over the electron energy E_e with the Fermi integral defined as

$$F_n(\eta) = \int_0^\infty \frac{x^n}{e^{x-\eta}+1} dx. \tag{A.11}$$

Using the following relation for the product of the Fermi-Dirac distributions,

$$\begin{aligned} & f_{e^-}(E_e) f_{e^+}(E_\nu + E_{\bar\nu} - E_e) \\ = & \frac{1}{\exp\left(\frac{E_\nu+E_{\bar\nu}}{T}\right)-1} \left\{ \frac{1}{\exp\left(\frac{E_e-(E_\nu+E_{\bar\nu})-\mu_e}{T}\right)+1} - \frac{1}{\exp\left(\frac{E_e-\mu_e}{T}\right)+1} \right\} \end{aligned} \tag{A.12}$$

We can obtain the final expression for I_1 as

$$\begin{aligned} I_1(E_\nu, E_{\bar\nu}, \cos\psi) = & -\frac{2\pi T\, E_\nu^2 {E_{\bar\nu}}^2 (1-\cos\psi)^2}{\left[\exp\left(\frac{E_\nu+E_{\bar\nu}}{T}\right)-1\right] {\Delta_e}^5} \\ & \times \left\{ AT^2 \left([G_2(y_{\max}) - G_2(y_{\min})] \right.\right. \\ & \quad + [2y_{\max} G_1(y_{\max}) - 2y_{\min} G_1(y_{\min})] \\ & \quad \left.\left. + \left[y_{\max}^2 G_0(y_{\max}) - y_{\min}^2 G_0(y_{\min}) \right] \right) \right. \\ & + BT \left([G_1(y_{\max}) - G_1(y_{\min})] + [y_{\max} G_0(y_{\max}) - y_{\min} G_0(y_{\min})] \right) \\ & \left. + C [G_0(y_{\max}) - G_0(y_{\min})] \right\}, \end{aligned} \tag{A.13}$$

with $\eta' = (\mu_e + E_\nu + E_{\bar\nu})/T$, $\eta = \mu_e/T, y_{\max} = E_{\max}/T$, $y_{\min} = E_{\min}/T$ and $G_n(y) \equiv F_n(\eta' - y) - F_n(\eta - y)$.

Similar calculations can be done for the other two integrals to give

$$I_2 = I_1(E_{\bar\nu}, E_\nu, \cos\psi), \tag{A.14}$$

$$I_3 = -\frac{2\pi T m_e^2 E_\nu E_{\bar\nu}(1-\cos\psi)}{\left[\exp(\frac{E_\nu+E_{\bar\nu}}{T})-1\right]\Delta_e} [G_0(y_{\max}) - G_0(y_{\min})]. \tag{A.15}$$

A.2 Reaction rate of plasmon decay

The properties of plasmon are derived from the so-called polarization tensor $\Pi^{\mu\nu}$, which is calculated field-theoretically as

$$\begin{aligned} i\Pi^{\mu\nu}(K) = & \frac{4i}{e^2} \int \frac{d^3k}{2E_e(2\pi)^3} \frac{(k\cdot K)(K^\mu k^\nu + K^\nu k^\mu) - K^2 k^\mu k^\nu - (k\cdot K)^2 g^{\mu\nu}}{(k\cdot K)^2} \\ & \times (f_{e^-}(E_e) + f_{e^+}(E_e)), \end{aligned} \tag{A.16}$$

in which $K = (\omega, \boldsymbol{K})$ and $k = (E_e, \boldsymbol{k})$ are the 4-momenta of plasmon and electron, respectively. It is decomposed into the transverse (Π_T) and longitudinal (Π_L) components, which are expressed as

$$\Pi^{\mu\nu}(K) = \Pi_T(K) P_T^{\mu\nu}(K) + \Pi_L(K) P_L^{\mu\nu}(K), \tag{A.17}$$

where the projection operators $P_T^{\mu\nu}$ and $P_L^{\mu\nu}$ are given as

$$P_T{}^{\mu\nu}(K) = \begin{cases} 0 & (\mu,\nu)=(0,0) \\ 0 & (\mu,\nu)=(0,i) \\ -\delta^{ij}+\dfrac{K^iK^j}{|\boldsymbol{K}|^2} & (\mu,\nu)=(i,j) \end{cases}, \tag{A.18}$$

$$P_L{}^{\mu\nu}(K) = \begin{cases} -\dfrac{|\boldsymbol{K}|^2}{K^2} & (\mu,\nu)=(0,0) \\ -\dfrac{\omega K^i}{K^2} & (\mu,\nu)=(0,i) \\ -\dfrac{(\omega)^2 K^iK^j}{K^2|\boldsymbol{K}|^2} & (\mu,\nu)=(i,j) \end{cases}. \tag{A.19}$$

Using the relations $P_T^{\mu\nu}P_{L\mu\nu}=0$, $P_T^{\mu\nu}P_{T\mu\nu}=2$, $P_L^{\mu\nu}P_{L\mu\nu}=1$ between the projection operators, we obtain each component of the polarization tensor as

$$\begin{aligned} \Pi_T(K) &= \frac{1}{2}\Pi^{\mu\nu}(K)P_{T\mu\nu}(K) \\ &= -\frac{2}{e^2}\int\frac{d^3k}{2E_e\,(2\pi)^3}\frac{-K^2\,|\boldsymbol{k}|^2+\dfrac{K^2}{|\boldsymbol{K}|^2}\,(\boldsymbol{K}\cdot\boldsymbol{k})^2+2\,(k\cdot K)^2}{(k\cdot K)^2} \\ &\quad\times\left(f_{e^-}\,(E_e)+f_{e^+}\,(E_e)\right), \end{aligned} \tag{A.20}$$

$$\begin{aligned} \Pi_L(K) &= -\frac{K^2}{|\boldsymbol{K}|^2}\Pi^{00} \\ &= -\frac{4}{e^2}\frac{K^2}{|\boldsymbol{K}|^2}\int\frac{d^3k}{2E_e\,(2\pi)^3}\frac{-K^2{E_e}^2+2\,(k\cdot K)\,(E_e\,\omega)-(k\cdot K)^2}{(k\cdot K)^2} \\ &\quad\times\left(f_{e^-}\,(E_e)+f_{e^+}\,(E_e)\right). \end{aligned} \tag{A.21}$$

In the relativistic limit, i.e., $E_e \gg |\boldsymbol{K}|, \omega$ and $m_e \to 0$ and $E_e \sim |\boldsymbol{k}|$, which is well justified in the present case, the above expressions are reduced to the following:

$$\Pi_T(K) = -\frac{3}{2}\frac{\omega^2}{e^2\,|\boldsymbol{K}|^2}{\omega_p}^2\left[1-\frac{\omega^2-|\boldsymbol{K}|^2}{\omega^2}\frac{\omega}{2\,|\boldsymbol{K}|}\ln\frac{\omega+|\boldsymbol{K}|}{\omega-|\boldsymbol{K}|}\right], \tag{A.22}$$

$$\Pi_L(K) = -3{\omega_p}^2\frac{\omega^2-|\boldsymbol{K}|^2}{e^2\,|\boldsymbol{K}|^2}\left[\frac{\omega}{2\,|\boldsymbol{K}|}\ln\frac{\omega+|\boldsymbol{K}|}{\omega-|\boldsymbol{K}|}-1\right], \tag{A.23}$$

in which the plasma frequency ω_p is defined as

$${\omega_p}^2 = \frac{2e^2}{3\pi^2}\,(k_BT)^2\,(F_1\,(\eta)+F_1\,(-\eta)). \tag{A.24}$$

The number of the reaction per unit time and volume, R, to produce a pair of neutrino and anti-neutrino via the decay of a plasmon is given by the polarization

tensor $\Pi^{\mu\nu}$ as follows:

$$\begin{aligned}
R &= \left(\frac{G}{\sqrt{2}}\right)^2 8\left(q_\mu {q_\nu}' + q_\nu {q_\mu}' - g_{\mu\nu} q\cdot q'\right) 2\pi {C_v}^2 K^2 \left[\Theta(\omega)\left(1+f_B(\omega)\right) + \Theta(-\omega) f_B(-\omega)\right] \\
&\qquad \times \left\{\Pi_L(K) P_L^{\mu\nu} \delta\left(K^2 + e^2\Pi_L(K)\right) + \Pi_T(K) P_T^{\mu\nu}\delta\left(K^2 + e^2\Pi_T(K)\right)\right\} \\
&= \left(\frac{G}{\sqrt{2}}\right)^2 \frac{8K^2}{\left[1-\exp\left(-\frac{\omega}{k_B T}\right)\right]} \left[\Theta(\omega) - \Theta(-\omega)\right]\left(q_\mu q'_\nu + q_\nu q'_\mu - g_{\mu\nu} q\cdot q'\right) \\
&\quad \times \left\{ -\frac{3}{2}\frac{\omega^2}{e^2 |\boldsymbol{K}|^2} {\omega_p}^2 \left[1 - \frac{\omega^2 - |\boldsymbol{K}|^2}{\omega^2}\frac{\omega}{2|\boldsymbol{K}|}\ln\frac{\omega+|\boldsymbol{K}|}{\omega-|\boldsymbol{K}|}\right] P_T^{\mu\nu}\delta\left(K^2 + e^2\Pi_T(K)\right)\right. \\
&\qquad \left. -3{\omega_p}^2 \frac{\omega^2 - |\boldsymbol{K}|^2}{e^2|\boldsymbol{K}|^2}\left[\frac{\omega}{2|\boldsymbol{K}|}\ln\frac{\omega+|\boldsymbol{K}|}{\omega-|\boldsymbol{K}|} - 1\right] P_L^{\mu\nu}\delta\left(K^2 + e^2\Pi_L(K)\right)\right\}. \qquad \text{(A.25)}
\end{aligned}$$

Note that the dispersion relations for the transverse and longitudinal plasmons are obtained from the δ-functions as $\omega = \omega_T(\boldsymbol{K})$ and $\omega = \omega_L(\boldsymbol{K})$, which satisfy the following equations:

$$K^2 + e^2\Pi_T(K) = K^2 - \frac{3}{2}{\omega_p}^2 \frac{{\omega_T}^2}{|\boldsymbol{K}|^2}\left[1 - \frac{{\omega_T}^2 - |\boldsymbol{K}|^2}{{\omega_T}^2}\frac{\omega_T}{2|\boldsymbol{K}|}\ln\frac{\omega_T+|\boldsymbol{K}|}{\omega_T-|\boldsymbol{K}|}\right] = 0, \quad \text{(A.26)}$$

$$K^2 + e^2\Pi_L(K) = K^2 - 3{\omega_p}^2\frac{K^2}{|\boldsymbol{K}|^2}\left[\frac{\omega_L}{2|\boldsymbol{K}|}\ln\frac{\omega_L+|\boldsymbol{K}|}{\omega_L-|\boldsymbol{K}|} - 1\right] = 0. \qquad \text{(A.27)}$$

Employing the conservation law $K = -(q+q')$, we finally obtain the reaction rate R as a function of $E_\nu, E_{\bar\nu}, \cos\psi$ as follows:

$$\begin{aligned}
R &= \left(\frac{G}{\sqrt{2}}\right)^2 \frac{16{C_V}^2}{e^2}\frac{2{E_\nu}^2{E_{\bar\nu}}^2(1-\cos\psi)}{\left[1-\exp\left(\frac{E_\nu+E_{\bar\nu}}{k_B T}\right)\right]} \\
&\quad \times \left\{\frac{3{\omega_p}^2}{{\Delta_e}^2}\delta\left(f_L\left(E_\nu, E_{\bar\nu}, \cos\psi\right)\right)\left[\frac{E_\nu+E_{\bar\nu}}{2\Delta_e}\ln\frac{E_\nu+E_{\bar\nu}-\Delta_e}{E_\nu+E_{\bar\nu}+\Delta_e} + 1\right]\right. \\
&\qquad \times \left[-2\cos\psi\left(E_\nu+E_{\bar\nu}\right)^2 - 2E_\nu E_{\bar\nu}\sin^2\psi + \frac{2\left(E_\nu+E_{\bar\nu}\right)^2}{{\Delta_e}^2}\left(E_\nu + E_{\bar\nu}\cos\psi\right)\left(E_{\bar\nu} + E_\nu\cos\psi\right)\right] \\
&\quad -\frac{3{\omega_p}^2\left(E_\nu+E_{\bar\nu}\right)^2}{{\Delta_e}^2}\delta\left(f_T\left(E_\nu, E_{\bar\nu}, \cos\psi\right)\right)\left[1 + \frac{E_\nu E_{\bar\nu}(1-\cos\psi)}{\left(E_\nu+E_{\bar\nu}\right)\Delta_e}\ln\frac{E_\nu+E_{\bar\nu}-\Delta_e}{E_\nu+E_{\bar\nu}+\Delta_e}\right] \\
&\qquad \left.\times\left[1 - \frac{\left(E_\nu\cos\psi + E_{\bar\nu}\right)\left(E_{\bar\nu}\cos\psi + E_\nu\right)}{{\Delta_e}^2}\right]\right\}, \qquad \text{(A.28)}
\end{aligned}$$

with $f_L\left(E_\nu, E_{\bar\nu}, \cos\psi\right)$ and $f_T\left(E_\nu, E_{\bar\nu}, \cos\psi\right)$ given as

$$\begin{aligned}
f_L\left(E_\nu, E_{\bar\nu}, \cos\psi\right) &= 2E_\nu E_{\bar\nu}(1-\cos\psi) \\
&\quad +3{\omega_p}^2\frac{2E_\nu E_{\bar\nu}(1-\cos\psi)}{{\Delta_e}^2}\left\{\frac{E_\nu+E_{\bar\nu}}{2\Delta_\nu}\ln\frac{E_\nu+E_{\bar\nu}-\Delta_e}{E_\nu+E_{\bar\nu}+\Delta_e} + 1\right\}, \qquad \text{(A.29)} \\
f_T\left(E_\nu, E_{\bar\nu}, \cos\psi\right) &= 2E_\nu E_{\bar\nu}(1-\cos\psi) \\
&\quad -\frac{3}{2}{\omega_p}^2\frac{\left(E_\nu+E_{\bar\nu}\right)^2}{{\Delta_e}^2}\left[1 + \frac{E_\nu E_{\bar\nu}(1-\cos\psi)}{\left(E_\nu+E_{\bar\nu}\right)\Delta_e}\ln\frac{E_\nu+E_{\bar\nu}-\Delta_e}{E_\nu+E_{\bar\nu}+\Delta_e}\right]. \qquad \text{(A.30)}
\end{aligned}$$

Appendix B

Determination of neutrino energy after scattering

In my code, I incorporate the reaction tables for nucleon- and electron-neutrino scatterings. In order to ensure the detailed balance between neutrinos before and after scattering E_ν, E'_ν, I adopt the special manner to determine the neutrino energy after scattering.

1. $E_{\rm min} \leq E'_\nu \leq E_\nu$
   The reaction rates for $E_\nu \leq E'_\nu$ are included in the table and I get neutrino energy after scattering interpolating data in the table. I use the modified reaction rate $\tilde{R}$ instead of $R_{\rm Nrec}$ for convenience:

$$\tilde{R}\left(E_\nu, \Delta E\right) = R_{\rm Nrec}\left(E_\nu, E'_\nu\right) \exp\left(-\frac{E_\nu}{T}\right), \tag{B.1}$$

   with the energy differecne $\Delta E \equiv E'_\nu - E_\nu$. The modified reaction rates are described by the reaction rates in the table $\tilde{R}_{ij} \equiv \tilde{R}\left(E_i, \Delta E_{ij}\right)$ with the neutrino energy employed in the table $E_1 \leq E_\nu \leq E_2$ and $E'_1 \leq E'_\nu \leq E'_2$ and the energy difference $\Delta E_{ij} \equiv E'_j - E_i$:

$$\tilde{R}\left(E_\nu, \Delta E\right) = q_1 k_1 \tilde{R}_{11} + q_1 k_2 \tilde{R}_{12} + q_2 k'_1 \tilde{R}_{21} + q_2 k'_2 \tilde{R}_{22}, \tag{B.2}$$

   where the coefficients are defined as follows:

$$q_1 = \frac{E_2 - E_\nu}{E_2 - E_1}, \quad q_2 = \frac{E_\nu - E_1}{E_2 - E_1} \tag{B.3}$$

$$k_1 = \frac{\Delta E_{12} - \Delta E}{\Delta E_{12} - \Delta E_{11}}, \quad k_2 = \frac{\Delta E - \Delta E_{11}}{\Delta E_{12} - \Delta E_{11}}, \tag{B.4}$$

$$k'_1 = \frac{\Delta E_{22} - \Delta E}{\Delta E_{22} - \Delta E_{21}}, \quad k'_2 = \frac{\Delta E - \Delta E_{21}}{\Delta E_{22} - \Delta E_{21}}. \tag{B.5}$$

2. $E_\nu \leq E'_\nu \leq E_{\rm max}$
   The reaction rates for $E_\nu \geq E'_\nu$ are derived from the rates for $E_\nu \leq E'_\nu$ using the following relation:

$$\tilde{R}\left(E_\nu, E'_\nu\right) = \tilde{R}\left(E'_\nu, E_\nu\right), \tag{B.6}$$

based on the detailed balance. The modified reaction rate is described as

$$\tilde{R}\left(E'_\nu, E_\nu\right) = q_3 k_3 \tilde{R}_{33} + q_3 k_4 \tilde{R}_{34} + q_4 k'_3 \tilde{R}_{43} + q_4 k'_4 \tilde{R}_{44}. \tag{B.7}$$

with the neutrino energy employed in the table $E_3 \leq E'_\nu E_4$ and $E'_3 \leq E_\nu E'_4$, the energy difference $\Delta E' \equiv E_\nu - E'_\nu$ and the coefficients

$$q_3 = \frac{E_4 - E'_\nu}{E_4 - E_3}, \quad q_4 = \frac{E'_\nu - E_3}{E_4 - E_3}, \tag{B.8}$$

$$k_3 = \frac{\Delta E_{34} - \Delta E'}{\Delta E_{34} - \Delta E_{33}}, \quad k_4 = \frac{\Delta E' - \Delta E_{33}}{\Delta E_{34} - \Delta E_{33}}, \tag{B.9}$$

$$k'_3 = \frac{\Delta E_{44} - \Delta E'}{\Delta E_{44} - \Delta E_{43}}, \quad k'_4 = \frac{\Delta E' - \Delta E_{43}}{\Delta E_{44} - \Delta E_{43}} \tag{B.10}$$

The total rate integrated over E'_ν is

$$\begin{aligned}
A &\equiv \int_{E_{\min}}^{E_{\max}} R\left(E_\nu, \tilde{E}_\nu\right) 2\pi \tilde{E}_\nu^2 d\tilde{E}_\nu \\
&= \int_{E_{\min}}^{E_{\max}} \tilde{R}\left(E_\nu, \tilde{E}_\nu\right) \exp\left(\frac{E_\nu}{T}\right) 2\pi \tilde{E}_\nu^2 d\tilde{E}_\nu \\
&= 2\pi \exp\left(\frac{E_\nu}{T}\right) \left[\int_{E_{\min}}^{E_\nu} \tilde{R}\left(E_\nu, \tilde{E}_\nu\right) \tilde{E}_\nu^2 d\tilde{E}_\nu + \int_{E_\nu}^{E_{\max}} \tilde{R}\left(\tilde{E}_\nu, E_\nu\right) \tilde{E}_\nu^2 d\tilde{E}_\nu\right] \\
&= \frac{1}{4}\left(E_\nu^4 - E_{\min}^4\right) A_{11} + \frac{1}{3}\left(E_\nu^3 - E_{\min}^3\right) A_{12} \\
&\quad + \frac{1}{5}\left(E_{\max}^5 - E_\nu^5\right) B_{11} + \frac{1}{4}\left(E_{\max}^4 - E_\nu^4\right) B_{12} + \frac{1}{3}\left(E_{\max}^3 - E_\nu^3\right) B_{13}
\end{aligned} \tag{B.11}$$

with the minimum and maximum energies $E_{\min}, E_{\max}$, at which the reaction rates become 10^{-5} times less than the peak rate, and the coefficients:

$$A_{11} = \frac{-\tilde{R}_{11} + \tilde{R}_{12}}{\Delta E_{12} - \Delta E_{11}} q_1 + \frac{-\tilde{R}_{21} + \tilde{R}_{22}}{\Delta E_{22} - \Delta E_{21}} q_2, \tag{B.12}$$

$$\begin{aligned}
A_{12} &= \frac{\left(\Delta E_{12} + E_\nu\right) \tilde{R}_{11} - \left(\Delta E_{11} + E_\nu\right) \tilde{R}_{12}}{\Delta E_{12} - \Delta E_{11}} q_1 \\
&\quad + \frac{\left(\Delta E_{22} + E_\nu\right) \tilde{R}_{21} - \left(\Delta E_{21} + E_\nu\right) \tilde{R}_{22}}{\Delta E_{22} - \Delta E_{21}} q_2,
\end{aligned} \tag{B.13}$$

$$B_{11} = \frac{1}{E_4 - E_3}\left(-\frac{\tilde{R}_{33} + \tilde{R}_{34}}{\Delta E_{34} - \Delta E_{33}} + \frac{\tilde{R}_{43} - \tilde{R}_{44}}{\Delta E_{44} - \Delta E_{43}}\right), \tag{B.14}$$

$$\begin{aligned}
B_{12} &= \frac{1}{E_4 - E_3}\left(\frac{\tilde{R}_{33}\left(E_4 - \Delta E_{34} + E_\nu\right) - \tilde{R}_{34}\left(E_4 - \Delta E_{33} + E_\nu\right)}{\Delta E_{34} - \Delta E_{33}}\right. \\
&\quad \left. + \frac{\tilde{R}_{43}\left(\Delta E_{44} - E_\nu - E_3\right) - \tilde{R}_{44}\left(\Delta E_{43} - E_\nu - E_3\right)}{\Delta E_{44} - \Delta E_{43}}\right),
\end{aligned} \tag{B.15}$$

$$\begin{aligned}
B_{13} &= \frac{1}{E_4 - E_3}\left(\frac{\tilde{R}_{33} E_4\left(\Delta E_{34} - E_\nu\right) + \tilde{R}_{34} E_4\left(E_\nu - \Delta E_{33}\right)}{\Delta E_{34} - \Delta E_{33}}\right. \\
&\quad \left. + \frac{\tilde{R}_{43} E_3\left(E_\nu - \Delta E_{44}\right) + \tilde{R}_{44} E_3\left(\Delta E_{43} - E_\nu\right)}{\Delta E_{44} - \Delta E_{43}}\right).
\end{aligned} \tag{B.16}$$

The neutrino energy after scattering E'_ν is determined by the random number x in the range of [0,1] and the normalized spectrum $\int_{E_{\min}}^{E'_\nu} R\left(E_\nu, \tilde{E}_\nu\right) 2\pi \tilde{E}_\nu^2 d\tilde{E}_\nu / A$.

Acknowlegments

I am greatful to my supervisor Prof. Shoichi Yamada with many discussions and his useful advices for my research topics. He taught me not only physics but also necessary abilities for researchers such as how to manage own research with many colaborators and how to write papers. He steered me in the right direction. I think it is the best way of repaying his kindness to continue to do my best for my researches from now on.

I am also happy to acknowlege helpful exchanges with my colaborators: Koh Takahashi, Takashi Yoshida, Hideyuki Umeda, Koji Ishidoshiro, Shun Furusawa and Hiroki Nagakura. Koh Takahashi, Takashi Yoshida and Hideyuki Umeda gave me the realistic progenitor models of stellar evolutions and Koji Ishidoshiro gave me useful suggestions about neutrino observations of pre-SN neutrinos. And I discussed with Shun Furusawa about neutrino emissions from nuclear weak interactions in the studies of pre-SN neutrinos. Hiroki Nagakura gave me several results of the dynamical SN simulations for SN neutrino studies and discussed about the neutrino transport using Monte Carlo code many times. I never advanced my researches without their helps.

I appreciate my colleagues in Yamada laboratory for giving me a new slant on my research and the latest astrophysical studies through the discussions in seminars. They also encouraged me greatly spiritually.

Finally, I thank all my family and friends for all their support in my daily life.

Bibliography

Abbott, B. P. et al.: 2016, *Phys. Rev. Lett.* **116(6)**, 061102

Abe, K. et al.: 2014a, *Nucl. Instrum. Meth.* **A737**, 253

Abe, K. et al.: 2014b, *Phys. Rev. Lett.* **112(18)**, 181801

Abe, K. et al.: 2018

Acciarri, R. et al.: 2016

Akimov, D. et al.: 2017, *Science* **357(6356)**, 1123

Alimonti, G. et al.: 2009, *Nucl. Instrum. Meth.* **A600**, 568

An, F. et al.: 2016, *J. Phys.* **G43(3)**, 030401

Arnett, D.: 1996, *Supernovae and nucleosynthesis: An investigation of the history of matter, from the big bang to the present*

Asakura, K. et al.: 2016, *Astrophys. J.* **818(1)**, 91

Ashie, Y. et al.: 2005, *Phys. Rev.* **D71**, 112005

Audi, G., M., W., A. H., W., F. G., K., MacCormick, M., Xu, X., and Pfeiffer, B.: 2012, *Chinese Physics C* **36**, 002

Barger, V., Marfatia, D., and Whisnant, K.: 2003, *Int. J. Mod. Phys.* **E12**, 569

Beacom, J. F. and Vagins, M. R.: 2004, *Phys. Rev. Lett.* **93**, 171101

Berger, B. E. et al.: 2009, *JINST* **4**, P04017

Bollig, R., Janka, H. T., Lohs, A., Martinez-Pinedo, G., Horowitz, C. J., and Melson, T.: 2017, *Phys. Rev. Lett.* **119(24)**, 242702

Braaten, E. and Segel, D.: 1993, *Phys. Rev.* **D48**, 1478

Bruenn, S. W.: 1985, *The Astrophysical Journal Supplement Series* **58**, 771

Burrows, A., Livne, E., Dessart, L., Ott, C., and Murphy, J.: 2006, *Astrophys. J.* **640**, 878

Buyukcizmeci, N. et al.: 2013, *Nucl. Phys.* **A907**, 13

Castor, J. I.: 2004, *Radiation Hydrodynamics*

Chakraborty, S. and Mirizzi, A.: 2014, *Phys. Rev.* **D90(3)**, 033004

Dessart, L., Burrows, A., Livne, E., and Ott, C. D.: 2006, *Astrophys. J.* **645**, 534

Doherty, C. L., Gil-Pons, P., Siess, L., and Lattanzio, J. C.: 2017, *Publications of the Astronomical Society of Australia* **34**, e056

Duan, H., Fuller, G. M., Carlson, J., and Qian, Y.-Z.: 2006a, *Phys. Rev. Lett.* **97**, 241101

Duan, H., Fuller, G. M., Carlson, J., and Qian, Y.-Z.: 2006b, *Phys. Rev.* **D74**, 105014

Esteban-Pretel, A., Pastor, S., Tomas, R., Raffelt, G. G., and Sigl, G.: 2007, *Phys. Rev.* **D76**, 125018

Fischer, T., Martínez-Pinedo, G., Hempel, M., and Liebendörfer, M.: 2012, *Physical Review D* **85**, 083003

Friman, B. L. and Maxwell, O. V.: 1979, *The Astrophysical Journal* **232**, 541

Fuller, G. M., Fowler, W. A., and Newman, M. J.: 1985, *The Astrophysical Journal* **293**, 1

Furusawa, S., Nagakura, H., Sumiyoshi, K., Kato, C., and Yamada, S.: 2017a, *Phys. Rev.* **C95(2)**, 025809

Furusawa, S., Sumiyoshi, K., Yamada, S., and Suzuki, H.: 2013, *Astrophys. J.* **772**, 95

Furusawa, S., Sumiyoshi, K., Yamada, S., and Suzuki, H.: 2017b, *Nucl. Phys.* **A957**, 188

Furusawa, S., Yamada, S., Sumiyoshi, K., and Suzuki, H.: 2011, *Astrophys. J.* **738**, 178

Guo, G. and Qian, Y.-Z.: 2016, *Phys. Rev.* **D94(4)**, 043005

Haft, M., Raffelt, G., and Weiss, A.: 1994, *The Astrophysical Journal* **425**, 222

Hirata, K., Kajita, T., Koshiba, M., Nakahata, M., Oyama, Y., Sato, N., Suzuki, A., Takita, M., Totsuka, Y., Kifune, T., Suda, T., Takahashi, K., Tanimori, T., Miyano, K., Yamada, M., Beier, E. W., Feldscher, L. R., Kim, S. B., Mann, A. K., Newcomer, F. M., van, R., Zhang, W., and Cortez, B. G.: 1987, *Physical Review Letters* **58**, 1490

Horowitz, C. J.: 2002, *Phys. Rev.* **D65**, 043001

Horowitz, C. J. and Li, G.: 1999, *Phys. Rev. Lett.* **82**, 5198

Itoh, N., Hayashi, H., Nishikawa, A., and Kohyama, Y.: 1996, *The Astrophysical Journal Supplement Series* **102**, 411

Iwakami, W., Kotake, K., Ohnishi, N., Yamada, S., and Sawada, K.: 2007, *Astrophys. J.*, [Astrophys. J.678,1207(2008)]

Jones, S. et al.: 2013, *Astrophys. J.* **772**, 150

Juodagalvis, A., Langanke, K., Hix, W. R., Martinez-Pinedo, G., and Sampaio, J. M.: 2010, *Nucl. Phys.* **A848**, 454

Juodagalvis, A., Sampaio, J. M., Langanke, K., and Hix, W. R.: 2008, *Journal of Physics G Nuclear Physics* **35(1)**, 014031

Kasen, D., Thomas, R. C., and Nugent, P.: 2006, *Astrophys. J.* **651**, 366

Kato, C., Delfan Azari, M., Yamada, S., Takahashi, K., Umeda, H., Yoshida, T., and Ishidoshiro, K.: 2015, *The Astrophysical Journal* **808**, 168

Keil, M. T., Raffelt, G. G., and Janka, H.-T.: 2003, *Astrophys. J.* **590**, 971

Kitaura, F. S., Janka, H. T., and Hillebrandt, W.: 2006, *Astronomy & Astrophysics* **450**, 345

Kotake, K., Takiwaki, T., Fischer, T., Nakamura, K., and Martínez-Pinedo, G.: 2018, *The Astrophysical Journal* **853**, 170

Koura, H.: 2004, in M. Arnould, M. Lewitowicz, G. Münzenberg, H. Akimune, M. Ohta, H. Utsunomiya, T. Wada, and T. Yamagata (eds.), *Tours Symposium on Nuclear Physics V*, Vol. 704 of *American Institute of Physics Conference Series*, pp 60–72

Koura, H., Tachibana, T., Uno, M., and Yamada, M.: 2003, *RIKEN accelerator progress report* **36**, 9

Koura, H., Tachibana, T., Uno, M., and Yamada, M.: 2005, *Progress of Theoretical Physics* **113(2)**, 305

Kraus, C. and Peeters, S. J. M.: 2010, *Progress in Particle and Nuclear Physics* **64**, 273

Kunugise, T. and Iwamoto, K.: 2007, *Publications of the Astronomical Society of Japan* **59(6)**, L57

Kurganov, A. and Tadmor, E.: 2000, *Journal of Computational Physics* **160**, 241

Langanke, K. and Martínez-Pinedo, G.: 2001, *Atomic Data and Nuclear Data Tables* **79**, 1

Langanke, K., Martinez-Pinedo, G., and Sampaio, J. M.: 2001, *Phys. Rev.* **C64**, 055801

Langanke, K., Martinez-Pinedo, G., Sampaio, J. M., Dean, D. J., Hix, W. R., Messer, O. E. B., Mezzacappa, A., Liebendoerfer, M., Janka, H. T., and Rampp, M.: 2003, *Phys. Rev. Lett.* **90**, 241102

Liebendörfer, M., Messer, O. E. B., Mezzacappa, A., Bruenn, S. W., Cardall, C. Y., and Thielemann, F. K.: 2004, *The Astrophysical Journal Supplement Series* **150**, 263

Lucy, L. B.: 1999a, *Astronomy & Astrophysics* **344**, 282

Lucy, L. B.: 1999b, *Astronomy & Astrophysics* **345**, 211

Lucy, L. B.: 2003, *Astron. Astrophys.* **403**, 261

Maeda, K.: 2006, *Astrophys. J.* **644**, 385

Marek, A., Janka, H. T., and M

Maxwell, O. V.: 1987, *The Astrophysical Journal* **316**, 691

Melson, T., Janka, H.-T., Bollig, R., Hanke, F., Marek, A., and Mller, B.: 2015, *Astrophys. J.* **808(2)**, L42

Mezzacappa, A. and Bruenn, S. W.: 1993a, *The Astrophysical Journal* **405**, 669

Mezzacappa, A. and Bruenn, S. W.: 1993b, *The Astrophysical Journal* **410**, 740

Mirizzi, A., Tamborra, I., Janka, H.-T., Saviano, N., Scholberg, K., Bollig, R., Hudepohl, L., and Chakraborty, S.: 2016, *Riv. Nuovo Cim.* **39(1-2)**, 1

Misch, G. W. and Fuller, G. M.: 2016, *Physical Review C* **94**, 055808

Müller, B. and Janka, H.-T.: 2014, *Astrophys. J.* **788**, 82

Müller, B., Janka, H.-T., and Marek, A.: 2013, *Astrophys. J.* **766**, 43

Nagakura, H., Ito, H., Kiuchi, K., and Yamada, S.: 2011, *The Astrophysical Journal* **731**, 80

Nagakura, H., Iwakami, W., Furusawa, S., Okawa, H., Harada, A., Sumiyoshi, K., Yamada, S., Matsufuru, H., and Imakura, A.: 2018, *Astrophys. J.* **854(2)**, 136

Nagakura, H., Iwakami, W., Furusawa, S., Sumiyoshi, K., Yamada, S., Matsufuru, H., and Imakura, A.: 2017, *Astrophys. J. Suppl.* **229(2)**, 42

Nagakura, H., Sumiyoshi, K., and Yamada, S.: 2014, *Astrophys. J. Suppl.* **214(2)**, 16

Nagakura, H. and Yamada, S.: 2008, *Astrophys. J.* **689**, 391

Nakazato, K., Sumiyoshi, K., Suzuki, H., Totani, T., Umeda, H., and Yamada, S.: 2013, *Astrophys. J. Suppl.* **205**, 2

Nomoto, K., Sparks, W. M., Fesen, R. A., Gull, T. R., Miyaji, S., and Sugimoto, D.: 1982, *Nature* **299**, 803

Obergaulinger, M., Cerda-Duran, P., Muller, E., and Aloy, M. A.: 2009, *Astron. Astrophys.* **498**, 241

O'Connor, E. P. and Couch, S. M.: 2018, *Astrophys. J.* **854(1)**, 63

Oda, T., Hino, M., Muto, K., Takahara, M., and Sato, K.: 1994, *Atomic Data and Nuclear Data Tables* **56**, 231

Odrzywołek, A.: 2007, *European Physical Journal C* **52**, 425

Odrzywolek, A.: 2009, *Physical Review C* **80**, 045801

Odrzywolek, A., Misiaszek, M., and Kutschera, M.: 2004, *Astroparticle Physics* **21**, 303

Olive, K. A., P.: 2014, *Chinese Physics C* **38(9)**, 090001

Patton, K. M., Lunardini, C., and Farmer, R. J.: 2017, *Astrophys. J.* **840(1)**, 2

Raduta, A. R., Gulminelli, F., and Oertel, M.: 2017, *Phys. Rev.* **C95(2)**, 025805

Raffelt, G.: 2012, *arXiv e-prints* p. arXiv:1201.1637

Raffelt, G. G.: 2001, *Astrophys. J.* **561**, 890

Ravenhall, D. G., Pethick, C. J., and Wilson, J. R.: 1983, *Phys. Rev. Lett.* **50**, 2066

Sato, K. and Suzuki, H.: 1987, *Phys. Rev. Lett.* **58**, 2722

Sawyer, R. F.: 2016, *Phys. Rev. Lett.* **116(8)**, 081101

Schinder, P. J. and Shapiro, S. L.: 1982, *The Astrophysical Journal Supplement Series* **50**, 23

Scholberg, K.: 2000, *AIP Conf. Proc.* **523(1)**, 355

Scholberg, K.: 2018, *J. Phys.* **G45(1)**, 014002

Sekiya, H.: 2017, *J. Phys. Conf. Ser.* **888(1)**, 012041

Shen, H., Toki, H., Oyamatsu, K., and Sumiyoshi, K.: 2011, *Astrophys. J. Suppl.* **197**, 20

Skinner, M. A., Burrows, A., and Dolence, J. C.: 2015

Smy, M. B. et al.: 2004, *Phys. Rev.* **D69**, 011104

SNOwGLOBES(ver1.1), http://www.phy.duke.edu/s̃chol/snowglobes/

Sullivan, C., O'Connor, E., Zegers, R. G. T., Grubb, T., and Austin, S. M.: 2016, *Astrophys. J.* **816(1)**, 44

Sumiyoshi, K., Suzuki, H., Yamada, S., and Toki, H.: 2004, *Nucl. Phys.* **A730**, 227

Sumiyoshi, K. and Yamada, S.: 2012, *Astrophys. J. Suppl.* **199**, 17

Sumiyoshi, K., Yamada, S., Suzuki, H., Shen, H., Chiba, S., and Toki, H.: 2005, *Astrophys. J.* **629**, 922

Summa, A., Hanke, F., Janka, H.-T., Melson, T., Marek, A., and Mller, B.: 2016, *Astrophys. J.* **825(1)**, 6

Tachibana, T.: 2000, *RIKEN Review: Focused on Models and Theories of the Nuclear Mass* **26**, 109

Tachibana, T. and Yamada, M.: 1995, in *Proceedings, International Conference on Exotic Nuclei & Atomic Masses (ENAM-95): Arles, France, Jun 19-23, 1995*, Vol. 763

Takahashi, K., Sumiyoshi, K., Yamada, S., Umeda, H., and Yoshida, T.: 2018, *arXiv e-prints* p. arXiv:1812.07175

Takahashi, K., Yoshida, T., and Umeda, H.: 2013, *Astrophys. J.* **771**, 28

Takahashi, K., Yoshida, T., Umeda, H., Sumiyoshi, K., and Yamada, S.: 2016, *Monthly Notices of the Royal Astronomical Society* **456**, 1320

Takiwaki, T., Kotake, K., and Suwa, Y.: 2016, *Mon. Not. Roy. Astron. Soc.* **461(1)**, L112

Tamborra, I., Hanke, F., Mller, B., Janka, H.-T., and Raffelt, G.: 2013, *Phys. Rev. Lett.* **111(12)**, 121104

Thompson, T. A., Burrows, A., and Horvath, J. E.: 2000, *Physical Review C* **62**, 035802

Thompson, T. A., Burrows, A., and Pinto, P. A.: 2003, *The Astrophysical Journal* **592**, 434

Tominaga, N., Blinnikov, S. I., and Nomoto, K.: 2013, *The Astrophysical Journal* **771**, L12

Tubbs, D. L.: 1978, *The Astrophysical Journal Supplement Series* **37**, 287

Ugliano, M., Janka, H. T., Marek, A., and Arcones, A.: 2016, *Astrophys. J.* **821**, 69, [Astrophys. J.757,69(2012)]

Umeda, H., Yoshida, T., and Takahashi, K.: 2012, *Progress of Theoretical and Experimental Physics* **2012**, 01A302

Wallace, J., Burrows, A., and Dolence, J. C.: 2016, *Astrophys. J.* **817(2)**, 182

Wright, W. P., Gilmer, M. S., Frhlich, C., and Kneller, J. P.: 2017a, *Phys. Rev.* **D96(10)**, 103008

Wright, W. P., Kneller, J. P., Ohlmann, S. T., Roepke, F. K., Scholberg, K., and Seitenzahl, I. R.: 2017b, *Phys. Rev.* **D95(4)**, 043006

Wright, W. P., Nagaraj, G., Kneller, J. P., Scholberg, K., and Seitenzahl, I. R.: 2016, *Phys. Rev.* **D94(2)**, 025026

Wurm, M. et al.: 2012, *Astropart. Phys.* **35**, 685

Yamasaki, T. and Yamada, S.: 2006, *Astrophys. J.* **650**, 291

Yang, G.: 2015, in *Proceedings, 12th Conference on the Intersections of Particle and Nuclear Physics (CIPANP 2015): Vail, Colorado, USA, May 19-24, 2015*

Yoshida, T. and Tachibana, T.: 2000, *Journal of Nuclear Science and Technology* **37(6)**, 491

Yoshida, T., Takahashi, K., Umeda, H., and Ishidoshiro, K.: 2016, *Phys. Rev.* **D93(12)**, 123012

早稲田大学　博士（理学）　学位申請　研究業績書

（2019 年 2 月　現在）

種 類 別	題名、　発表・発行掲載誌名、　発表・発行年月、　連名者（申請者含む）
論文	○Title: Neutrino emissions in all flavors up to the pre-bounce of massive stars and the possibility of their detections Journal: The Astrophysical Journal, Volume 848, article id. 48, 17 pp. Publication date: October, 2017 Authors: Chinami Kato, Hiroki Nagakura, Shun Furusawa, Koh Takahashi, Hideyuki Umeda, Takashi Yoshida, Koji Ishidoshiro & Shoichi Yamada Title: Dependence of weak interaction rates on the nuclear composition during stellar core collapse Journal: Physical review C, Volume 95, article id. 025809, 11 pp. Publication date: February, 2017 Authors: Shun Furusawa, Hiroki Nagakura, Kohsuke Sumiyoshi, Chinami Kato & Shoichi Yamada ○Title: Pre-supernova neutrino emissions from ONe cores in the progenitors of core-collapse supernovae: are they distinguishable from those of Fe cores? Journal: The Astrophysical Journal, Volume 808, article id. 168, 20 pp. Publication date: July, 2015 Authors: Chinami Kato, Milad Delfan Azari, Shoichi Yamada, Koh Takahashi, Hideyuki Umeda, Takashi Yoshida & Koji Ishidoshiro
講演 （口頭）	Title: ニュートリノ球内部における核子散乱によるニュートリノスペクトルへの影響 Conference: 日本天文学会　2018 年秋季年会 / Date: September, 2018 Authors: Chinami Kato, Hiroki Nagakura, Yusuke Hori & Shoichi Yamada Title: 原子核による前兆ニュートリノ放出 Conference: 新学術「宇宙の歴史をひもとく地下素粒子原子核研究」第三回超新星ニュートリノ研究 / Date: March, 2017 Authors: Chinami Kato Title: 超新星爆発へ向けた親星からの予兆～前兆ニュートリノの放出と観測可能性 Conference: マルチメッセンジャー研究会 / Date: March, 2017 Authors: Chinami Kato Title: 原子核による前兆ニュートリノ放出 Conference: 日本天文学会　2017 年春季年会 / Date: March, 2017 Authors: Chinami Kato, Shoichi Yamada, Hiroki Nagakura, Shun Furusawa, Koh Takahashi, Takashi Yoshida, Hideyuki Umeda & Koji Ishidoshiro Title: Properties of pre-supernova neutrino in collapsing phase～towards comprehensive neutrino studies Conference: Revealing the history of the universe with underground particle and nuclear research 2016 / Date: May, 2016 Authors: Chinami Kato

早稲田大学　博士（理学）　学位申請　研究業績書

種 類 別	題名、　発表・発行掲載誌名、　発表・発行年月、　連名者（申請者含む）
講演 （ポスター）	Title: 前兆ニュートリノの親星依存性 Conference: 日本天文学会　2016 年春季年会 / Date: March, 2016 Authors: Chinami Kato, Shoichi Yamada, Hiroki Nagakura, Koh Takahashi, Takashi Yoshida, Hideyuki Umeda & Koji Ishidoshiro Title: Pre-supernova neutrino emission from ONe cores in the progenitors of core-collapse supernovae: are they distinguishable from those of Fe cores? Conference: Numazu workshop Date: September, 2015 Authors: Chinami Kato Title: 超新星前兆ニュートリノの放出率及びその観測可能性 Conference: 日本物理学会　2015 年春季年会 / Date: March, 2015 Authors: Chinami Kato Title: 超新星前兆ニュートリノの放出率及びその観測可能性 Conference: 日本天文学会　2015 年春季年会 / Date: March, 2015 Authors: Chinami Kato Title: Progenitor model による前兆ニュートリノ放出率の違いと観測可能性 Conference: 新学術「宇宙の歴史をひもとく地下素粒子原子核研究」第一回超新星ニュートリノ研究会 / Date: March, 2015 Authors: Chinami Kato Title: モンテカルロ法を用いたニュートリノ輸送計算 Conference: 理論懇シンポジウム / Date: December, 2018 Authors: Chinami Kato, Hiroki Nagakura, Yusuke Hori & Shoichi Yamada Title: Pre-SN neutrino emissions in all-flavors from SN progenitors and their detectability Conference: Physics of Core-Collapse Supernovae and Compact Star Formations Date: March, 2018 Authors: Chinami Kato, Shoichi Yamada, Hiroki Nagakura, Shun Furusawa, Koh Takahashi, Takashi Yoshida, Hideyuki Umeda & Koji Ishidoshiro Title: Pre-SN neutrino emissions in all-flavors from SN progenitors and their detectability Conference: Microphysics in Computational Relativistic Astrophysics 2017 Date: July, 2017 Authors: Chinami Kato, Shoichi Yamada, Hiroki Nagakura, Shun Furusawa, Koh Takahashi, Takashi Yoshida, Hideyuki Umeda & Koji Ishidoshiro Title: 原子核による前兆ニュートリノ放出とその観測可能性 Conference: 理論懇シンポジウム/ Date: December, 2016 Authors: Chinami Kato, Shoichi Yamada, Hiroki Nagakura, Shun Furusawa, Koh Takahashi, Takashi Yoshida, Hideyuki Umeda & Koji Ishidoshiro

早稲田大学　博士（理学）　学位申請　研究業績書

種 類 別	題名、　発表・発行掲載誌名、　発表・発行年月、　連名者（申請者含む）
	Title: Pre-SN neutrino emissions from ONe cores in the progenitors of core-collapse supernova Conference: IAUS329:The lives and death-throes of massive stars Date: November, 2016 Authors: Chinami Kato, Shoichi Yamada, Hiroki Nagakura, Shun Furusawa, Koh Takahashi, Takashi Yoshida, Hideyuki Umeda & Koji Ishidoshiro Title: The properties of pre-SN neutrinos and its observational detection ～ towards the comprehensive supernova neutrino studies Conference: Many Riddles About Core-Collapse Supernova Date: June, 2016 Authors: Chinami Kato, Shoichi Yamada, Hiroki Nagakura, Wakana Iwakami, Shun Furusawa, Koh Takahashi, Takashi Yoshida, Hideyuki Umeda & Koji Ishidoshiro Title: 超新星前兆ニュートリノによる親星モデルの判別可能性 Conference: 新学術「宇宙の歴史をひもとく地下素粒子原子核研究」領域研究会 Date: May, 2015 Authors: Chinami Kato, Shoichi Yamada, Koh Takahashi, Takashi Yoshida, Hideyuki Umeda & Koji Ishidoshiro
その他 （セミナー）	Title: The evolutions of massive stars and the importance of neutrino observations Seminar : 広島大学素粒子論研究室におけるセミナー Date: October, 2018 Authors: Chinami Kato Title: The evolutions of massive stars and the importance of neutrino observations Seminar : 高エネルギー加速器研究機構におけるセミナー Date: June, 2018 Authors: Chinami Kato Title: 全フレーバーの前兆ニュートリノ放出とその観測可能性 Seminar : 東北大学ニュートリノ科学研究センターにおけるセミナー Date: July, 2017 Authors: Chinami Kato Title: 前兆ニュートリノの親星依存性とその観測～超新星ニュートリノの包括的な研究へ向けて Seminar : 東京大学宇宙線研究所におけるセミナー Date: May, 2016 Authors: Chinami Kato